Electronic Properties of Mesostructured Metal Oxides in Dye-Sensitized Solar Cells

Pablo Docampo

Worcester College

University of Oxford

A thesis submitted for the degree of

Doctor of Philosophy

May 2012

Declaration

This thesis is the result of my own work and includes nothing which is the outcome of work done in collaboration except where specifically indicated in the text.

I declare that no part of this work has been submitted for a degree or any other qualification at this or any other university.

Pablo Docampo, May 2012

I dedicate this thesis to my loving girlfriend, Cassandra, and my family.

Acknowledgements

Foremost, I would like to thank Dr. Henry J. Snaith for giving me the opportunity to carry out my research project in his laboratory at the University of Oxford. I specially thank him for his constant availability to answer all my questions through many useful discussions. Secondly, I would like to thank my fellow colleagues for their support and ever-present science discussions. Especially Agnese Abrusci (thanks for proof-reading my thesis and applications!).

I highly appreciate the collaborations with Prof. Ullrich Steiner's group at the University of Cambridge and Prof. Ullrich Wiesner's group at Cornell University. Morgan Stefik (Cornell) and Stefan Guldin (Cambridge) were really hard-working and helpful and it was a pleasure to collaborate with them.

I would also like to thank the groups of Prof. Peng Wang (Chinese Academy of Sciences, China) and Hidetoshi Miura (Chemicrea inc. Japan) for supplying the dyes used in this thesis.

I thank Paul Pattinson for his bottomless patience and good humour while dealing with literally dozens of people trying to use the same small clean room at the same time on a regular basis. I know it was a stressful job, but you made all our lives easier.

I also thank my parents, family and Sali for their support and extremely appreciated deliveries of food. The taste of those empanadas definitely made me feel like I was back at home for a little while. I also can't imagine traveling anywhere without "empanadillas da avoa".

Finally, there are no words to express my gratitude to my girlfriend Cassandra for her unconditional love, unwavering support, and the wonderful time we have spent together in Oxford. I love you too.

Abstract

Solid-state dye-sensitized solar cells (ssDSCs) offer the possibility of high power conversion efficiencies (PCEs) of over 20%. However, after more than a decade of research, devices still barely reach over 7% PCEs. In this thesis, limitations to device performance are studied in detail, and solutions for future advancement are put forward.

In the first part of the thesis, factors limiting charge generation are explored by studying the crystallization environment of mesoporous TiO_2 self-assembled through block copolymers. It was found that the density and distribution of sub band gap states are a function of the synthesis conditions and critically affect the performance characteristics of the self-assembled titania used in ssDSCs. As a result, the self-assembled mesoporous oxide system presented in this thesis outperforms for the first time the conventional nanoparticle based electrodes fabricated and tested under the same conditions, with demonstrated PCEs of over 5%.

In chapters 6, 7 and 8, the factors limiting the diffusion length and hence, the thickness of the fabricated devices, are carefully examined. Previous literature points towards insufficient pore-filling of the hole transporting material (HTM) as the main limiting factor. In chapter 6 a pore-filling study is shown where a new technique to evaluate the pore-filling fraction of the HTM in the conventional mesoporous metal oxide electrode is also presented and conclude that sufficient pore-filling of thick films can easily be achieved. Another usual strategy to extend the electron lifetime in the devices and thus, the charge diffusion length, involving thin film coatings of insulating metal oxides is examined in chapter 7, with satisfactory results for SnO_2-based

ssDSCs. The diffusion length can also be extended if the factors limiting the diffusion of charges through the device are identified and removed, as presented in chapter 8.

Finally, a study on the stability of the ssDSC is presented in chapter 9. The developments achieved enable long term stability to be effectively targeted, and represent a key milestone towards commercial realization of ssDSCs.

Contents

List of Figures

Nomenclature

Δn	photoinjected electron density
ΔQ	charge collection efficiency corrected charge generated with perturbation pulse
ΔQ_m	measured charge generated with perturbation pulse
ΔV	perturbation voltage amplitude
Δ	phase shift of the reflected component
ϵ	extinction coefficient
η	power conversion efficiency
η_{abs}	fraction of absorbed light
η_{col}	charge collection efficiency
η_{trans}	fraction of successfully generated electron-hole pairs from each incident photon
μ	mobility
Φ_B	Schottky barrier height
σ	conductivity
τ_e	recombination lifetime of electrons
τ_n	effective electron recombination lifetime

τ_{meas} measured transport lifetime at short circuit conditions

τ_{trans} transport lifetime of electrons

A electric field amplitude

A^* Richardson constant for thermionic emission

A_r reflected electric field amplitude

c spiro-OMeTAD casting solution concentration

C_2 particle independent thermodynamic constant

d thickness of film

D_e diffusion coefficient of electrons

D_L diffusion length of electrons

D_n effective diffusion coefficient

e electron charge

E_A acceptor energy level

E_D donor energy level

E_F Fermi energy level

F_A Fermi-Dirac function at energy E

FF fill factor

h Plank's constant

J current density

J_S saturation current density

J_{SC} short circuit current density

JV current-voltage

JV_{max} Maximum power point

k Boltzmann constant

m^* effective electron mass

n refractive index

N_A number of traps

n_a trapped charge density

n_eff effective refractive index

$n_{av,eff}$ averaged, effective refractive index

N_{CB} number of available states at the conduction band

n_{CB} density of free electrons in the conduction band

n_{CL} refractive index contribution from the capping layer

$n_{eff,CL=0}$ refractive index of film with maximally filled pores

n_{FREE} free electron charge density

N_{TOT} number of traps

n_{TRAP} trapped electron charge density

p mesoporous layer porosity

P_i incident power

q electron charge

R reflectance

r relative reflected amplitude

S dye ground state

S^+ oxidized dye

T temperature

T transmitted light fraction

t mesoporous layer thickness

t relative transmitted amplitude

t_{CL} capping layer thickness

t_{wet} wet layer thickness

v_i volume fraction

V_{OC} open circuit voltage

v_{pores} volume fraction of available pores

BET Brunauer-Emmett-Teller

C capacitance

CB conduction Band

CIGS copper indium gallium selenide

DOS density of states

DSC dye-sensitized solar cell

E Energy

FTO fluorine doped tin oxide

HOMO highest occupied molecular orbital

HTM hole transporting material

IPCE incident photon to electron conversion efficiency

ISO poly(isoprene-*b*-styrene-*b*-ethylene oxide)

LUMO lowest unoccupied molecular orbital

OPTP optical-pump terahertz-probe

P123 poly(ethylene oxide-*b*-propylene oxide-*b*-ethylene oxide)

PEO poly(ethylene oxide)

PF pore-filling

PI poly(isoprene)

ssDSC solid-state dye-sensitized solar cell

UV ultra-violet

VB valence Band

Chapter 1

Introduction

1.1 Background

The world's current energy consumption rate has risen to nearly 15 TW, a figure that has doubled since the late 70s, and is projected to increase in excess of 50% by 2035. At present, over 67% of the energy is produced from combusting coal, natural gas and oil, a pattern that is likely to remain practically unchanged by 2035.[1] Scientific consensus has been unequivocally reached in attributing the observed climate change to the carbon dioxide emissions from combustion of fossil fuels.[2] To avoid causing dangerous climate change, carbon dioxide emissions must be reduced greatly in the next 20-30 years.[3]

In an effort to meet this challenge, renewable energy sources such as sunlight, wind, tides or geothermal heat have been harnessed to produce around 6% of the current energy demand. Among those natural sources of energy, the most abundant is sunlight. If we were able to harvest all the energy that is incident on the surface of the earth for 1 hour we would be able to meet the yearly requirements of the whole planet. It is obvious that covering the whole surface of the earth with solar cells is not an option, but with less than 0.7% coverage of the available land mass, and the use of devices with an incident to output power conversion efficiency of 8%, we would be able to satisfy the world's energy needs.

All materials absorb sunlight in one way or another, however, in most systems, this absorbed energy is usually converted into heat. This has lead to the develop-

ment of systems that make use of this property to heat up water for domestic use or to drive a turbine and generate electrical power in that manner.[4] However, it is also possible to directly generate an electrical current, termed "photocurrent", directly from sunlight incident on carefully chosen materials. This last category of devices are known as photovoltaic solar cells.

Most of the research effort in photovoltaics has been directed at inorganic semiconductor solar cells, which can achieve power conversion efficiencies for single junction devices, for example crystalline silicon, of up to 25% and over 40% in multijunction devices.[5] These cells albeit being very efficient, tend to have quite complicated fabrication protocols that require very high temperatures and need copious amounts of the materials used, typically hundreds of micrometers for crystalline silicon, which make them expensive to produce. In an attempt to reduce material cost, thin film alternatives (from nanometers to micrometers) have been developed in the form of amorphous and nanocrystalline silicon or other direct band-gap materials, such as gallium arsenide (GaAs) or copper indium gallium selenide (CIGS). These devices have other pitfalls: in the former case, the power conversion efficiencies are typically considerably lower, hovering around 12% for the best laboratory devices. In the latter case, the most efficient direct band-gap materials utilize rare elements, such as Indium, which are relatively much less abundant and harder to extract than silicon. More importantly, these materials lack the massive technical know-how of silicon industrial production. In particular, although GaAs is as far as performance is concerned a much better solar cell material, its associated production costs are so high that mass-production at present is unviable. For these reasons, the uptake of photovoltaic energy generation has not been strong.

Some low-cost alternatives have been introduced over the years, such as organic, quantum dot-based or other inorganic semiconductor-based solar cells.[6, 7, 8] A common theme across all of these types of devices is that they are compatible with solution processing techniques. Manufacture of these devices can be easily implemented using existing printing and coating equipment.[9] This is a particularly important aspect because if our goal is to not only keep up with but to also overcome the global energy demand to be able to substitute other sources of energy, the production rate is critical in order to cover the required hundreds

of thousands of squared kilometers.

1.2 Dye-Sensitized Solar Cells

Dye-Sensitized Solar Cells (DSC) as introduced by O'Regan and Grätzel in 1991 offer a low-cost and mass-producible system.[10] These devices are composed of a monolayer of light absorbing dye adsorbed to the surface of a mesoporous electron transporting metal oxide, usually a TiO_2 film fabricated from sintered nanoparticles. Photons excite electrons from the highest occupied molecular orbital (HOMO) to the lowest unoccupied molecular orbital (LUMO) of the dye and is subsequently injected into, and transported through the TiO_2 mesostructure to the collection electrode, typically fluorine doped tin oxide (FTO). The other side of the dye is contacted by a redox active electrolyte, usually iodide/triiodide-based, which regenerates the oxidized dye molecules and transports the holes to the counter electrode, usually platinum coated FTO.

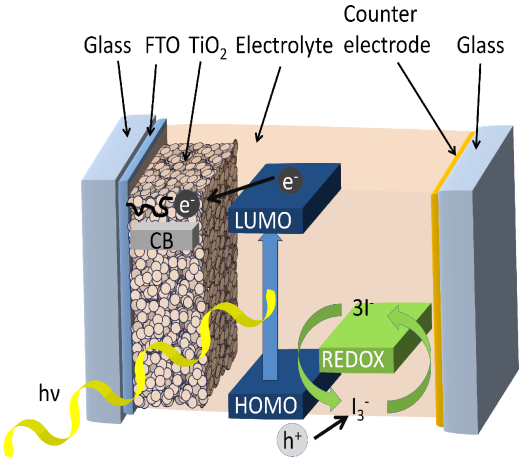

Figure 1.1: Dye-Sensitized Solar cell schematic.

The use of liquid electrolyte leads to significant technological challenges, as the devices must be carefully sealed to avoid leaks. Furthermore, the archetypal redox couple iodide tri-iodide is corrosive. In order to address these issues, in 1998 Bach et al replaced the liquid electrolyte with an organic solid-state alternative, (2,2(7,7(- tetrakis-(N,N-di-pmethoxyphenylamine)9,9(-spirobifluorene) Spiro-OMeTAD.[11] A schematic of the device structure is shown in figure 1.1. Since the ionization potential of spiro-OMeTAD is deeper that the redox potential of iodide/tri-iodide couple the theoretical maximum voltages attainable with solid state devices should be higher and would result in a greater power conversion efficiency.[12, 13] Indeed this loss limits the former devices to around

15% efficiency, while it should be possible to reach over 20% with a solid-state hole transporter (HTM). Devices fabricated with a solid-state HTM have been reported to surmount 7% efficiencies and large improvements are foreseeable in the near future.[14]

To offer commercially competitive devices, several challenges must be overcome: long-term stability; pore filling so as to maximize charge collection efficiency; panchromatic absorption to ensure that the optimum amount of light is absorbed; and efficient charge generation per absorbed photon so as to maximize the current output from the sunlight.

1.3 Aims of the present thesis

In spite of the apparent simplicity of DSC operation, much of the underlying physics still needs to be elucidated. Unraveling the mechanisms of charge generation in solid-state DSCs (sDSC) and the limiting factors to charge transport and recombination is crucial in order to achieve the potential for this system and constitutes the main goal of the present work.

Conventional approaches to studying electronic properties of DSCs usually rely upon the preparation of nanoparticles via colloidal synthesis methods. In this way, porosity, crystal size, surface area, crystal type etc. can be easily modified.[15, 16, 17] However, this advantage comes at a cost: the surface area, crystal size and porosity of the resulting films are linked and cannot be independently modified, making the study of subtle changes in the crystallization environment practically impossible. Using materials self-assembled through block copolymers presents a novel solution to study the charge generation and transport mechanisms in sDSCs.

Disentangling the issues that limit the thickness of the devices to around 2 μm is the other main focus of this thesis. This is particularly important because enabling thick films allows the use of panchromatic sensitizers that can absorb a wider band of the solar irradiance spectrum which can lead to a doubling of the device performance. In the past, the thickness limitations of the solid-state dye-sensitized solar cells have been primarily blamed on poor pore filling by the hole transporter material. For this reason, in chapter 6 I will present a study in

pore filling, which due to the thin film nature of the system, can be measured by studying the resulting interference fringes.

In order to achieve working solid-state dye-sensitized solar cells fabricated from thick films, the diffusion length must be extended. This parameter is a combination of the diffusion coefficient, i.e. how quickly the charges move through the film, and the recombination lifetime, i.e. how long will the electrons and holes last before they annihilate one another. A typical strategy employed is based on achieving longer electron lifetimes through coating of thin shells of insulating metal oxides over the mesoporous photoanode. In chapter 7 I will study the role of a thin MgO layer over SnO_2-based dye-sensitized solar cells. It is usually found that in absence of this layer, extremely poor performance (under 1%) is generally achieved for DSCs based on these materials, and therefore studying its role is important in order to understand what factors are limiting the device performance.

I also present a study examining the limits to the electron transport in mesoporous TiO_2 photoanodes in chapter 8. By using block copolymer assembled photoanodes, the morphology of the films was kept more or less constant, resulting in mesostructures with very different particle sizes but very similar exposed surface areas. This has allowed me to study in detail the effects of the grain boundaries on the transport properties of the TiO_2 photanodes used in solid-state dye-sensitized solar cells.

Finally, I present a study on the encapsulation of sDSCs in an inert atmosphere. This is particularly important since stability over 10000 hours is a requirement for buildings or utility scale power applications. Un-encapsulated devices exposed to ambient air and sunlight usually degrade to less than half the initial performance within days. Previously, every attempt to encapsulate cells in nitrogen resulted in devices degrading within minutes of sunlight illumination. Curiously, once exposed to air again, devices recover their initial performance. This led to the identification of a shunting path between the mesoporous metal oxide and the cathode that forms a Schottky barrier under ambient air. I will discuss in detail a solution to this problem in chapter 9.

References

[1] John Conti and Paul Holtberg. International energy outlook 2011. *Report Number: DOE/EIA-0484(2011)*, 2011. 1

[2] Naomi Oreskes. The scientific consensus on climate change. *Science*, 306(5702):1686, 2004. 1

[3] Kevin Anderson and Alice Bows. Beyond 'dangerous' climate change: emission scenarios for a new world. *Philosophical Transactions of the Royal Society A: Mathematical,Physical and Engineering Sciences*, 369(1934):20–44, 2011. 1

[4] Roland Winston. Principles of solar concentrators of a novel design. *Solar Energy*, 16(2):89–95, 1974. doi: DOI: 10.1016/0038-092X(74)90004-8. 2

[5] Martin A. Green, Keith Emery, Yoshihiro Hishikawa, and Wilhelm Warta. Solar cell efficiency tables (version 37). *Progress in Photovoltaics: Research and Applications*, 19(1):84–92, 2011. 2

[6] Gang Li, Vishal Shrotriya, Jinsong Huang, Yan Yao, Tom Moriarty, Keith Emery, and Yang Yang. High-efficiency solution processable polymer photovoltaic cells by self-organization of polymer blends. *Nat Mater*, 4(11):864–868, 2005. 10.1038/nmat1500. 2

[7] Steven A. McDonald, Gerasimos Konstantatos, Shiguo Zhang, Paul W. Cyr, Ethan J. D. Klem, Larissa Levina, and Edward H. Sargent. Solution-processed pbs quantum dot infrared photodetectors and photovoltaics. *Nat Mater*, 4(2):138–142, 2005. 10.1038/nmat1299. 2

[8] Hironori Katagiri, Kazuo Jimbo, Win Shwe Maw, Koichiro Oishi, Makoto Yamazaki, Hideaki Araki, and Akiko Takeuchi. Development of czts-based thin film solar cells. *Thin Solid Films*, 517(7):2455 – 2460, 2009. 2

[9] Frederik C. Krebs, Thomas Tromholt, and Mikkel Jorgensen. Upscaling of polymer solar cell fabrication using full roll-to-roll processing. *Nanoscale*, 2:873–886, 2010. 2

[10] Brian O'Reagan and Michael Gratzel. A low cost, high efficiency solar cell based on dye-sensitised TiO_2 films. *Nature*, 353:737–740, 1991. 3

[11] U Bach, P Comte, J E Moser, F Weisso, and Michael Gratzel. Solid-state dye-sensitized mesoporous TiO_2 solar cells with high photon-to-electron conversion efficiencies. *Nature*, 395:583–585, 1998. 3

[12] John N. Clifford, Emilio Palomares, Md K. Nazeeruddin, M. Gratzel, and James R. Durrant. Dye dependent regeneration dynamics in dye sensitized nanocrystalline solar cells: evidence for the formation of a ruthenium bipyridyl cation/iodide intermediate. *The Journal of Physical Chemistry C*, 111(17):6561–6567, 2007. 3

[13] H. J. Snaith. Estimating the maximum attainable efficiency in dye-sensitized solar cells. *Advanced Functional Materials*, 20(1):13–19, 2010. 3

[14] Julian Burschka, Amalie Dualeh, Florian Kessler, Etienne Baranoff, Ngoc-Le Cevey-Ha, Chenyi Yi, Mohammad K. Nazeeruddin, and Michael Gratzel. Tris(2-(1h-pyrazol-1-yl)pyridine)cobalt(iii) as p-type dopant for organic semiconductors and its application in highly efficient solid-state dye-sensitized solar cells. *Journal of the American Chemical Society*, 133(45):18042–18045, 2011. 4

[15] N. Kopidakis, N. R. Neale, K. Zhu, J. van de Lagemaat, and A. J. Frank. Spatial location of transport-limiting traps in TiO_2 nanoparticle films in dye-sensitized solar cells. *Appl. Phys. Lett.*, 87(20), 2005. 4

[16] Shingo Kambe, Shogo Nakade, Yuji Wada, Takayuki Kitamura, and Shozo Yanagida. Effects of crystal structure, size, shape and surface structural differences on photo-induced electron transport in TiO_2 mesoporous electrodes. *J. Mater. Chem.*, 12:723–728, 2002. 4

[17] Arthur J. Frank, Nikos Kopidakis, and Jao van de Lagemaat. Electrons in nanostructured TiO_2 solar cells: transport, recombination and photovoltaic properties. *Coordination Chemistry Reviews*, 248(13-14):1165 – 1179, 2004. 4

Chapter 2

Solar cell operating principles

2.1 Conventional Photovoltaics

In their simplest incarnations, photovoltaic cells are composed of semiconductor materials, i.e. materials where electrons require a certain energy to be able to roam the lattice freely, termed band-gap energy. Electrons possessing this energy (or higher) are said to be in the conduction band (CB), while electrons still bound to their individual atoms are said to be in the valence band (VB). The band-gap energy of the material determines the sunlight spectrum absorption onset, shown shaded in blue for crystalline silicon in figure 2.1, since only photons with energies above the band-gap can excite electrons into the CB. This quantity also determines the maximum current that can be generated from the complete device. For every electron excited into the conduction band, a hole is left behind in the valence band where the electron used to be bound to the lattice atom. These holes can be treated as positively charged particles, free to move in the valence band.[1]

In complete devices, a carefully engineered junction where one side is p-doped, i.e. has an excess of holes, and the other side is n-doped, i.e. has an excess of electrons, is used to extract the charges from the device. This type of bilayer structure is called a p-n junction. When the p-side and the n-side are joined, at first, holes from the p-side tend to diffuse through to the n-side and likewise, electrons from the n-side tend to diffuse through to the p-side where they recom-

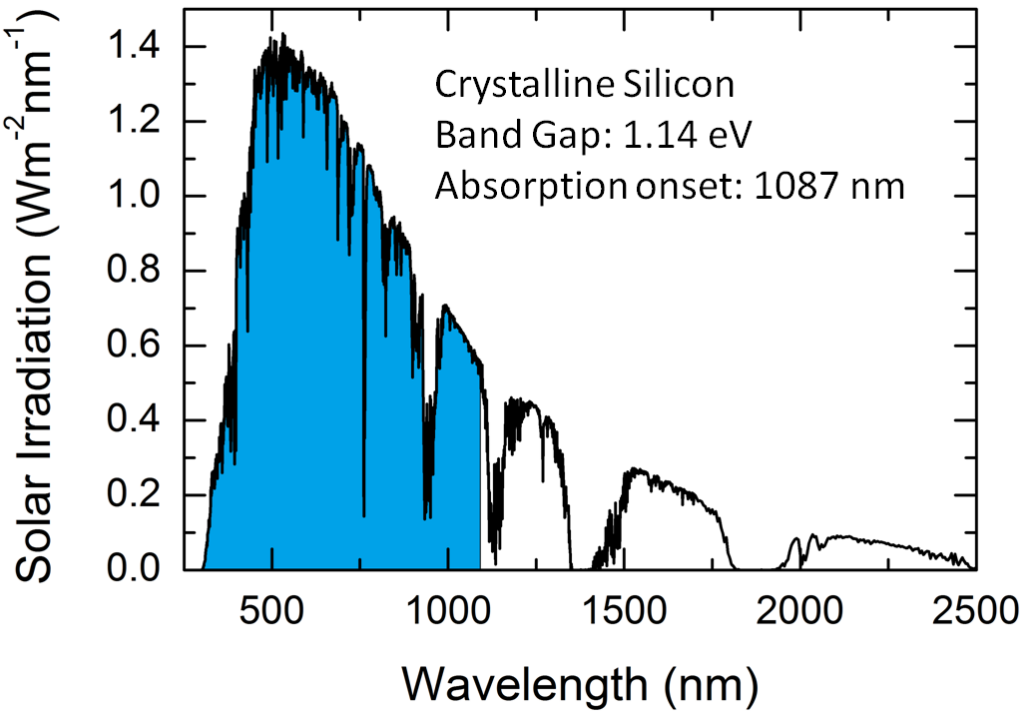

Figure 2.1: Irradiance against wavelength for the solar spectrum Air Mass 1.5 incident on the surface of the earth. Shaded in blue is the absorption of crystalline silicon.[2]

bine with a charge of the opposite sign. In this manner, a depletion region is formed, i.e. no mobile charges are present, and the net charge of the immobile dopant ions left close to the junction on the p-side becomes negative (holes have been lost) and in the same way, dopant ions close to the junction on the n-side become positive. This sets up a built-in field that pushes electrons towards the n-side and holes toward the p-side.

To quantify the magnitude of the built-in potential, the Fermi energy level of the material must be studied. This quantity determines the occupancy of electrons of the conduction band and it depends strongly on doping levels, density of states and temperature. For instance, in heavily doped materials, the Fermi level is approximately determined by the binding energy of the dopant. Since the Fermi level must be situated at a constant distance from vacuum, when one heavily doped n-type material is contacted with a heavily doped p-type material,

band bending as shown on figure 2.2 occurs. The built-in potential is thus given by the differences between the donor energy level (E_D) and the acceptor energy level (E_A). When the p-n junction is exposed to light, more electron-hole pairs are generated and consequently the total populations of holes and electrons are displaced from simple thermal equilibrium. This leads to the redefinition of the Fermi level into two quasi Fermi levels, one for each type of charge. The difference between the two quasi Fermi levels gives the magnitude of the open circuit potential.[3]

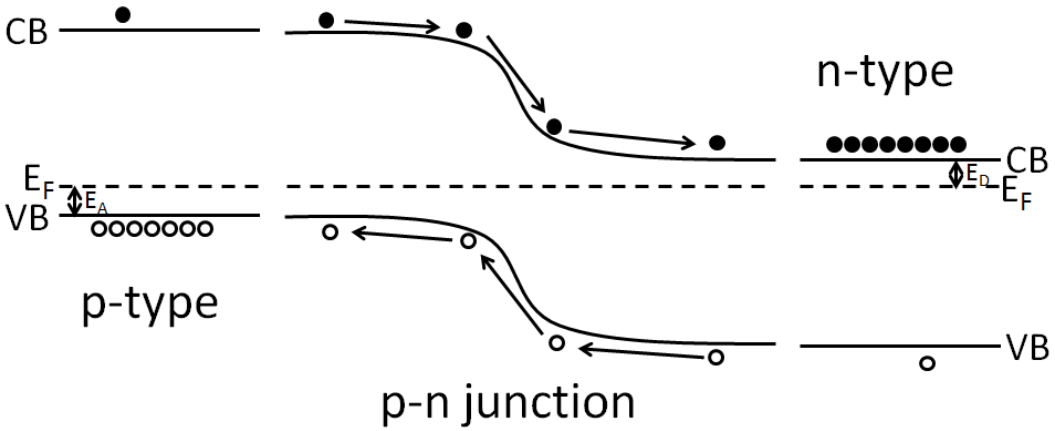

Figure 2.2: Energy band diagram showing band bending of a p-n junction, where CB is the conduction band, VB is the valence band, E_F is the Fermi level, E_A is the acceptor binding energy and E_D is the donor binding energy

2.2 Solar Cell Characterization

Solar cells are generally characterized by measuring their current against voltage curve (J-V Curve). From here, the most useful parameters can be extracted: power conversion efficiency (η), short circuit current (J_{SC}), open circuit voltage (V_{OC}) and fill factor (FF). The short-circuit current is the current measured when the anode and the cathode are connected without a load, or in other words when the applied voltage is zero. The open circuit voltage can be measured when the anode and cathode are connected with a high load, or in other words when the current reaches zero. The fill factor is calculated as simply as:

$$FF = \frac{(JV)_{max}}{J_{SC}V_{OC}} \tag{2.1}$$

where JV_{max} is the maximum power point of the JV curve. The power conversion efficiency depends on the incident power (P_i) and is calculated as:

$$\eta = \frac{J_{SC}V_{OC}FF}{P_i} \tag{2.2}$$

It is interesting to understand which material factors affect the different photovoltaic parameters. For instance, consider two hypothetical solar cells that have no other differences besides utilizing a wide band gap material to absorb light in the first case and a narrow band gap material for the second case. This change would be reflected in the JV curve since the absorption onset has changed: the film with the narrower bandgap will generate a higher J_{SC} because it's absorbing more photons, but it will also have a lower V_{OC} because the difference in Fermi level for holes and electrons will be smaller. Depending on how much the bandgap has changed and taking into account the shape of solar irradiance spectrum, these two cells could have the exact same power conversion efficiency. A good technique then to discriminate between solar cells with different absorption spectra is by measuring the incident photon to electron conversion efficiency (IPCE). For this measurement, a monochromator is used to output light at a single wavelength, with a known photon flux and simply sweep through the required

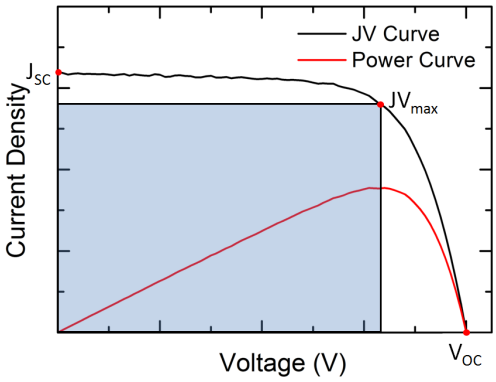

Figure 2.3: Illustration of a JV curve for a solar cell under illumination. The power curve is used to determine JV_{max}. The shaded area corresponds to the maximum power output attainable.

wavelength range.

Due to the inherent trade-off between current and voltage, an optimum absorber for the solar spectrum incident on earth can be found. If the solar cells were operating without losses within the system, a maximum of approximately 33% power conversion efficiency with a bandgap of 1.4 eV can be achieved for a single junction type of device.[3, 4] The best solar cells fabricated with monocrystalline silicon (∼1.1 eV bandgap) currently reach around 25% power conversion efficiency.[5, 6] Silicon, however, is a material with an indirect bandgap, i.e. the the minimum in the conduction band energy is at a different wave vector than the valence band maximum. In essence, in order to absorb a photon and generate an electron-hole pair, some extra momentum must be provided simultaneously by phonons, i.e. lattice vibration modes. This occurs relatively "rarely", so the films must be very thick (in the order of hundreds of micrometers to milimeters) in order to absorb light efficiently and this affects the maximum performance achievable. The most efficient solar cells are currently fabricated from gallium arsenide (GaAs), with record efficiencies reaching 28% [5], mostly due to its more favourable direct bandgap (∼1.4 eV) which minimizes charge transport related losses.

2.3 DSC and ssDSC operation

The operational principles behind dye-sensitized solar cells (DSCs) and solid-state DSCs (ssDSCs) are a bit different from conventional photovoltaic devices. In this instance, the functions of absorber, hole transporter and electron transporter have been decoupled, and a p-n junction to collect the charges efficiently is no longer used. A schematic of this process is shown in figure 2.4.

2.3.1 Photoinduced charge transfer

The first process in the working circuit of a DSC involves photoexcitation of an electron from the HOMO to the LUMO of the dye, followed by electron transfer into the metal oxide used and hole regeneration by the hole transporter. In order to maximize photoinduced charge transfer from the dye into the metal oxide,

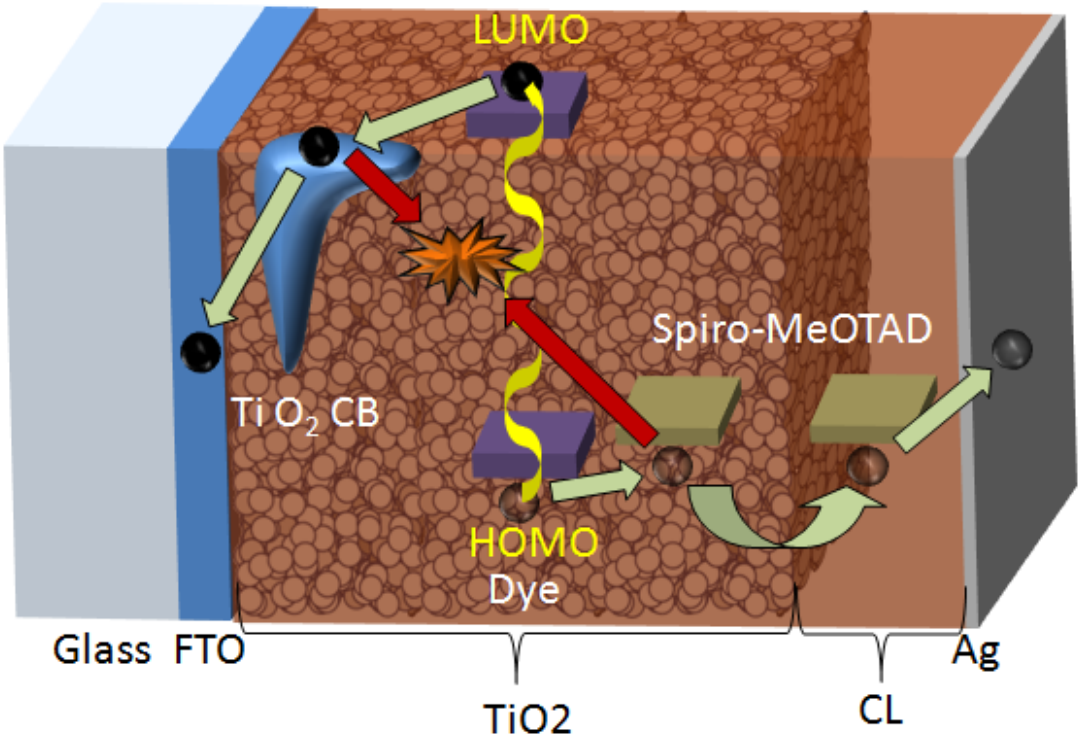

Figure 2.4: DSC charge transport mechanism. Green arrows represent the charge transport paths while the red arrows represent the recombination path.

the following considerations must be taken into account: there are competing photoexcited state decay channels that don't result in electron-hole pairs that must be orders of magnitude slower than photoinduced electron transfer and it must be energetically favorable to transfer electrons from the LUMO of the dye to the available energy states in the metal oxide and also from the HOMO level to the ones in the hole transporter. The first requirement can be dealt with by smart design of the sensitizers, usually incorporating a donor-acceptor π-conjugated system, where the holes are "pulled" away from the TiO_2 interface and the electrons are "pushed" towards the anchoring groups.[7] The second requirement implies designing the dyes to place the LUMO at a potential above the CB of the metal oxide and the HOMO below the oxidation potential of the hole transporter. In both cases, an "over-potential" of around 0.2-0.3 eV on both sides appears to be allowed for to drive the reactions efficiently, i.e. close to unity.[8] In the case of DSCs with iodine/iodide-based electrolytes, a further 0.3

eV overpotential is necessary to convert $2I_2^-$ to I_3^-.[9]

2.3.2 Electron transport

Once the electrons have been transferred to the metal oxide, simple diffusion is relied on to collect the charges. When light is switched on on the device, an electron concentration gradient is established where the areas near the electrodes are electron-depleted and charge is being constantly pumped in at the metal oxide/dye interface (see figure 2.5).[8] The electron mobility in nanocrystalline TiO_2 is several orders of magnitude smaller than in bulk, in the order of $10^{-4}cm^2V^{-1}s^{-1}$ against 10 $cm^2V^{-1}s^{-1}$,[10, 11] as well as showing a strong dependence on light intensity, suggesting that electrons undergo multiple trapping events in sub bandgap states before reaching the electrodes.[8, 12, 13] The transport mechanism is thus: electrons are transferred into the mesoporous oxide where they become trapped at sub bandgap states. Then, they are thermally released into the conduction band, where they are free to move until they become trapped again. In this way, transport is governed by detrapping times, which become longer for the deeper traps.[8, 12, 13, 14]

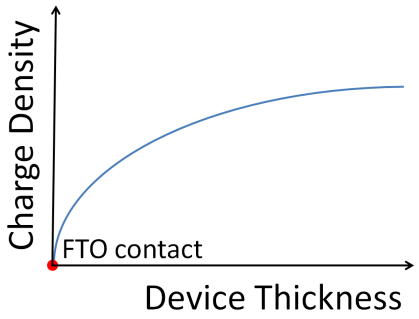

Figure 2.5: Charge density distribution under short-circuit conditions

In its simplest form, the distribution of sub bandgap states can be considered as a single exponential and its occupancy is given by the Fermi-Dirac distribution function at an energy E with n_A as the density of carriers at this energy and N_A as the number of available states at this energy. Transport occurs through free electrons in the conduction band (n_{CB}), so in order to determine conductivity of the film which is proportional to n_{CB},[14] it is necessary to calculate how this quantity changes with the quasi Fermi level of electrons in the film.

$$F_A = \frac{1}{1 + e^{\frac{E - E_F}{kT}}} \tag{2.3}$$

$$n_A = N_A F_A \tag{2.4}$$

$$n_{CB} = N_{CB} e^{\frac{E_{Fn} - E_{CB}}{kT}} \tag{2.5}$$

From equation 2.5, it can be inferred that the conductivity of the film increases with increasing probability of finding electrons in the conduction band, i.e. increasing electron quasi Fermi level, explaining the heavy dependence on light intensity of the charge transport timescales for this type of devices.[15]

2.3.3 Hole transport

Hole transport in the hole transporter is a diffusive process. In the case of the tri-iodide/iodide system, following reactions occur, were S^+ refers to the oxidized dye and S to its ground state:[9, 16]

$$S^+ + \frac{3}{2} I^- \rightarrow S + \frac{1}{2} I_3^- \tag{2.6}$$

$$I_3^- + 2 \cdot e^-_{cathode} \rightarrow 3 I^-_{cathode} \tag{2.7}$$

For reaction 2.6 to occur, an intermediate di-iodide (I_2^-) complex must be formed so that it then reacts with another di-iodide complex to form the resulting tri-iodide complex.[17] Again, as in the case of electron transport, a concentration gradient where an excess of tri-iodide complexes are being generated at the mesoporous photoanode interface and they are being depleted at the cathode was established, which converts them to 3 iodide ions through reaction 2.7. In order to have efficient hole diffusion in typical acetonitrile-based electrolytes, a 0.3 M concentration of iodide is sufficient, although for more viscous electrolytes, a higher concentration is necessary.[18]

Hole transport in solid-state hole transporters is best described as a diffusive hopping process,[19, 20] where holes are generated at the photoanode interface and are being depleted at the cathode. Typical hole mobilities of

10^{-4}cm^{2}V^{-1}s^{-1} are measured for the current best performing solid-state hole transporter (2,2(7,7(-tetrakis- (N,N-di- pmethoxyphenylamine) 9,9(-spirobifluorene) (Spiro-OMeTAD) which is more or less matched to the measured electron mobilities in TiO_2. [21] However, to improve device performance, the solid-state hole transporters are typically doped with ionic dopants as well as chemical dopants.[11, 22, 23] The effects of additives are not only limited to improve the conductivity and mobility of spiro-OMeTAD, but they also influence the charge generation mechanism by making changes to the surface of the mesoporous oxide.[11, 22, 24]

2.3.4 Cell operation-related losses

In DSCs, electron transfer is an extremely fast process in the femtosecond timescale, [25, 26] and hence losses before this process is complete are usually negligible. Dye regeneration can be quite slow, however, and hence up to 10% of the oxidized dye molecules can be intercepted in some systems, i.e. an electron from the CB of the mesoporous oxide returns the dye to the ground state, before being regenerated by the electrolyte depending on the potential upon the mesoporous metal oxide, i.e. bias.[27] The other main loss arises from recombination of holes in the electrolyte and electrons in the mesoporous oxide, although since dye regeneration requires an intermediate di-iodide complex that cannot undergo charge recombination, this process tends to be several orders of magnitude slower than transport through the mesoporous oxide. When the electrolyte is substituted with spiro-OMeTAD, dye regeneration is orders of magnitude faster and hence virtually no charge is lost to interception.[28] However, the electron recombination rate is on a much faster timescale than the liquid electrolyte counterpart, due to the fact that it's a single electron process. [15, 29]

It is convenient to define the diffusion coefficient (D_e), i.e. how quickly the charges are traveling through the metal oxide; the recombination lifetime (τ_e, i.e. how long until the electrons and holes recombine; the transport lifetime (τ_{trans}), i.e. how quickly the charges are collected at the electrodes; the diffusion length (D_L), i.e. how far can the charges travel before recombining; and the charge collection efficiency (η_{col}), i.e. the fraction of charges that are being collected.[30]

$$D_e = \frac{thickness^2}{2.35\tau_{trans}} \tag{2.8}$$

$$D_L = \sqrt{D_e \tau_e} \tag{2.9}$$

$$\eta_{col} = \frac{\tau_e}{\tau_e + \tau_{trans}} \tag{2.10}$$

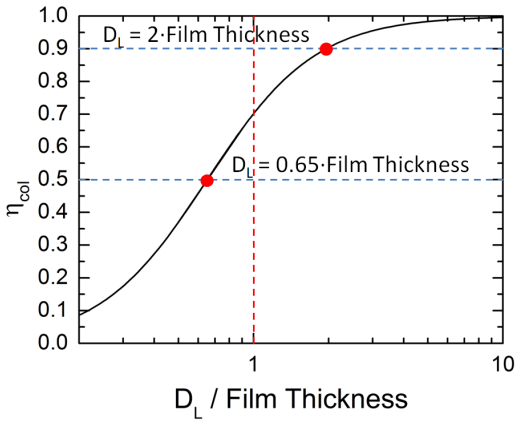

Figure 2.6: Theoretical charge collection efficiency dependence with thickness of film and diffusion length

The diffusion length (D_L) is a combination of all the other parameters and it has the deepest impact on device performance. As can be seen on figure 2.6, building a device with a thickness that is as long as the diffusion length only yields charge collection efficiencies of around 70%, whereas as soon as this parameter is over twice the film thickness, over 90% charge collection efficiency can be achieved. This means that only charges generated within an electron diffusion length of the electron contact can be collected efficiently. Therefore the strategy necessary to design a high power conversion efficiency device is to ensure that the electron diffusion length is long compared to the absorption length, i.e. the length at which most of the incident light has been absorbed, thereby ensuring simultaneously high charge collection and light absorption efficiencies. It is important to keep in mind that the diffusion length will vary greatly depending on the applied bias and light intensity incident on the film when optimising the constituent materials.[31, 32]

2.4 Measuring the electronic properties of DSCs

A technique successfully implemented for measuring the electronic properties of DSCs is based on performing transient decay experiments where a small light perturbation is applied to a cell under operation and its voltage or current response is measured. In essence, a steady-state background illumination is first applied to the cell, filling up a fraction of the available sub bandgap states which will scale with the light intensity applied. A schematic of this process is shown in fig 2.7. Then, a short pulse, typically under 200 μs long, which is shorter than the transport lifetimes and several orders of magnitude shorter than the recombination lifetimes, is shone on the cell and the response of the cell is recorded with an oscilloscope. The measurement can be performed at fixed potential conditions, i.e. potentiostatic mode, or at fixed current conditions, i.e. galvanostatic mode. In the latter case, the current generated through the small perturbation pulse is not allowed to exit the device and hence the response measured with oscilloscope is purely dependent on the recombination kinetics of the system. In the former case, current is allowed to flow through the device and hence the recorded dynamics reflect both the charge extraction and recombination characteristics. To extract the transport lifetime (τ_{trans}) from the measured photocurrent decay (τ_{meas}), the electron lifetime (τ_e) at short circuit conditions must be measured, and they can be related by the following equations:

$$\frac{1}{\tau_{meas}} = \frac{1}{\tau_{trans}} + \frac{1}{\tau_e} \tag{2.11}$$

$$\tau_{trans} = \frac{\tau_e \tau_{meas}}{\tau_e - \tau_{meas}} \tag{2.12}$$

The interpretation of these transient experiments is complicated by the fact that metal oxides are very disordered semiconductors with significant amounts of charge trapping. Since only free (untrapped, n_{CB} from eq. 2.5) charges in the metal oxide can be transported, the observed dynamics are a superposition of the "true" (free electron) dynamics and the trapping-detrapping mechanism. For this reason, a quasi static approximation must be used.[8, 14, 33] This leads to the redefinition of an effective diffusion coefficient (D_n) and effective electron

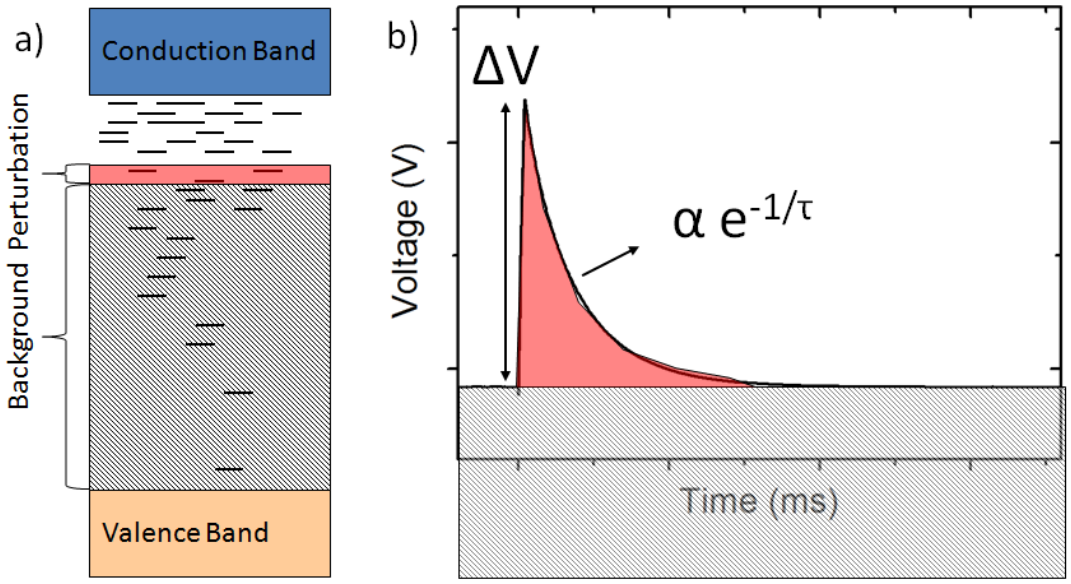

Figure 2.7: Photovoltage and photocurrent decay technique. a) Schematic of the energetics of the system. b) Typical decay curve for a photovoltage decay.

lifetime (τ_n):

$$\tau_n = \tau_e(1 + \frac{\partial n_A}{\partial n_{CB}}) \tag{2.13}$$

$$D_n = \frac{D_e}{1 + \frac{\partial n_A}{\partial n_{CB}}} \tag{2.14}$$

It follows that to calculate the diffusion length D_L from D_n and τ_n, the term $(1 + \frac{\partial n_A}{\partial n_{CB}})$, where n_A is the trapped electron density and n_{CB} is the free electron density, must be the same for both. This condition is satisfied when both the diffusion coefficient and electron lifetime are measured at the same quasi Fermi level.[8, 14, 33] This can be a problem, however, because the usual measurement procedure is to vary the background light intensity to change the quasi Fermi level of electrons in the film and measure the photovoltage decay at open circuit conditions. On the other hand, the photocurrent decays are usually measured at short circuit conditions and hence, the quasi Fermi level is at a much lower

potential. To get around this problem, a photovoltage decay at short circuit conditions can be acquired by sourcing a current through the device equal to its short circuit current. In this case, no extra current is allowed to flow, and all generated charge by the perturbation pulse must recombine. In this way, the electron lifetime at short circuit conditions can be obtained and then it is possible to extract the diffusion length under the same condition.[32, 34]

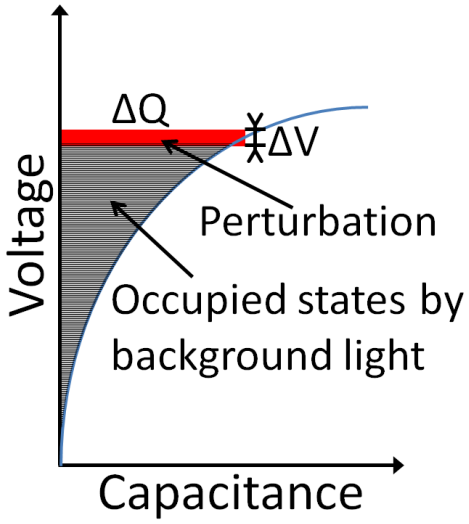

Figure 2.8: Schematic of capacitance against voltage plots

With this technique, it is also possible to extract the density of sub bandgap states of the mesoporous oxide. In brief, light is irradiated onto the cell to generate a certain open-circuit voltage and then flash the cell with a further light pulse, generating a small voltage perturbation (ΔV) which is recorded. The device is subsequently short-circuited, exposed to the same flash of light and the collected current is integrated to estimate the generated charge (ΔQ), after correcting for the losses due to charge recombination as $\Delta Q = \frac{\Delta Q_m}{\eta_{COL}}$, where ΔQ_m is the measured generated charge and η_{COL} is the charge collection efficiency. Knowing both, the voltage perturbation (ΔV) and the total amount of charge which is generated by the light pulse (ΔQ), the chemical capacitance $C = \frac{\Delta Q}{\Delta V}$ at a given open-circuit voltage can be derived. By plotting the resulting differential capacitance against voltage plot, as shown in figure 2.8 the density of states can be mapped out, since the capacitance gives the number of electrons that can be accumulated at each applied bias.

References

[1] S. N. Sze. Physics of semiconductor devices. *Wiley-Interscience. Second edition*, pages 256, 258, 1981. 8

[2] NREL. Astm g173-03 tables: Extraterrestrial spectrum, terrestrial global 37 deg south facing tilt and direct normal + circumsolar. *http://rredc.nrel.gov/solar/spectra/am1.5/*, 1999. 9

[3] Peter Wurfel. Physics of solar cells - from principles to new concepts. *Wiley-VCH*, 1st edition:141, 2005. 10, 12

[4] William Shockley and Hans J. Queisser. Detailed balance limit of efficiency of p-n junction solar cells. *Journal of Applied Physics*, 32(3):510–519, 1961. 12

[5] Martin A. Green, Keith Emery, Yoshihiro Hishikawa, Wilhelm Warta, and Ewan D. Dunlop. Solar cell efficiency tables (version 39). *Progress in Photovoltaics: Research and Applications*, 20(1):12–20, 2012. 12

[6] Jianhua Zhao, Aihua Wang, Martin A. Green, and Francesca Ferrazza. 19.8% efficient "honeycomb" textured multicrystalline and 24.4% monocrystalline silicon solar cells. *Applied Physics Letters*, 73(14):1991–1993, 1998. 12

[7] Yousuke Ooyama and Yutaka Harima. Molecular designs and syntheses of organic dyes for dye-sensitized solar cells. *European Journal of Organic Chemistry*, 2009(18):2903–2934, 2009. 13

[8] Laurence M. Peter. Dye-sensitized nanocrystalline solar cells. *Phys. Chem. Chem. Phys.*, 9:2630–2642, 2007. 13, 14, 18, 19

[9] Gerrit Boschloo and Anders Hagfeldt. Characteristics of the iodide/triiodide redox mediator in dye-sensitized solar cells. *Accounts of Chemical Research*, 42(11):1819–1826, 2009. 14, 15

[10] L. Forro, O. Chauvet, D. Emin, L. Zuppiroli, H. Berger, and F. Levy. High mobility n-type charge carriers in large single crystals of anatase (TiO_2). *Journal of Applied Physics*, 75(1):633–635, 1994. 14

[11] Henry J. Snaith and Michael Gratzel. Enhanced charge mobility in a molecular hole transporter via addition of redox inactive ionic dopant: Implication to dye-sensitized solar cells. *Applied Physics Letters*, 89(26):262114, 2006. 14, 16

[12] Jenny Nelson and Rosemary E. Chandler. Random walk models of charge transfer and transport in dye sensitized systems. *Coordination Chemistry Reviews*, 248(1314):1181 – 1194, 2004. 14

[13] Jenny Nelson. Continuous-time random-walk model of electron transport in nanocrystalline TiO_2 electrodes. *Phys. Rev. B*, 59:15374–15380, Jun 1999. 14

[14] Juan Bisquert and Vyacheslav S. Vikhrenko. Interpretation of the time constants measured by kinetic techniques in nanostructured semiconductor electrodes and dye-sensitized solar cells. *The Journal of Physical Chemistry B*, 108(7):2313–2322, 2004. 14, 18, 19

[15] J Kruger, R Plass, Michael Gratzel, PJ Cameron, and LM Peter. Charge transport and back reaction in solid-state dye-sensitized solar cells: A study using intensity-modulated photovoltage and photocurrent spectroscopy. *J. Phys. Chem. B*, 107(31):7536–7539, 2003. 15, 16

[16] Md. K. Nazeeruddin, Etienne Baranoff, and Michael Gratzel. Dye-sensitized solar cells: A brief overview. *Solar Energy*, 85(6):1172 – 1178, 2011. 15

[17] Ivan Montanari, Jenny Nelson, and James R. Durrant. Iodide electron transfer kinetics in dye-sensitized nanocrystalline TiO_2 films. *The Journal of Physical Chemistry B*, 106(47):12203–12210, 2002. 15

[18] Peng Wang, Bernard Wenger, Robin Humphry-Baker, Jacques-E. Moser, Joel Teuscher, Willi Kantlehner, Jochen Mezger, Edmont V. Stoyanov, Shaik M. Zakeeruddin, and Michael Gratzel. Charge separation and efficient light energy conversion in sensitized mesoscopic solar cells based on binary ionic liquids. *Journal of the American Chemical Society*, 127(18):6850–6856, 2005. PMID: 15869308. 15

[19] M. C. J. M. Vissenberg and M. Matters. Theory of the field-effect mobility in amorphous organic transistors. *Phys. Rev. B*, 57:12964–12967, May 1998. 15

[20] Dmitry Poplavskyy and Jenny Nelson. Nondispersive hole transport in amorphous films of methoxy-spirofluorene-arylamine organic compound. *Journal of Applied Physics*, 93(1):341–346, 2003. 15

[21] H.J. Snaith and L. Schmidt-Mende. Advances in liquid-electrolyte and solid-state dye-sensitized solar cells. *Adv. Mater.*, 19(20):3187–3200, 2007. 16

[22] Julian Burschka, Amalie Dualeh, Florian Kessler, Etienne Baranoff, Ngoc-Le Cevey-Ha, Chenyi Yi, Mohammad K. Nazeeruddin, and Michael Gratzel. Tris(2-(1h-pyrazol-1-yl)pyridine)cobalt(iii) as p-type dopant for organic semiconductors and its application in highly efficient solid-state dye-sensitized solar cells. *Journal of the American Chemical Society*, 133(45):18042–18045, 2011. 16

[23] U Bach, P Comte, J E Moser, F Weisso, and Michael Gratzel. Solid-state dye-sensitized mesoporous TiO_2 solar cells with high photon-to-electron conversion efficiencies. *Nature*, 395:583–585, 1998. 16

[24] Qingjiang Yu, Yinghui Wang, Zhihui Yi, Ningning Zu, Jing Zhang, Min Zhang, and Peng Wang. High-efficiency dye-sensitized solar cells: The influence of lithium ions on exciton dissociation, charge recombination, and surface states. *ACS Nano*, 4(10):6032–6038, 2010. 16

[25] B. Wenger, M. Gratzel, and J. E. Moser. Rationale for kinetic heterogeneity of ultrafast light-induced electron transfer from ru(ii) complex sensitizers to nanocrystalline TiO_2. *J. Am. Chem. Soc*, 127(35):12150–12151, 2005. 0002-7863. 16

[26] Priti Tiwana, Patrick Parkinson, Michael B. Johnston, Henry J. Snaith, and Laura M. Herz. Ultrafast terahertz conductivity dynamics in mesoporous TiO_2 : Influence of dye sensitization and surface treatment in solid-state dye-sensitized solar cells. *J. Phys. Chem. C*, 114(2):1365–1371, 2010. 16

[27] Daibin Kuang, Cedric Klein, Henry J. Snaith, Jacques-E Moser, Robin Humphry-Baker, Pascal Comte, Shaik M. Zakeeruddin, and Michael Gratzel. Ion coordinating sensitizer for high efficiency mesoscopic dye-sensitized solar

cells: Influence of lithium ions on the photovoltaic performance of liquid and solid-state cells. *Nano Letters*, 6(4):769–773, 2006. PMID: 16608281. 16

[28] J.E. Kroeze, N. Hirata, L. Schmidt-Mende, C. Orizu, S.D. Ogier, K. Carr, M. Gratzel, and J.R. Durrant. Parameters influencing charge separation in solid-state dye-sensitized solar cells using novel hole conductors. *Advanced Functional Materials*, 16(14):1832–1838, 2006. 16

[29] Francisco Fabregat-Santiago, Juan Bisquert, Le Cevey, Peter Chen, Mingkui Wang, Shaik M. Zakeeruddin, and Michael Gratzel. Electron transport and recombination in solid-state dye solar cell with spiro-ometad as hole conductor. *J. Am. Chem. Soc.*, 131(2):558–562, 2009. 16

[30] J. van de Lagemaat and A. J. Frank. Nonthermalized electron transport in dye-sensitized nanocrystalline TiO_2 films: Transient photocurrent and random-walk modeling studies. *The Journal of Physical Chemistry B*, 105(45):11194–11205, 2001. 16

[31] Jarl Nissfolk, Kristofer Fredin, Anders Hagfeldt, and Gerrit Boschloo. Recombination and transport processes in dye-sensitized solar cells investigated under working conditions. *The Journal of Physical Chemistry B*, 110(36):17715–17718, 2006. 17

[32] Henry J. Snaith, Robin Humphry-Baker, Peter Chen, Ilkay Cesar, Shaik M. Zakeeruddin, and Michael Gratzel. Charge collection and pore filling in solid-state dye-sensitized solar cells. *Nanotechnology*, 19(42), 2008. 17, 20

[33] Juan Bisquert. Chemical diffusion coefficient of electrons in nanostructured semiconductor electrodes and dye-sensitized solar cells. *The Journal of Physical Chemistry B*, 108(7):2323–2332, 2004. 18, 19

[34] Janne Halme, Gerrit Boschloo, Anders Hagfeldt, and Peter Lund. Spectral characteristics of light harvesting, electron injection, and steady-state charge collection in pressed TiO_2 dye solar cells. *The Journal of Physical Chemistry C*, 112(14):5623–5637, 2008. 20

Chapter 3

Experimental methods and setup

3.1 Device Assembly

3.1.1 FTO glass preparation

Fluorine doped tin oxide ($15\,\Omega\square^{-1}$, Pilkington) was used as received and cut down to a square with a side of 11.2 cm with a diamond scribe. The cut sheet was then selectively etched with Zn powder and a solution of 2.4 M HCl. To achieve the required etched pattern, the areas where the FTO must be preserved were covered with scotch tape. A schematic of this procedure is shown in Figure 3.1. Following the removal of the FTO in the required areas, the sheet was then washed with copious amounts of de-ionized water. After this step, the sheet was brushed with a toothbrush and a 2% solution of Hellmanex (Sigma Aldrich) and then rinsed again with de-ionized water. After the substrates were dried, they were rinsed with acetone, dried again, rinsed with ethanol and dried one final time. Once the substrates were cleaned and dried, they were subjected to a 10 minute oxygen plasma treatment.

3.1.2 Metal oxide compact layer deposition

After the substrates have been plasma etched, a compact layer of the same metal oxide as the one that will be used as the mesoporous photoanode is deposited via spray pyrolysis. The 3 metal oxides used in this work are ZnO, SnO_2 and TiO_2:

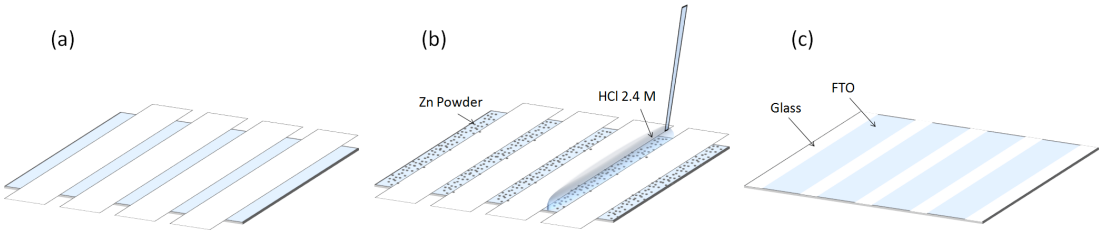

Figure 3.1: FTO Etching procedure schematic. (a) Sheet with the scotch tape set up in the required pattern. (b) Sheet after sprinkling Zn powder and applying a small quantity of HCl. (c) Sheet after etching.

3.1.2.1 TiO_2

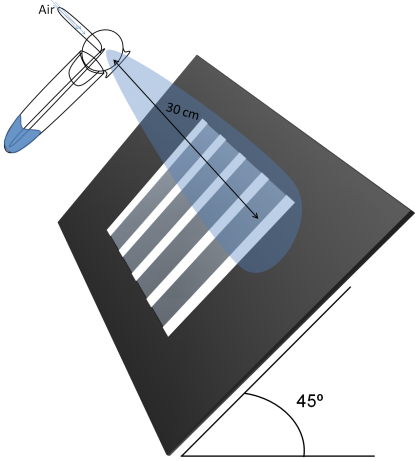

Figure 3.2: Spray pyrolysis schematic.

Firstly, 6.6 mL of a solution of Titanium diisopropoxide bis(acetylacetonate) 75% by weight in Isopropanol (Sigma Aldrich) in anhydrous ethanol was prepared in a 1:10 Ti-Acac:ethanol volumetric ratio.[1, 2] The solution was prepared fresh each time a maximum of 30 minutes before use. Meanwhile, the substrate was heated on a hotplate tilted to 45°C to a temperature of 250°C. Once the temperature is reached and after a wait of 10 min, the whole solution was sprayed by hand in a pattern where the handpump was pressed twice while aiming at each corner and after doing all corners, 10 seconds were left between cycles. The height of the sprayer was kept constant by the use of a clamp, and it was angled in such a way as to spray directly perpendicular to the substrate. A schematic representation is shown on figure 3.2. After the whole solution has been sprayed, the substrates were left at 250°C for 20 minutes and then it was left to cool naturally to room temperature.

3.1.2.2 SnO_2

The setup and spraying pattern were kept as the previous section. Two 6.6 mL solutions of Butyltin trichloride (Sigma Aldrich 95%) in anhydrous ethanol were prepared in a 1:10 precursor:ethanol volumetric ratio. The substrates were heated to a temperature of 450°C and left at this temperature for 20 min. After this waiting period is completed, the first precursor solution was sprayed in the usual pattern. After this step is done, 10 min were waited and then the hotplate was allowed to cool down naturally to 250°C. Once this temperature is reached, the second precursor solution was sprayed in the usual pattern. Finally, after 10 min, the hotplate was allowed to cool naturally to room temperature.

3.1.2.3 ZnO

The setup and spraying pattern were kept as the previous section. A 6 mL, 100 mM solution of Zinc acetate dihydrate (Sigma Aldrich 99.999%) in anhydrous methanol was prepared.[3] The substrates were heated to a temperature of 350°C and left at this temperature for 20 min. After this waiting period is completed, the precursor solution was sprayed in the usual pattern. After this step is done, 10 min were waited and then the hotplate was allowed to cool down naturally to room temperature.

3.1.3 Mesoporous paste deposition

After spray pyrolysis deposition of the compact layer, the substrates were plasma etched for 1 minute and then the mesoporous paste was screen-printed with a stripe 8mm wide across the center of all substrates. Depending on the metal oxide used, the procedure for preparing the paste must be tuned to achieve the correct thickness. After the paste deposition is completed, the substrates were subjected to an ethanol-rich atmosphere for periods between 20 and 90s to homogenize the top layer. Once this step is completed, the substrates were placed for 5 minutes on a hotplate at 135°C. The substrates are then calcinated at 500°C in an oven with a slow ramp that reaches this temperature after 3 hours and then are allowed to cool down naturally to room temperature. The substrates may be collected at this stage and kept in the drawer indeterminably with no negative consequences.

3.1.3.1 TiO_2 transparent paste

Dyesol paste 18NR-T is composed of ∼20 nm anatase TiO_2 nanoparticles in a mixture of ethyl cellulose and terpineol. This paste was diluted down with terpineol to a ratio of 0.3:1 terpineol:paste by weight. The resulting mixture was then stirred manually until it visually looked homogeneous and then was allowed to mix for 24h in an automatic shaker. The films prepared from this paste and with a mesh termed T120, which refers to the number of threads per inch, by the supplier (Mascoprint) which results in thicknesses of between 1.8 and 2 μm which are the optimum thickness for the dyes used.

3.1.3.2 TiO_2 block copolymer-derived paste

The powder from the calcined block copolymer-derived mesostructure was processed into a paste in a similar way as described by Ito et al.[4] (quantities quoted are for 1 g of TiO_2 powder). The TiO_2 powder was ground lightly in an alumina mortar for 10 seconds dry and for a further 1 second after the addition of 167 μl of acetic acid. 833 μl of deionized water was added and then the powder was ground for further 30 seconds. The paste was then transferred into a vial after adding 16 ml of ethanol. This solution was stirred with a magnetic stirrer for 1 minute and then sonicated with an ultrasonic probe 15 times with an interval of 2 seconds on, 2 seconds off. 3.33 g of α-terpineol was added and the paste was again stirred for 1 minute and then sonicated following the same procedure. Finally 5 g of a 10 weight-% solution of ethyl-cellulose (1:1, 10000cps:46000 cps) and ethanol were added, stirred and sonicated. The paste was then heated to 60°C for 24 h in air to evaporate the ethanol, and then redispersed in ethanol at a concentration of 1 ml ethanol per 1 g of paste, which was then further diluted down with ethanol to different concentrations to obtain a range of final film thicknesses.

3.1.3.3 SnO_2 paste

The SnO_2 paste was prepared from <100 nm particle size SnO_2 nanopowder (Sigma-Aldrich) in a similar way as Ito et al.[4] (amounts are for 1.6g of powder): The powder was ground in an alumina mortar for 1 minutes dry and for a further minute second after the addition of 167 μl of acetic acid. 833 μl of deionized

water was added and then the powder was ground for a further 5 minutes. After this point, ethanol was slowly added in 2 mL steps every 2 to 5 minutes to ensure the correct paste consistency to be able to grind the macro-aggregates. After 1 hour or until no more macro-aggregates are visible, the paste was then transferred into a vial after adding 20-30 ml of ethanol. This solution was stirred with a magnetic stirrer for 1 minute and then sonicated with an ultrasonic probe 30 times with an interval of 2 seconds on, 2 seconds off. 3.33 g of anhydrous terpineol (Sigma Aldrich) was added and the paste was again stirred for 1 minute and then sonicated following the same procedure. Finally 4 g of a 10 weight-% solution of ethyl-cellulose (1:1, 10000cps:46000cps) and ethanol were added, stirred and sonicated. The paste was then rotavaped to eliminate the ethanol from the mixture.

3.1.3.4 ZnO paste

20g of a zinc oxide dispersion (Sigma-Aldrich 40%wt in ethanol) was weighed out and 1.2 ml of butylamine was added and stirred with a magnetic bar for 5 minutes. 20g of anhydrous terpineol (Sigma-Aldrich) was added and stirred for another 5 minutes. 30g of a 10 weight-% solution of ethyl-cellulose (1:1, 10000cps:46000cps) and ethanol were added and stirred for a further 5 minutes. The mixture was then sonicated with an ultrasonic probe, operated for a total sonication time of 2 minutes, cycling 2 seconds on, 2 seconds off. Finally the mixture was rotavaped to remove all the ethanol.

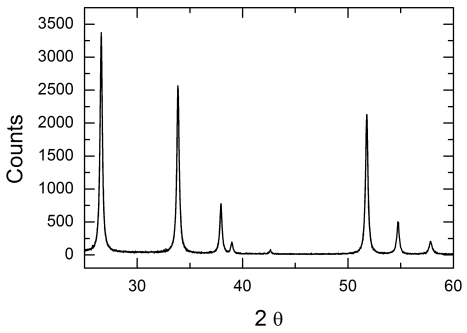

Figure 3.3: XRD data for the SnO_2 powder used in the fabrication of the solar cells. Scherrer analysis indicates that the crystallite size is ∼35 nm

3.1.3.5 Al_2O_3 paste

An aluminum oxide dispersion was purchased from Sigma-Aldrich (10%wt in water) and was washed in the following manner: it was centrifuged at 7500 rpm for 6h, and redispersed in absolute ethanol 99.8%+ (Fisher Chemicals) with an ultrasonic probe, operated for a total sonication time of 5 minutes, cycling 2 seconds on, 2 seconds off. The rinsing process was repeated 3 times. After washing 3 times, for every 10 g of the original dispersion (1g total Al2O3) the following was added: 3.33 g of α-terpineol and 5g of a 50:50 mix of ethyl-cellulose 10 cP and 46 cP purchased from Sigma Aldrich in ethanol, 10% by weight. After the addition of each component, the mix was stirred for 2 minutes and sonicated with the ultrasonic probe for 1 minute of sonication, using a 2 seconds on 2 seconds off cycle. The resulting mixture was introduced in a Rotary evaporator to remove excess ethanol to a concentration suitable to obtain between 50 to 400 nm thick films when spin-coating or doctor blade coating.

3.1.4 Surface treatment

After calcination, the sheet is cut down with a diamond scribe to the correct size, i.e. 1.4x1.4cm squares. Depending on the material used, different surface treatments were performed to grow a thin layer of the following oxides.

3.1.4.1 TiO_2 treatment

A 2M stock solution of $TiCl_4$ was diluted down to 15 mM with de-ionized water. The substrates were immersed in this solution for 1 hour at 70°C, then they were submerged in clean de-ionized water for 1 minute and then left standing on their edge to dry for 5 minutes.[5, 6] After drying the substrates, they were left on a hotplate at 100°C for 10 minutes and subsequently were resintered at 500°C for 45 minutes then left to cool down naturally to 70°C.

3.1.4.2 MgO treatment

A 20 mM solution of magnesium acetate tetrahydrate was prepared in absolut ethanol (Fisher Chemicals) at a 20 mM concentration. Then, a weighing bottle

with an airtight lid was warmed in a hotplate at 100°C for 3 minutes, after which time the Mg-acetate solution was added and the bottle was closed. The mixture was allowed to warm up until the solution is boiling, which generally occurs within 5 minutes with the lid on. Once the mixture is boiling, the lid is removed and the substrates are placed inside this chemical bath for exactly one minute unlidded. Once the substrates are removed, they were left to drip on their edge, after which they were rinsed in a cold ethanol solution for up to a minute of time. After rinsing, the substrates were immediately dried with an air gun before placing them on a hotplate which was left at 100°C for 10 minutes and subsequently ramped to either 500°C for SnO_2-based devices or 400°C for ZnO-based devices for 45 minutes then left to cool down naturally to 70°C.

3.1.4.3 Hydrothermal MgO treatment

Two solutions were prepared: a 50 mM magnesium nitrate hexahydrate (99.999% Sigma Aldrich) aqueous solution and an 80 mM sodium hydroxide (99.99 % Sigma Aldrich) aqueous solution.[7] After stirring for 10 minutes with a magnetic stirrer, both solutions were added at a 1:1 volume ratio and finally the substrates were immersed.[1] The vessels were then placed on a hotplate at 150°C for 20 minutes, at which point the substrates were removed and submerged in clean de-ionized water for 1 minute, then left for 5 minutes to dry standing on their edges. After the substrates were dried, they were left on a hotplate at 100°C for 10 minutes and subsequently were resintered at either 500°C for SnO_2-based devices or 400°C for ZnO-based devices for 45 minutes then left to cool down naturally to 70°C.

3.1.4.4 Hydrothermal Y_2O_3 treatment

Two solutions were prepared: a 50 mM yttrium nitrate hexahydrate (99.8 % Sigma Aldrich) aqueous solution and an 80 mM sodium hydroxide (99.99 % Sigma Aldrich) aqueous solution.[8] After stirring for 10 minutes with a magnetic stirrer, both solutions were added at a 1:1 volume ratio and finally the substrates were immersed. The vessels were then placed on a hotplate at 150°C for 20 minutes,

[1] The solution is initially clear but quickly goes cloudy. After the treatment is complete, there usually are big particulates floating on the bottomo of the vessel

at which point the substrates were removed and submerged in clean de-ionized water for 1 minute, then left for 5 minutes to dry standing on their edges. After the substrates were dried, they were left on a hotplate at 100°C for 10 minutes and subsequently were resintered at either 500°C for SnO_2-based devices or 400°C for ZnO-based devices for 45 minutes then left to cool down naturally to 70°C.

3.1.5 Dyeing

After the substrates have been resintered and left to cool down to 70°C, they must be immediately submerged in the dye solution for 1 hour. The dyes used in the work in this thesis are termed D102, D149[9] and C220[10]. The chemical composition of these dyes is given in figure 3.4. To prepare these solutions, first a 1:1 mixture of anhydrous acetonitrile (Sigma Aldrich) and *tert*-butanol (Sigma Aldrich) is prepared. This solution is then added in a 1mg of dye per 10mL of solution ratio for D102 and D149 dyes, and at a 1mg per 20mL of solution for C220 dye. To the D149 solution, chenodeoxycholic acid (97% Sigma Aldrich) was added in a 1:1 molar ratio, i.e. 0.53 mg per 10 mL of solution.

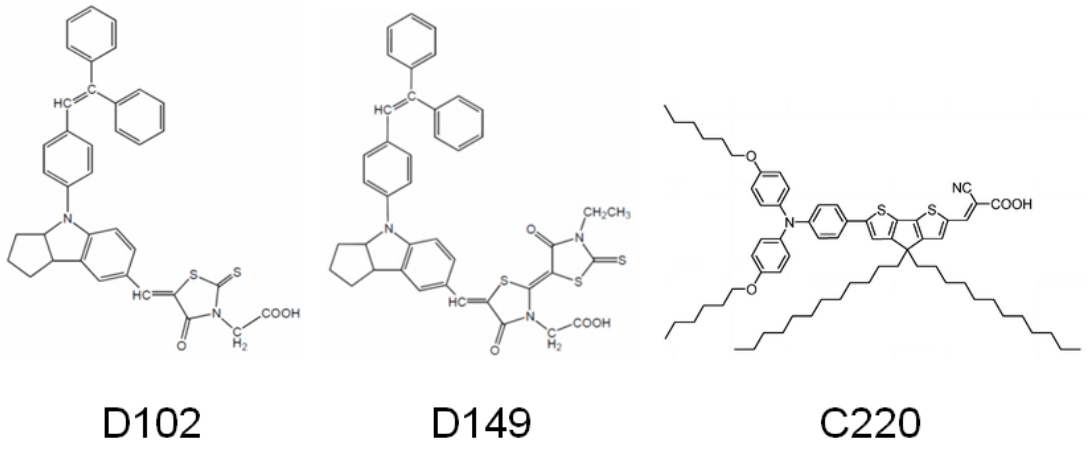

Figure 3.4: Chemical composition of the dyes used in this study.

3.1.6 spiro-OMeTAD filling and electrode deposition

2,2',7,7'-tetrakis(N,N-di-p-methoxypheny-amine)-9,9'-spirobifluorene (Spiro-OMeTAD) [11] purchased from LumTech or Merck was dissolved in anhydrous chloroben-

zene (Sigma Aldrich) at a typical concentration of 10% by volume, although adjustements were made for thinner or thicker films. After fully dissolving the hole transporter, 4-*tert*-butyl pyridine (*t*BP) was added with a volume to mass ratio of 1:26 l mg^{-1} *t*BP:spiro-OMeTAD. Lithium bis(trifluoromethylsulfonyl)imide salt (Li-TFSI) was pre-dissolved in acetonitrile at 170 $mgml^{-1}$ and added to the hole transporter solution at 1:12 lmg^{-1} of Li-TFSI solution:Spiro-OMeTAD.[12] The dyed films were rinsed briefly in acetonitrile and dried in air for 1 minute. For spin-coating, a small quantity of the hole transporter solution (18-25 μl) was dispensed onto each substrate and left to wet the films for 20 s before spin-coating at 700 rpm for 40 s in air. The films were left overnight in an air atmosphere before placing them in a thermal evaporator where 150 nm thick silver electrodes were deposited through a shadow mask under high vacuum (10^{-6} mbar).

3.1.7 Liquid electrolyte filling

The home-made robust Z646 electrolyte used was composed of a mixture of 0.8M 1-propyl-3-methylimidazolium iodide, 0.15M Iodine, 0.5M 1-methylbenzimidazole, 0.1M guanadinium thiocyanate, in 3-methoxypropionitrile.[13] After being washed by acetonitrile and dried under air flow, the sensitized electrodes were assembled with the counter electrode by melting a 25 μm thick Surlyn gasket. To prepare the platinum coated counter electrode, first a hole was sandblasted into an FTO slide. A drop of 5 mM (H_2PtCl_6) ethanolic solution was then spread over the FTO and then it was heated to 400°C during 15 min under air. The internal space between the working and the counter electrodes was filled with Z646 electrolyte using a vacuum back-filling system. The hole was finally clogged with a melted surlyn sheet and a thin cover slide.

3.2 Dye desorption

The mesoporous films were sensitized with a Ru-based dye, termed Z907,[14] overnight. Then, they were submerged in 4 ml of a 200 mM solution of potassium hydroxide in methanol for over 24h. The absorption spectrum was then recorded with a cary uv-vis spectrometer. Taking into account the Beer-Lamber law ($T =$

$10^{\epsilon lc}$), and knowing the extinction coefficient of the dye (12000 $\mathrm{Lmol^{-1}cm^{-1}}$), the number of dye molecules attached to the mesoporous structure can then be calculated.

3.3 spiro-OMeTAD density calculation

To obtain the density of Spiro-OMeTAD, films were spin cast from chlorobenzene on glass slides. Film thicknesses were measured using a Dektak 150 surface profiler, and the glass was cut after coating with spiro-OMeTAD in order to remove any edges where increased film thickness is often observed and potential coating of the sides, or even underside of the slides. The areas of the films were then measured using high resolution photography, allowing the volume of each film to be calculated accurately. The Spiro-OMeTAD was then re-dissolved in a known volume of chlorobenzene and UV-visible absorption spectra were taken for the resulting solutions. From this the molar extinction coefficient ϵ for a given wavelength could be obtained via the Beer-Lambert law $A = c\epsilon l$,[15] where A is absorbance, c solution concentration and l the optical path length. By comparing the spectra from the dissolved films at the same wavelength, the concentration and hence the mass of Spiro-OMeTAD originally in the film can be attained, and since the film volume is also known, the density can be deduced.

3.4 Block copolymer assembly

3.4.1 Diblock copolymer paste assembly

3.45 mL of 37% HCl were rapidly added to 5 mL of titanium ethoxide in a beaker at 50 C under stirring. The resulting sol was left to age for 90 minutes. In a separate vial, 0.1 g of PI-*b*-PEO copolymer (Mn=33.5 kg/mol, polydispersity 1.03, 23 wt% PEO) was dissolved in 7 mL of THF. The appropriate amount of the sol was added into the polymer solution to adjust the ratio of final (calcined) TiO_2 to added polymer by weight, to the three ratios 2:1, 1:1, and 1:3. For example, for titania 2:1, 0.873 ml sol was mixed with 0.1g PI-*b*-PEO in 7 ml THF. The solution was left to dry in air at 50°C. The dry material was then

redissolved in a toluene and 1-butanol mixture where the ratio of the to solvents was adjusted to match the PI:(PEO+sol) weight fraction (for example for titania 2:1, the mixture consisted of 0.81 ml toluene and 0.61 ml 1-butanol). Finally, the solution was cast into a PTFE dish and left in air at 50°C for over 24 hours. The resulting material was heated slowly (5 °C per minute) to 500°C, calcined for 1 hour at 500°C, and then left to cool down over 4 hours.

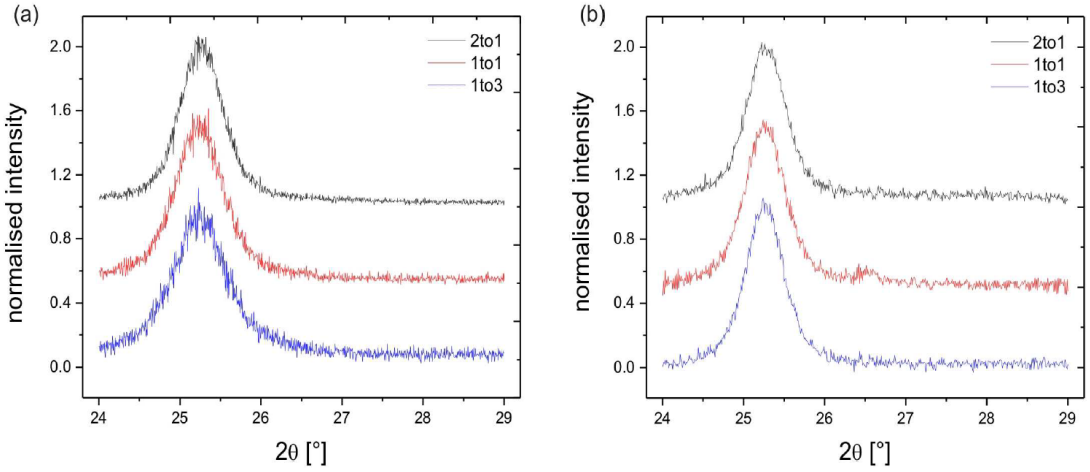

Figure 3.5: Wide-angle X-ray scattering of calcined titania (a) before and (b) after paste processing. For better comparison between titania 2:1 (top), titania 1:1 (middle) and titania 1:3 intensities were normalized. Crystal sizes of the materials were determined by fitting the anatase (101) peak with a Voigt function and subsequently correlating the peak broadening to nanocrystallinity via the Debye-Scherrer equation with a K value of 0.89. I acknowledge that this data was collected by Stefan Guldin in the University of Cambridge.

3.4.2 Diblock copolymer derived film

TiO_2 electrodes were fabricated as follows: 0.4 g of a poly(isoprene-*b*-ethylene oxide) block-copolymer (PI-*b*-PEO) (molecular weight M_n = 34.4 kg/mol, 28 wt% PEO) was dissolved in 8 ml of an azeotrope solvent mixture of toluene (72.84 w%) and 1-butanol (27.16 w%). A titanium-containing sol was prepared separately by the addition of 1.54 ml titanium(IV) isopropoxide (Sigma Aldrich, 99.999% trace metals basis) to 0.49 ml hydrochloric acid (37%) under vigorous stirring. 5 min after addition of the titania precursor, the sol was added to the

polymer solution and subsequently stirred for a further 30 min. Hybrid were then deposited from solution via spin coating (1800 rpm, 20 s) or doctor blading onto the prepared FTO substrates. Subsequently the films were exposed to an annealing protocol on a calibrated hotplate (2000 W with programme regulator, Harry Gestigkeit GmbH), typically for 10 min at 50°C, followed by a 45 min linear heating ramp to 300°C and a final dwell time of 5 min at this temperature. The procedure of film deposition and subsequent annealing was repeated several times (typically 3-7 cycles) to match the required film thickness. Finally the stack was calcined at 600°C (3 hours, heat ramp 5 °C/min, Cole Parmer, EW-33855-35) to remove the organic material and crystallize the TiO_2.

3.4.3 Triblock terpolymer derived film

A polymer solution was prepared by dissolving 50 mg of ISO (M_n=14.63, 29.04, and 9.77 kg/mol for I, S, and O, respectively, with a polydispersity of 1.05) in 0.61 mL of anhydrous anisole for at least 1h. In a separate vial a sol stock solution was prepared by quickly adding 5 mL of titanium isopropoxide to 1.6 mL of concentrated 37 wt% HCl(aq) under rapid stirring. Caution must be taken since this addition is violently exothermic and can cause splashing. The closed vial containing the dilute sol stock solution was stirred for 5 min followed by the addition of 10 mL of dry tetrahydrofuran and two additional minutes of stirring. Next, 0.22 mL of the dilute sol stock solution was added to the polymer solution followed by 30 minutes of shaking. The quantity of titania sol added was chosen to correspond to c.a. 27.5 vol% for the combined PEO and titania volume in order to target the network morphology window [16, 17]. Films were prepared by doctor blading the final solution onto an FTO substrate with a preformed titania compact layer deposited via spray-pyrolysis. The wet films were allowed to dry on hotplates set to 30°C for 1-2 days. The dry films were aged at 100°C for 3 days to further the condensation reaction and then were calcined at 500°C with a 1°C/min heating ramp followed by a 1 h hold and natural furnace cooling.

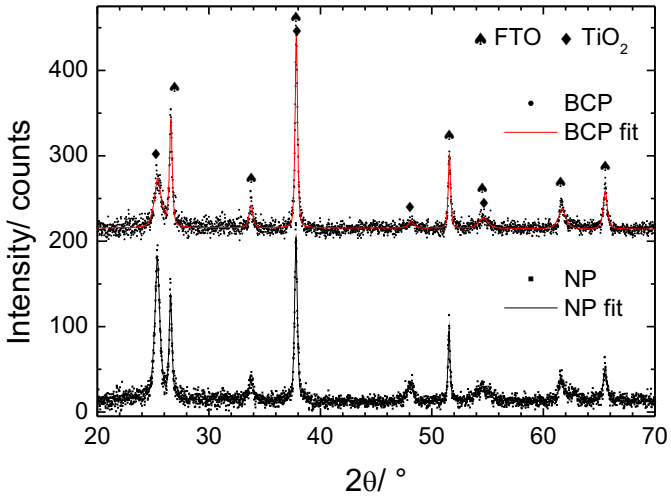

Figure 3.6: Wide-angle X-ray diffraction of different photoanodes. Top: Diffraction data and fit of triblock terpolymer assembled photoanodes. Bottom: diffraction data and fit for conventional nanoparticle photoanodes. For clarity, the expected peak position of TiO_2 anatase (PDF 711167, ♦) and FTO (♠) are indicated. These are expected to be the main contribution from the mesoporous photoanode and the transparent conductive substrate respectively. I acknowledge that Robert Gunning in the University of Oxford collected and analyzed the data presented in this figure.

3.5 Materials characterization

TEM samples of the block copolymer PI-b-PEO/TiO_2 mesostructure were prepared by sectioning the bulk materials to 50nm with a Leica Ultracut UCT cryo-ultramicrotome and transferring the slices onto copper TEM grids. These samples were imaged in a Tecnai T12 Spirit TEM with an acceleration voltage of 120keV. Scanning electron microscopy of processed titania films and devices was carried out on a Leo Ultra 55 with a field emission source of 3 kV acceleration voltage. Ellipsometric data was taken on a Nanofilm ep3se imaging ellipsometer and the instrument software was used to analyze the data. Results by imaging ellipsometry were verified with a spectroscopic ellipsometer (Woollam alpha-SE). SAXS patterns were recorded in the G1 beamline in Cornell High Energy Synchrotron Source (CHESS) with a Flicam 2D CCD detector, with the beam energy at 10.5

keV and the sample-to-detector of 2.3 m. Wide-angle x-ray diffraction was carried out on a PANalytical MPD Pro using monochromatic $CuK_{\alpha 1}$ radiation, using an X'Celerator linear detector.

3.6 Transient photovoltage and photocurrent decay measurement setup

To perform transient photovoltage and photocurrent decay measurements, first, three arrays of diodes: white (Lumiled Model LXHL-NWE8 white star), red (LXHLND98 red star) and green (LXHL-NM98 green star); were soldered and screwed into a home-made holder. A schematic is shown with the distribution of the arrays in figure 3.7. To select either green or red perturbation, a USB controllable relay board was used (KMtronic), and a transistor (IRF7821PbF) was used to determine the length of the pulse. The white light array is connected to a PC controllable power supply (TTi TQ355TP) at a constant current setting, while the perturbation array is connected at a constant voltage setting. In this way, a wave generator (Agilent 33220A) connected to the transistor switches the transistor on or off, and the light can be pulsed. The solar cell is then situated in the center of the beam and connected to an oscilloscope (Agilent InfiniiVision 6000 Series), while it is triggered by the wave generator so the photoresponse can be recorded. The whole system is controlled by LabView to acquire the data automatically.

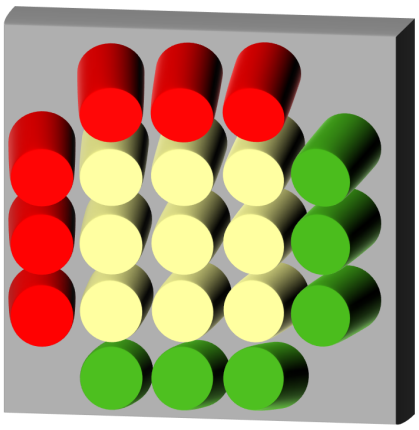

Figure 3.7: LED array setup schematic

The LED response to the pulse generated by the wave generator was recorded for different time scales in figure 3.8. As can be seen on b), the transistor has a switching time in the order of 25 ns, and the LEDs turn on to about 70-80% intensity within 200ns. However, the system does not reach equilibrium until 10

μs after switching the transistor on, which is several orders of magnitude faster than the response of most solid-state dye-sensitized solar cells.

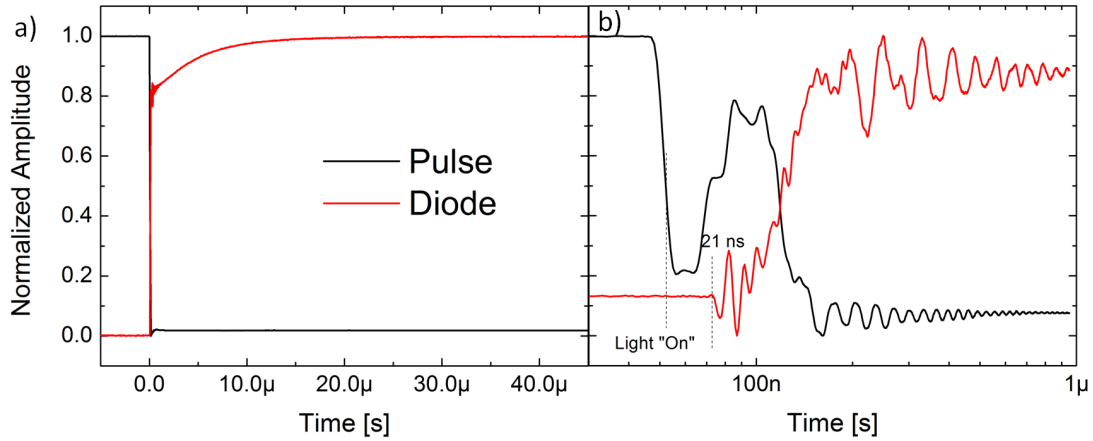

Figure 3.8: LED response measured on a fast silicon diode to the pulse generated by the wave generator for a) long times and b) short times. The pulse has been turned upside down for clarity.

3.6.1 Calculations of charge density

3.6.1.1 Open circuit

Once the DOS is known, as shown in figure 2.8, the resulting points can be fit assuming an exponential distribution of states as:

$$C = \frac{dQ}{dV} \tag{3.1}$$

$$C = Ae^{BV} \tag{3.2}$$

$$\int_0^Q dQ = \int_0^V CdV = \int_0^V Ae^{BV}dV \tag{3.3}$$

$$Q = \frac{A}{B}(e^{VB} - 1) \tag{3.4}$$

3.6.1.2 Short circuit

There are two ways to extract the charge density of the films at short circuit conditions: by performing complete short circuit current decays, i.e. charge ex-

traction, or through extrapolation from small perturbation short circuit current decays. In the first method, the complete photocurrent decay from a background light intensity to complete darkness is measured in an oscilloscope. The total charge in the film is then the result of calculating the area under the resulting curve.

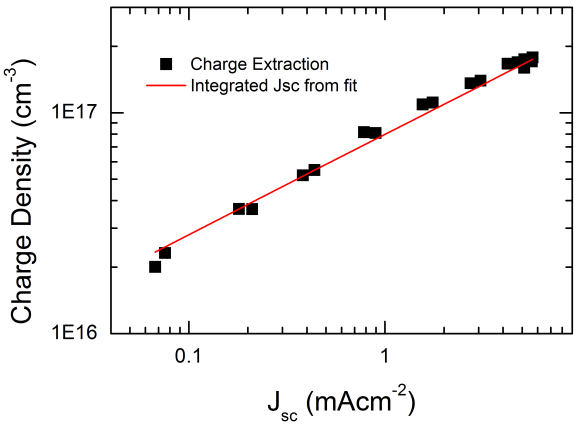

Figure 3.9: Measured extracted charge against short circuit current for standard 1.8 μm thick solid-state cells. Line corresponds to the integrated charge derived directly from the decay lifetimes of the small perturbation transient photocurrent decay measurements and using equation 3.7.

For the second method, the small perturbation transport lifetime ($\tau(J)$) against short circuit current (J) for a range of background light intensities was fit as a power law:[18]

$$\tau(J) = AJ^B \tag{3.5}$$

After establishing the relationship between short circuit current and transport lifetime, the current density can be calculated iteratively as:

$$J = J_0 e^{\frac{-t}{\tau(J)}} \tag{3.6}$$

$$J_0 = J_0 e^{\frac{0}{\tau(J)}} = J_0$$

$$J_1 = J_0 - \Delta J_0$$

$$J_2 = J_1 - \Delta J_1$$

$$\vdots$$

$$J_{n+1} = J_n - \Delta J_n \tag{3.7}$$

$$\Delta J_n = J_n(t) - J_n(t + \Delta t) = J_0 e^{\frac{-t}{\tau(J)}} - J_0 e^{\frac{-(t+\Delta t)}{\tau(J)}}$$

$$\Delta J_n = J_n(1 - e^{\frac{-\Delta t}{AJ_n^B}}) \tag{3.8}$$

The resulting values for the short circuit current can then be integrated to find the charge density. To check whether this method is a good approximation to the charge density of the films, the complete photocurrent decay from different background light intensities to complete darkness were measured and integrated to find the charge density, as shown in figure 3.9. The calculations almost perfectly follow the charge density extracted from the film via complete short circuit decays, confirming that this is a viable technique to obtain the charge density at short circuit conditions.

References

[1] Ladislav Kavan and Michael Gratzel. Highly efficient semiconducting TiO_2 photoelectrodes prepared by aerosol pyrolysis. *Electrochimica Acta*, 40(5):643–652, 1995. 26

[2] Petra J. Cameron and Laurence M. Peter. Characterization of titanium dioxide blocking layers in dye-sensitized nanocrystalline solar cells. *The Journal of Physical Chemistry B*, 107(51):14394–14400, 2003. 26

[3] F. Paraguay D, W. Estrada L, D. R. Acosta N, E. Andrade, and M. Miki-Yoshida. Growth, structure and optical characterization of high quality zno

thin films obtained by spray pyrolysis. *Thin Solid Films*, 350(12):192–202, 1999. 27

[4] S. Ito, P. Chen, P. Comte, M. K. Nazeeruddin, P. Liska, P. Pechy, and M. Gratzel. Fabrication of screen-printing pastes from TiO_2 powders for dye-sensitised solar cells. *Progress in photovoltaics*, 15(7):603–612, 2007. 28

[5] P. M. Sommeling, B. C. O'Regan, R. R. Haswell, H. J. P. Smit, N. J. Bakker, J. J. T. Smits, J. M. Kroon, and J. A. M. van Roosmalen. Influence of a $TiCl_4$ post-treatment on nanocrystalline TiO_2 films in dye-sensitized solar cells. *The Journal of Physical Chemistry B*, 110(39):19191–19197, 2006. 30

[6] Brian C. O'Regan, James R. Durrant, Paul M. Sommeling, and Nicolaas J. Bakker. Influence of the $TiCl_4$ treatment on nanocrystalline TiO_2 films in dye-sensitized solar cells. 2. charge density, band edge shifts, and quantification of recombination losses at short circuit. *The Journal of Physical Chemistry C*, 111(37):14001–14010, 2007. 30

[7] N. O. V. Plank, H. J. Snaith, C. Ducati, J. S. Bendall, L. Schmidt-Mende, and M. E. Welland. A simple low temperature synthesis route for ZnOMgO coreshell nanowires. *Nanotechnology*, 19(46):465603, 2008. 31

[8] Natalie O. V. Plank, Ian Howard, Akshay Rao, Mark W. B. Wilson, Caterina Ducati, Rajaram Sakharam Mane, James S. Bendall, Rami R. M. Louca, Neil C. Greenham, Hidetoshi Miura, Richard H. Friend, Henry J. Snaith, and Mark E. Welland. Efficient ZnO nanowire solid-state dye-sensitized solar cells using organic dyes and core-shell nanostructures. *The Journal of Physical Chemistry C*, 113(43):18515–18522, 2009. 31

[9] Tamotsu Horiuchi, Hidetoshi Miura, and Satoshi Uchida. Highly efficient metal-free organic dyes for dye-sensitized solar cells. *Journal of Photochemistry and Photobiology A: Chemistry*, 164(13):29–32, 2004. 32

[10] Ning Cai, Soo-Jin Moon, Le Cevey-Ha, Thomas Moehl, Robin Humphry-Baker, Peng Wang, Shaik M. Zakeeruddin, and Michael Gratzel. An organic d-p-a dye for record efficiency solid-state sensitized heterojunction solar cells. *Nano Lett.*, 11(4):1452–1456, 2011. 32

[11] U Bach, P Comte, J E Moser, F Weisso, and Michael Gratzel. Solid-state dye-sensitized mesoporous TiO_2 solar cells with high photon-to-electron conversion efficiencies. *Nature*, 395:583–585, 1998. 32

[12] Jessica Kruger, Robert Plass, Le Cevey, Marco Piccirelli, Michael Gratzel, and Udo Bach. High efficiency solid-state photovoltaic device due to inhibition of interface charge recombination. *Applied Physics Letters*, 79(13):2085–2087, 2001. 33

[13] Peng Wang, Cedric Klein, Robin Humphry-Baker, Shaik M. Zakeeruddin, and Michael Gratzel. Stable >= 8% efficient nanocrystalline dye-sensitized solar cell based on an electrolyte of low volatility. *Applied Physics Letters*, 86(12):123508, 2005. 33

[14] Peng Wang, Shaik M. Zakeeruddin, Jacques E. Moser, Mohammad K. Nazeeruddin, Takashi Sekiguchi, and Michael Gratzel. A stable quasi-solid-state dye-sensitized solar cell with an amphiphilic ruthenium sensitizer and polymer gel electrolyte. *Nat Mater*, 2(6):402–407, 2003. 10.1038/nmat904. 33

[15] James D. Ingle and Stanley R. Crouch. Spectrochemical analysis. *Prentice Hall 1st edition*, 1988. 34

[16] Morgan Stefik, Surbhi Mahajan, Hiroaki Sai, Thomas H. Epps, Frank S. Bates, Sol M. Gruner, Francis J. DiSalvo, and Ulrich Wiesner. Ordered three- and five-ply nanocomposites from abc block terpolymer microphase separation with niobia and aluminosilicate sols. *Chem. Mater.*, 21(22):5466–5473, 2009. 36

[17] Christopher A. Tyler, Jian Qin, Frank S. Bates, and David C. Morse. Scft study of nonfrustrated abc triblock copolymer melts. *Macromolecules*, 40(13):4654–4668, JUN 26 2007. 36

[18] Nikos Kopidakis, Kurt D. Benkstein, Jao van de Lagemaat, and Arthur J. Frank. Transport-limited recombination of photocarriers in dye-sensitized nanocrystalline tio2 solar cells. *The Journal of Physical Chemistry B*, 107(41):11307–11315, 2003. doi: 10.1021/jp0304475. 40

Chapter 4

Diblock copolymer assembled structures

4.1 Introduction

4.1.1 Block copolymers

Amphiphilic block copolymers are an excellent tool for nanotechnology.[1] They are composed of tethered polymer blocks, one hydrophilic, the other hydrophobic, which results in highly incompatible blocks, and hence a high Flory-Huggins interaction parameter[2]. Block copolymers with a high Flory-Huggins parameter will phase separate and so can be used to assemble highly ordered nanostructures, ranging from spherical, cylindrical and gyroidal to lamellar by simply changing the volume fraction of each of the blocks. See figure 4.2. The tunability of shape and scale gives unparalleled control over the resulting self-assembled morphologies. There are multiple ways of assembling structures with block copolymers. Some strategies involve creating templates from these soft materials, where one block is selectively removed while the other one is used as a scaffold allowing the backfilling of very complex structures, such as the gyroid mesophase (see fig

4.1).[3, 4]

Another approach for the synthesis of nanocomposites involves the selective incorporation of an inorganic sol into a single block of a diblock copolymer film. Pioneered by Templin et al in 1997,[5] access to predicted diblock copolymer phases were achieved through the selective swelling of an aluminosilicate sol into the poly(ethylene oxide) (PEO) phase of a block copolymer. Later, Stucky et al.[6, 7] incorporated metal-oxide sols into an ABA triblock copolymer (poly(ethylene oxide-*b*-propylene oxide-*b*-ethylene oxide), Pluronic123). The resulting transition metal oxide containing nanocomposites were subsequently heat treated in air to partially crystallize the metal oxide while oxidatively removing the polymer, producing a framework of nanocrystallites which mirrors the block copolymer directed morphology.

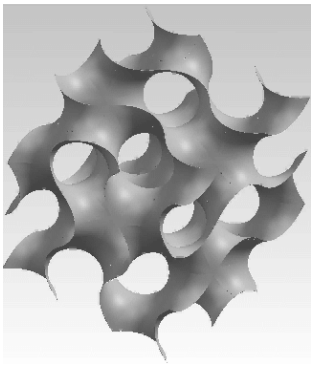

Figure 4.1: Schematic of the gyroid structure

The use of the block copolymer P123 typically limits the pore size between 6 and 14 nm, which is too small for some applications, and may impede the complete crystallization while maintaining structural integrity.[8] An alternative copolymer to use as a structure directing agent is poly(isoprene-*block*-ethylene oxide) (PI-*b*-PEO). This block copolymer offers several advantages such as structural stability at high annealing temperatures, enabling the complete crystallization of metal oxides like Nb_2O_5 or TiO_2.[9] Furthermore, pore sizes ranging from 20 to 80 nm[10] have been achieved by tuning the molecular weight of the polymer. As a consequence of the high interaction parameter between the two building blocks PI and PEO and the low glass transition temperature highly regular block copolymer morphologies such as cylinders, lamellae and gyroids have been shown for Al_2SiO_5 and Nb_2O_5.[5, 9, 11]

High performance DSCs rely upon an extremely high interfacial area, since charge carriers are only generated in the chemisorbed monolayer of photoactive dye. Charge carrier recombination in ssDSCs can be up to 2 orders of magnitude faster than in conventional liquid electrolyte devices [12, 13], so the poor electron diffusion in these random networks [14, 15, 16] combined with poor infiltration of

the solid-state hole transporters limit the titania electrode in ssDSCs to around 2 μm. This is not thick enough to achieve panchromatic light absorption with the currently available sensitizers. The block copolymer directed assembly is a particularly promising approach to photoanode architectural design since it allows control of pore size [10], crystallinity [17] and electronic properties [18] of the photoanode while being compatible with low cost and large scale production methods. In principle, following this route should enable the design of ideal photoanodes with control over both morphology and feature size provided by the block copolymer. Indeed, block copolymer derived TiO_2 has been shown to lead to enhanced electron mobilities when designed to facilitate high temperature heat treatments.[9, 19].

4.1.2 Block copolymer self-assembly

The mechanism through which the diblock copolymer PI-*b*-PEO assembles the morphology is as follows: the copolymer is formed by two blocks joined at the center, one is hydrophilic (poly ethylene oxide, PEO) and the other is hydrophobic (poly isoprene, PI). When dissolved in a polar solvent, the equivalent blocks from separate copolymers tend to join in clusters and depending on the volume fraction of each of the components, different morphologies can be achieved once the system has been let to cast in air, see figure 4.2.

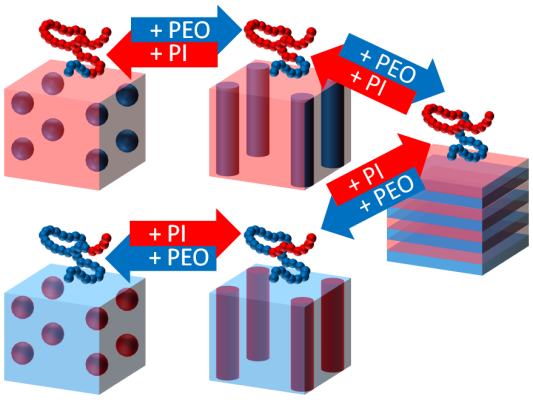

Figure 4.2: Diblock copolymer morphologies

The driving force for the self-assembly of block copolymers is the incompatibility of the covalently linked blocks of the macromolecule. This formation mechanism is then compatibilized with functional inorganic materials as introduced above, by taking advantage of selective interactions, such as hydrogen bonding, to drive sol nanoparticles into just one of the polymer blocks. The introduced TiO_2 sol particles used in this chapter are ex-

pected to preferentially reside in the hydrophilic PEO block due to attractive intermolecular forces.[20]

4.2 Block copolymers in ssDSCs

Previously, self-assembled block copolymer morphologies have been applied to the solid-state DSC: For one route, films were fabricated by spin-coating a titania sol containing diblock copolymer solution directly on the device substrate with subsequent annealing and nanocrystalline mesoporous film formation.[10] The second route involved replicating the double gyroid phase into titania by electrodeposition through a nanoporous block copolymer generated template.[3, 4] Both of these routes delivered very encouraging results, and demonstrate the range of structures achievable through block copolymer self-assembly and replication into active semiconductor devices. However, they both suffer from difficulties in making the films suitably thick, since the crystallization process occurs on the device substrate. A volume contraction during calcination induces in-plane strain which leads to the formation of cracks in thick sintered films.

Recently an alternative approach has been presented where the material calcination process was decoupled from the actual film fabrication.[21] In this case, monolithic nanocrystalline porous TiO_2 is ground down and processed into a paste to coat the substrates, forming crack-free, albeit rough, films up to many micrometers in thickness.

4.3 Results and discussion

4.3.1 Control of the titania mesostructure through PI-*b*-PEO self-assembly

Solid-state DSC devices were manufactured from mesoporous TiO_2 layers in the following fashion (see sections 3.1 and 3.4.1 for details). A PI-*b*-PEO block copolymer with a molecular weight Mn = 33.5 kg mol^{-1}, polydispersity 1.03 and a PEO weight fraction of 0.23 was dissolved in anhydrous tetrahydrofuran (THF). Ti-ethoxide in HCl was added. Following the evaporation of the solvent,

the material was calcined to anatase TiO_2 at 500 °C in air. The resulting mesoporous monolith was briefly ground to a powder (60 seconds) and processed into a paste by solvent and cellulose addition following a similar method to Ito et al.[22] albeit with only one minute grinding and brief ultrasonification. To investigate the influence of the crystallization environment on the solar cell performance, titania hybrid composites were synthesized using three different precursor to block copolymer ratios. The mixing ratios of the sol to polymer solutions were adjusted in such a way that the weight of the TiO_2 after calcination as compared to the weight of the polymer in the solution had the ratios 1:3, 1:1 and 2:1. Titania derived from the three different recipes is referred to as "titania 1:3", "titania 1:1", and "titania 2:1" in the reminder of the chapter. Figure 4.3a is a schematic illustration of the sol gel self assembly process, and Figure 4.3b-d are schematics of the block copolymer directed morphologies for titania 1:3, 1:1 and 2:1 respectively.

In Figure 4.3e, 4.3f, and 4.3g TEM images are presented of the bulk hybrid material before calcination. The 1:3 recipe yielded an array of amorphous titania cylinders surrounded by a matrix of PI. Cylinders with a differing alignment with respect to the image plane are discernible in Figure 4.3e. The 1:1 recipe (Figure 1f) resulted in an inverse micellar morphology containing PI spheres surrounded by a matrix containing both PEO and amorphous titania. Although, a lamellar morphology was expected for the 1:1 ratio, [1] [23, 24] It is suspected that the use of roughly equal portions of two selective solvents induced micellization of the polymer which resulted in toluene and PI rich micelles surrounded by a matrix rich in butanol, PEO and titania. Such a solvent induced morphology[25] could become kinetically trapped by titania condensation during the casting process resulting in an inverse micellar morphology. Finally for the 2:1 recipe in Figure 4.3g, an inverted morphology of an amorphous titania phase has formed around a well ordered array of PI cylinders. Small angle X-ray scattering (SAXS) patterns are consistent with the above findings (see Figure 4.4). Figures 4.3h, 4.3i, 4.3j show the calcined materials after heat treatment in air at 500°C. The titania 1:3

[1] A density of 2 gcm^{-3} for the TiO_2 sol within the polymer can be estimated which results in a hydrophilic volume fraction of: 0.62 for 2:1, 0.49 for 1:1 and 0.3 for 1:3 ratios; corresponding to the expected diblock copolymer phase diagrams shown in Fig.4.3 b-d.

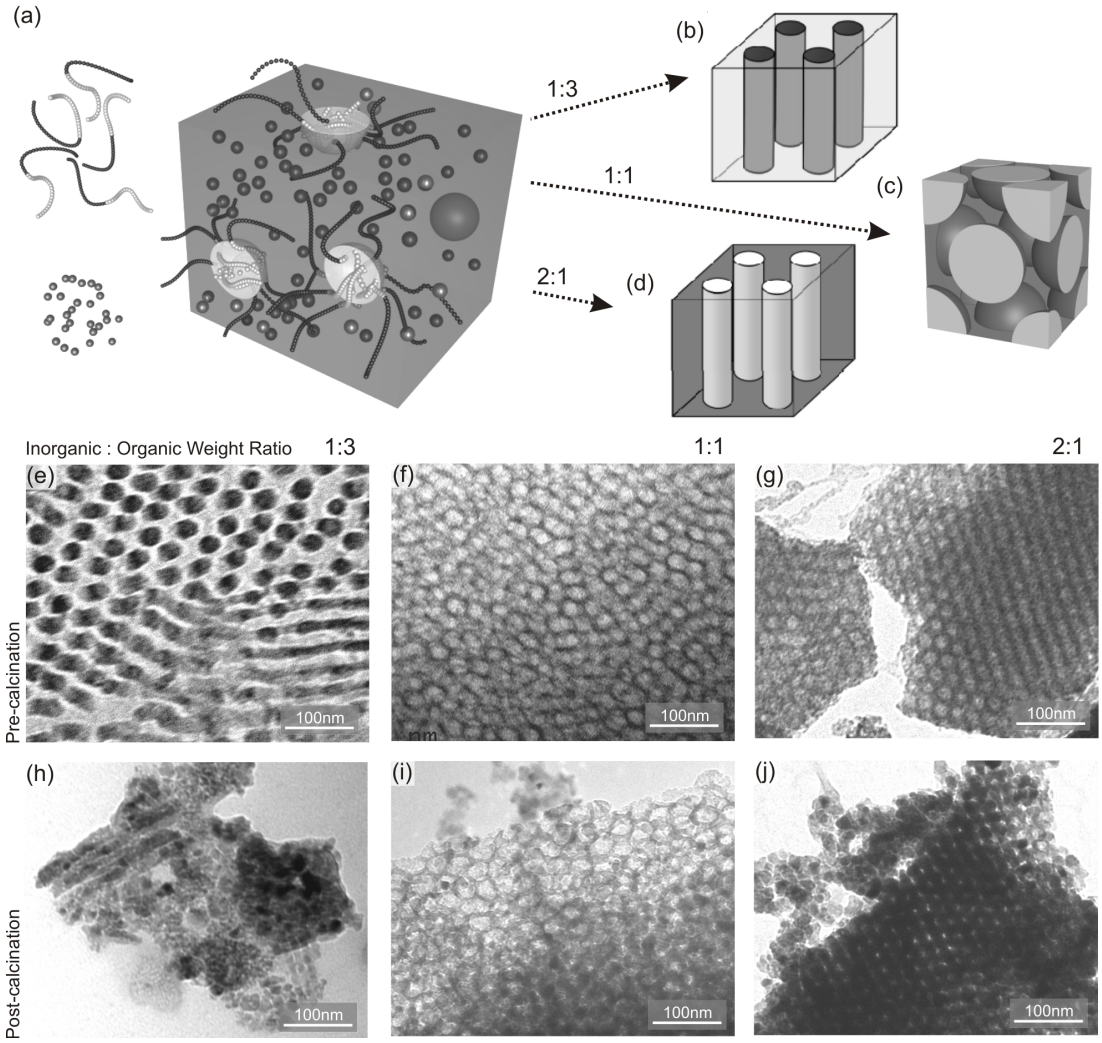

Figure 4.3: Morphologies of block copolymer directed titania before paste-processing. (a) Schematic drawing of the self-assembly process of TiO_2 within the block copolymer. Sol-particles are shown as small dark gray spheres, the PEO domains as dark gray chains and the PI phase is represented as light gray chains. The TiO_2 sol particles are shown to predominantly reside within the PEO phase. Different morphologies are obtained, depending on the titania load: (b) TiO_2 rich cylinders in an organic matrix for titania 1:3, (c) organic micelles in the TiO_2 rich matrix for titania 1:1 and (d) organic cylinders in a TiO_2 rich matrix for titania 3:1. (e) to (g) are bright field TEM images of the materials for the different recipes before calcination, i.e. as hybrid material. Light areas in (b)-(g) show the organic-rich domains and the dark areas correspond to the TiO_2 rich domains. (h) to (j) are TEM images of the calcined material for all three recipes (heated to 500°C in air). I acknowledge that all images presented in this figure were acquired by Stefan Guldin in Cornell University.

sample has predominantly collapsed since there is no self supporting scaffold once the polymer is removed, though elongated features with a cylinder-like morphology can still be seen. Samples with a higher inorganic ratio (titania 1:1 and 2:1) maintained their previous morphology.

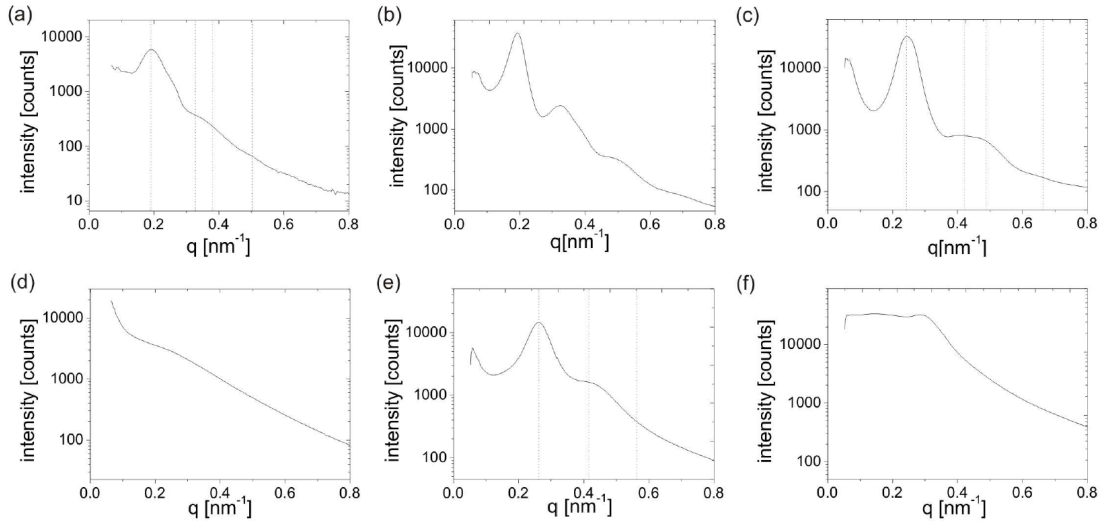

Figure 4.4: Radially-integrated plots from small angle X-ray scattering patterns. The scattering vector, q, is defined as $q = 4\pi sin\frac{\theta}{\lambda}$, where θ is the scattering angle and λ is the x-ray wavelength. Plots (a) to (c) correspond to the pre-calcined hybrid samples of titania 1:3, 1:1, and 2:1, respectively. Plots (d) to (f) correspond to the calcined samples of titania 1:3, 1:1, and 2:1, respectively. Dotted lines in (a) and (c) show predicted peak positions for hexagonal morphologies calculated from the first reflection peak positions. Dotted lines in (e) are reminiscent with a micellar arrangement of pores as described in the text for the calcined titania 1:1 sample. I acknowledge that all the data and analysis presented in this figure was acquired and performed by Hiroaki Sai in Cornell University.

Powder X-ray diffraction was employed to probe the crystal polymorph and size in the resulting films processed from pastes. Initially, after calcination of the monolith at 500°C for 2 hours, the crystal phase was entirely anatase consisting of nanocrystals with sizes of 10.1 ± 0.2 nm for the 1:3 ratio, 11.2 ± 0.1 nm for the 1:1 ratio and 12.7 ± 0.1 nm for the 2:1 ratio as determined by Debye-Scherrer analysis.

While the size of the nanocrystals varied for the three recipes after the first calcination step, a less significant trend is discernible upon re-sintering the paste,

and similar final sizes are reached for all three initial compositions. The SEM images in Figure 4.5, (d) to (f) depict the final mesoscopic film morphology of all the ratios and it is evident that all morphologies are similar after grinding, sonification, paste formation and subsequent annealing. Additionally, the Brunauer-Emmett-Teller (BET) specific surface area obtained from nitrogen physisorption of the film processed materials are very similar for the three initial TiO_2 to polymer ratios, $\sim$60 m^2g^{-1} (data not shown), while any added porosity during paste processing of the films was kept constant by the addition of ethyl-cellulose in a 1:2 (cellulose:TiO_2) ratio by weight.

It is important to emphasize that the initial block copolymer-derived morphologies of Figure 4.3 are predominantly lost during the grinding process utilized for device manufacture: The titania layers in the three device cross-sections, shown in Figure 4.5, are indistinguishable in terms of porosity, TiO_2 morphology and crystallinity. Although this limits the control of the mesostructure in these "processable" films, the three types of titania have a different preparation history. This provides an excellent framework to study the electronic properties of mesoporous materials that were synthesized from different (but controlled) initial conditions, while keeping factors such as surface area, crystal size, dye uptake, light scattering, and hole transporter infiltration relatively constant.

4.3.2 Solar cell performance

Solid-state dye-sensitized solar cells were fabricated as described in section 3.1 using the D102 dye. After filling the pores, the hole transporter has to create a thin and uniform capping layer on top of the electrode to introduce the necessary electronic asymmetry of the device, establishing a selective contact of the organic hole conductor with the metal electrode. On the other hand, a thick capping layer increases the series resistance in the device and limits the fill factor.[13] The herein created films were extremely rough, and, following the standard coating protocol (15 wt% spiro-OMeTAD in chlorobenzene spin-coated at 2000 rpm)[26] only relatively poor device performances were obtained.

The degree of pore filling and the thickness of the capping layers are important factors influencing the device performance. This requires a careful investigation

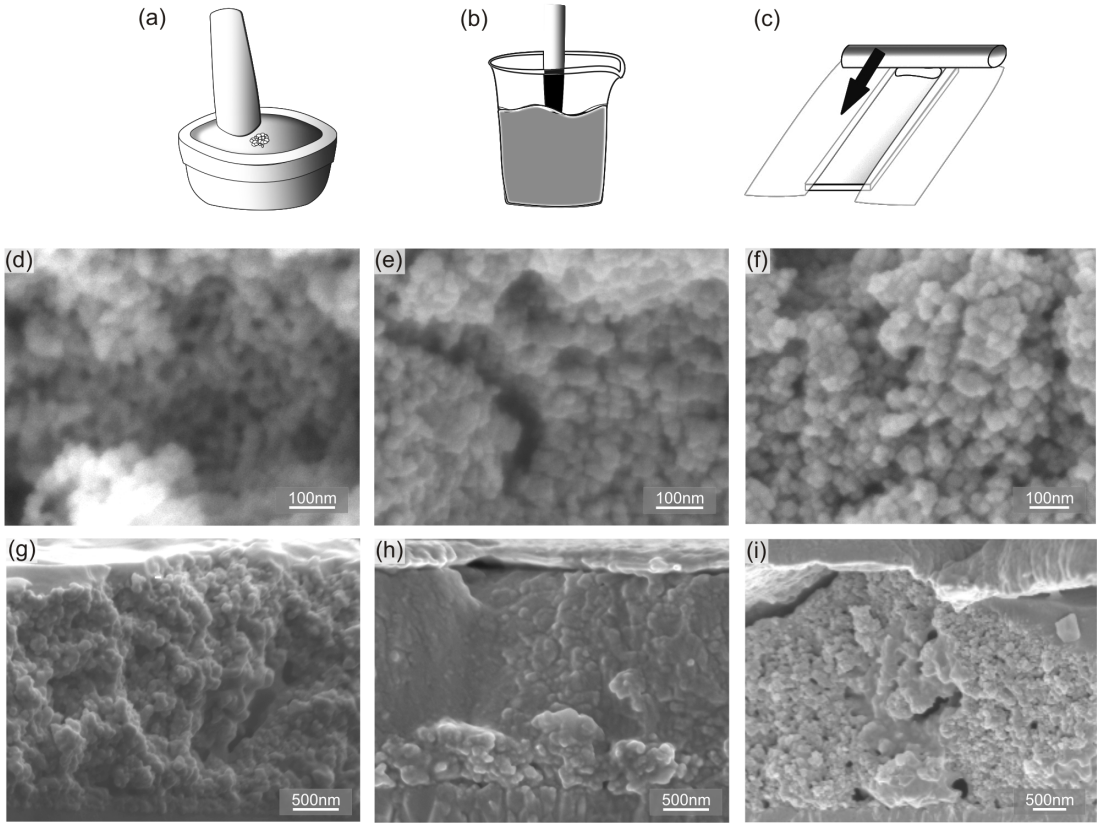

Figure 4.5: SEM images of the TiO_2 paste. (a) to (c) show the different steps in the paste reconstitution process. First the annealed powder is lightly ground for 2 minutes (a), then cellulose and α-terpineol are added and the resulting mixture is sonicated (b), and finally the paste is doctor bladed to obtain thin films of around 2 μm in thickness (c). (d) to (f) are SEM surface images of the ensuing mesoporous TiO_2 after sintering the paste on the device substrates, (f) corresponds to titania 2:1, (e) to titania 1:1 and (d) to titania 1:3. (g) to (i) are the corresponding SEM images of device cross-sections. I acknowledge that all the images presented in this figure were acquired by Stefan Guldin in the University of Cambridge.

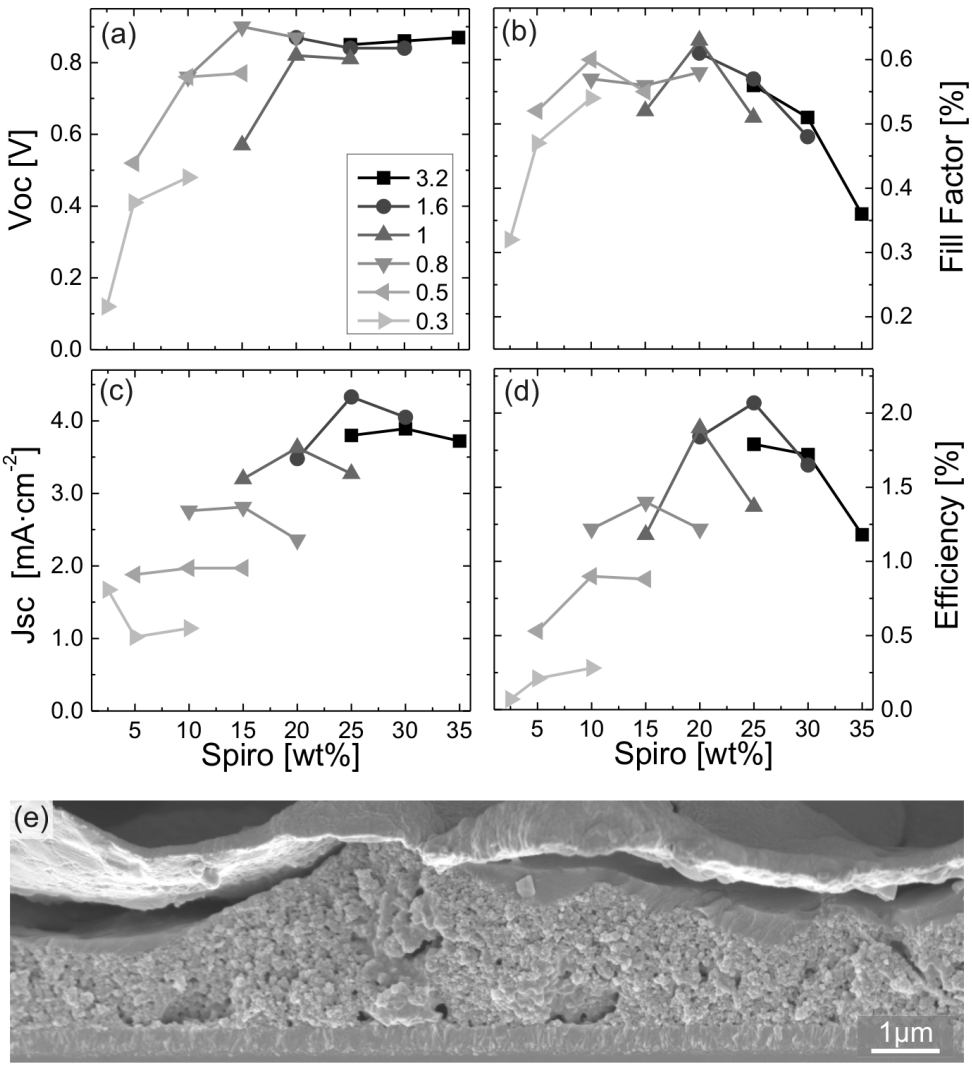

Figure 4.6: Pore filling optimization. Graphs a to d show the solar cell performance parameters measured under full sun illumination for the titania 2:1 devices, where the numbers in the legend correspond to the film thicknesses in μm. Each data point is the result of the average from 3 to 6 devices. (a) Open-circuit voltage, (b) fill factor, (c) short circuit current and (d) power conversion efficiency. Error bars are omitted for clarity, but they are between 5-10% of the values shown. (e) A long cross-section of the optimized titania 1:3 device where the thickness varies between 1 and 3 μm.

of the spiro-OMeTAD processing step that can be finely tuned by varying the concentration of the casting solution and the spin-coating speed.[26, 27] The thickness of the mesoporous layer was varied as well as the concentration of the spiro-OMeTAD casting solution. In Figure 4.6a-d the solar cell performance parameters are shown for devices incorporating titania 2:1 paste electrodes of a range of different thicknesses. The performance parameters are plotted against spiro-OMeTAD concentration in the starting solution, measured under 100 mWcm^{-2} AM 1.5 simulated sun light. The basic observation is that devices between 1 to 3 microns in thickness operate reasonably well with casting solutions containing between 20 to 30% spiro-OMeTAD (c.f. 15% for standard devices, i.e. fabricated from commercially available nanoparticle pastes). The evolution of the solar cell performance parameters with spiro-OMeTAD concentration is a convolution of the increasing film thickness, pore filling and capping layer thickness.[26, 27] For the thin films (up to 0.5 μm), the layer roughness is comparable to the overall film thickness, making it challenging to form an optimum composite. Figure 4.6a shows the fill factor as a function of spiro-OMeTAD concentration, with the film thicknesses noted in the legend. At low spiro-OMeTAD concentrations the pore filling improves with increasing concentration resulting in an increase in fill factor. The solubility limit for spiro-OMeTAD in chlorobenzene is close to 35 % and hence the use of high concentration solutions does not improve pore filling, but increases the thickness of the capping layer causing a lower fill factor. Too thick capping layers appear to limit the device performance by increased resistive losses, though pore filling may also be inhibited by excessive concentrations of the casting solution. The optimum combination of parameters is a TiO_2 film thickness of 1.6 μm and a spiro-OMeTAD solution concentration of 25%. This is a considerably higher concentration than the optimised concentration of 15% required for devices manufactured from smooth films made with standard TiO_2 nanoparticles. This is probably due to the requirement of having a considerably thicker spiro-OMeTAD capping layer to completely cover the rough undulating film.

To illustrate the roughness of the layers and the apparent difficulty of uniformly filling and capping these “undulating” films, a cross sectional SEM image of a solid-state DSC incorporating a titania 1:3 film is shown in Figure 4.6e.

Even though this is one of the roughest devices of the series, the device delivered a power conversion efficiency of over 3%. In contrast to previous assumptions, this clearly demonstrates that the solid-state DSC is compatible with rough non-uniform films. Upon close inspection of the SEM image, it is apparent that both the spiro-OMeTAD capping layer (darker region near the top), and the silver electrode (bright capping material) are to a greater or lesser degree conforming to the undulating surface. This is a likely explanation for the good fill factor of these devices. A similar study of film thickness and pore filling as shown for titania 2:1 in Figure 4.6 was conducted for the remaining two titania ratios, and the best performing cells from each series are characterized electronically in more depth below. The roughness of the films is a consequence of the employed fabrication pathway to mesoporous TiO_2 films. In an earlier publication it was shown that in the presented fabrication approach the basic constituents, titania nanocrystallites, typically agglomerate into building blocks on the micrometer length scale, which has the fortunate effect of uniting scattering and a high surface area for dye loading and ensuing light harvesting in a single, thin layer.[21]

Figure 4.7-a shows the normalized photovoltaic action spectra for the optimized devices based on pastes made with all three titania recipes as well as the normalized incident photon-to-electron conversion efficiency (IPCE) for a device fabricated from standard TiO_2 nanoparticle paste for comparison (the curves have been normalized for shape comparison), all cells are sensitized with the same dye, D102. As mentioned previously, the mesoporous material fabricated from all three titania recipes have similar surface areas, and judging by the normalized IPCE spectra, they have similar light absorption profiles. As compared to the reference standard nanoparticle based device, the block copolymer spectra are narrower, suggesting a slightly lower absorption depth in the block copolymer derived composites. A study of the variation of photovoltaic action spectra with the cell thickness was also performed and is shown in Figure 4.8. The width of the action spectra increases monotonically with increasing film thickness. The "standard nanoparticle" based cells were fabricated from Dyesol 18NR-T paste which is composed of ∼20nm diameter 100% anatase nanoparticles, with a post $TiCl_4$ treated film porosity of approximately 58%, a surface area of 62 m^2g^{-1} and a pore size of 23nm as determined by nitrogen adsorption mesurments.

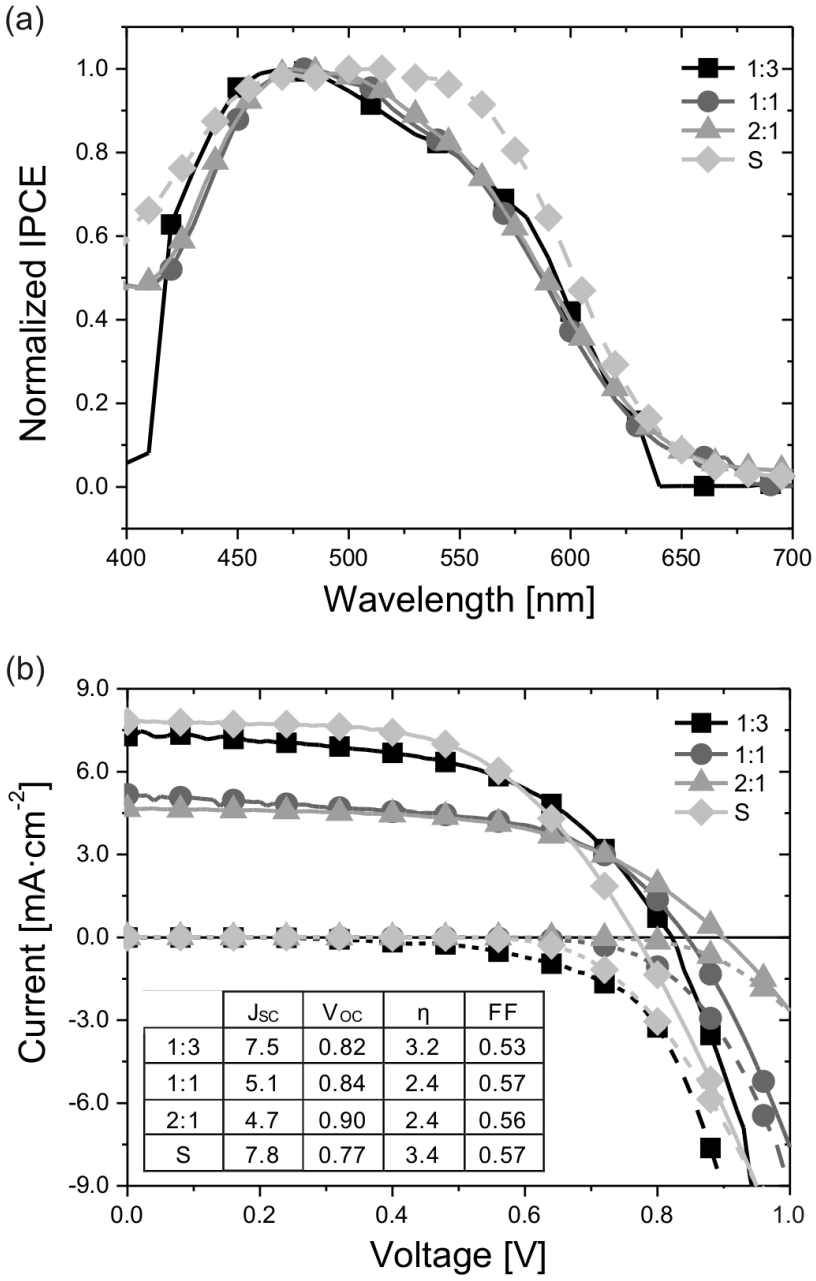

	J_{SC}	V_{OC}	η	FF
1:3	7.5	0.82	3.2	0.53
1:1	5.1	0.84	2.4	0.57
2:1	4.7	0.90	2.4	0.56
S	7.8	0.77	3.4	0.57

Figure 4.7: a) Normalized incident photon-to-current conversion efficiency (IPCE) and b) current density-voltage (JV) curves of devices made from the 3 titania recipes (see legend). A reference device fabricated from a standard nanoparticle paste is shown as gray diamonds (S in the legend). Inset in b) shows the extracted values for the short-circuit current (J_{sc}), open-circuit voltage (V_{oc}), power conversion efficiency (η) and fill factor (FF) for the 4 devices.

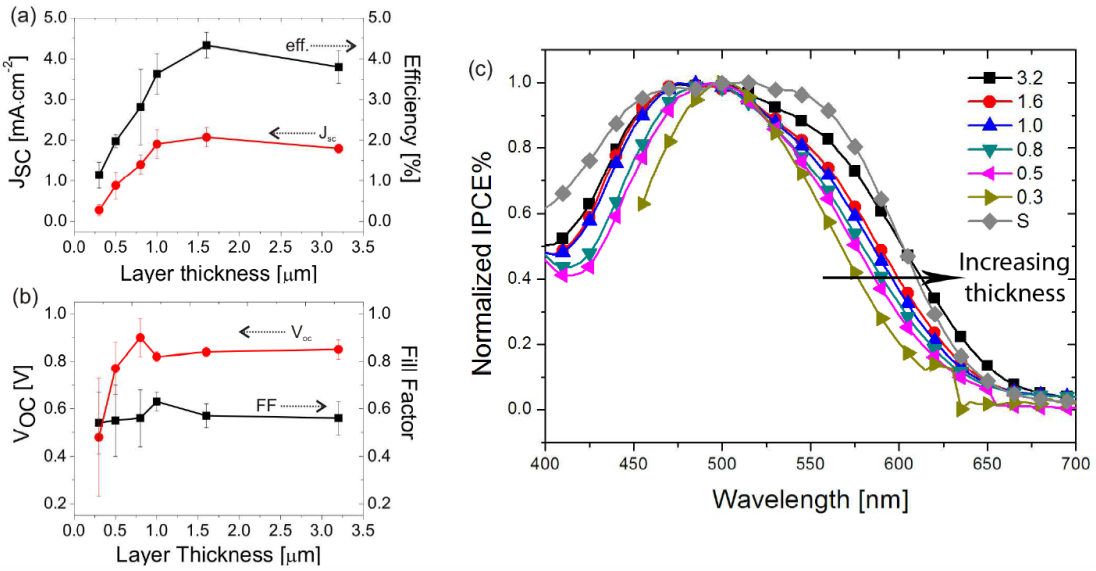

Figure 4.8: Thickness dependence of devices incorporating the titania 2:1 morphology, parameters extracted from measurements of solid-state DSC with optimized hole transporter concentrations. a-b) Solar simulator parameters, where in a) efficiency (●) and short-circuit current (J_{sc}, ■), and in b) open-circuit voltage (V_{oc}, ■) and fill factor (●), are all plotted against mesoporous layer thickness. Values shown are the average of 3 to 6 devices. c) Normalized incident photon-to-electron conversion efficiencies (IPCE) for the different mesoporous layer thicknesses plotted against wavelength. A "standard" (S) nanoparticle device (◆) is shown for comparison

In Figure 4.7b the current voltage (JV) curves for the best performing devices of each paste recipe are shown, along with a standard nanoparticle based reference cell fabricated in the same series. The short-circuit current and overall performance improve with reduction of the titania content in the recipe. The titania 1:3 device generated a very competitive short-circuit current of 7.5 $mAcm^{-2}$ and an overall efficiency of 3.2% measured under simulated AM1.5 sun light at $100mWcm^{-2}$. This is a 100% improvement upon the previous best reported block copolymer assembled solid-state DSC[10] where the assembly and crystalisation took place directly upon the FTO glass substrate. It is also extremely close to the standard nanoparticle based device,[28] which in this case delivered 3.4 % power conversion efficiency.

4.3.3 Electronic properties

The primary reason for varying the composition of the metal-oxide precursor sol over a broad range was to systematically change the material structure and properties in order to improve our understanding of the critical factors which limit and improve device performance. TiO_2 synthesis via copolymer-directed self-assembly is a very different route compared to the traditional colloidal assembly, and hence broadens the scope for optimizing TiO_2 properties for DSCs, and furthermore opens up the parameter space available for detailed investigation. In order to investigate differences in electronic behavior between the various devices fabricated in this study, small perturbation transient photovoltage and photocurrent decay and collection measurements were performed, see section 2.4 for details. These experiments allow the derivation of the transport and recombination properties in the solar cells as well as the nature and distribution of sub bandgap states within the titania films.

The diffusion coefficient (D_e) is estimated from the current collection lifetime (τ_{trans}) as $D_e = \frac{thickness^2}{2.35\tau_{trans}}$ (see section 2.4 for more details).[29] In Figure 4.9a the diffusion coefficient versus incident light intensity is presented for devices incorporating the three titania compositions compared to a standard nanoparticle based solar cell. The diffusion coefficients increase weakly with light intensity, and are similar for all four devices, signifying similarly good charge transport in

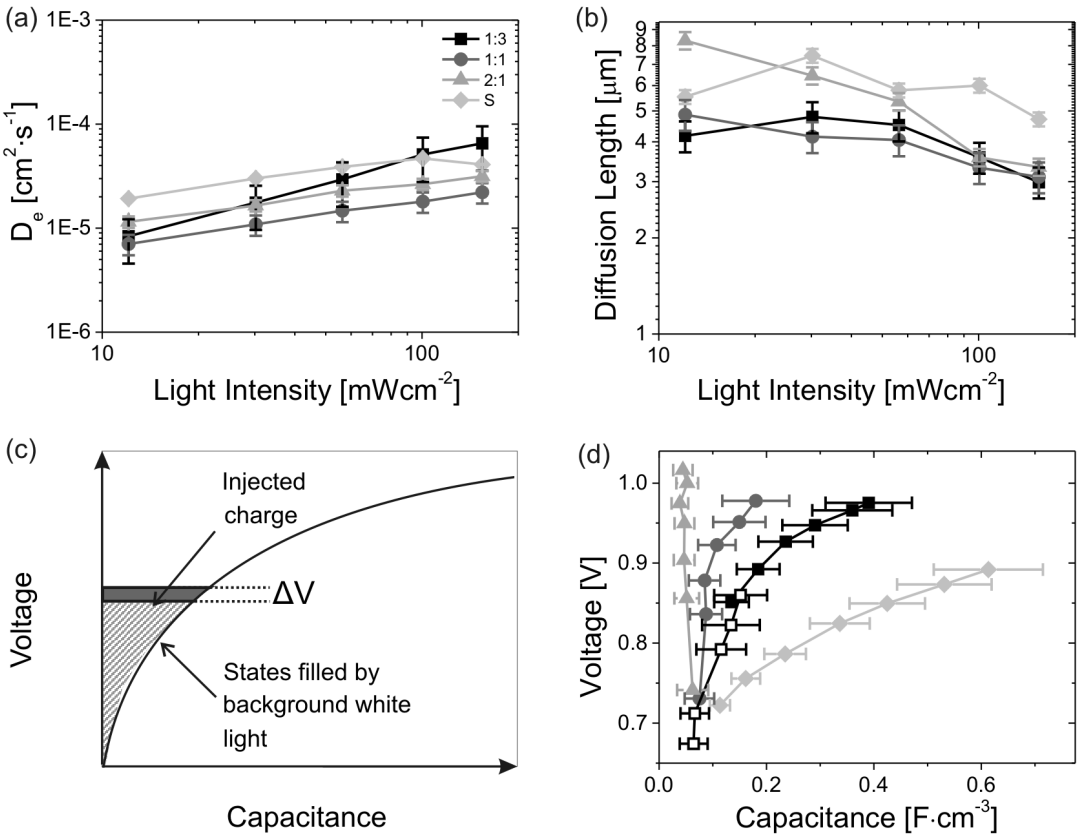

Figure 4.9: Transient photocurrent and photovoltage decay measurements. a) Diffusion coefficients (D_e) and b) diffusion lengths (L_D) extracted from transient photocurrent and photovoltage decay measurements plotted against different background white light intensities for the different titania recipes (see legend). A device made from standard (S) nanoparticle paste (diamonds) is also shown for comparison. c) Schematic diagram of the sub bandgap density-of-states, plotted as voltage against capacitance. This shows persistently filled states (shaded gray in diagonal stripes), which are populated by photo induced electron transfer from the background white light. Also shown in solid-red are states transiently filled from the red light pulse, which induce a small voltage perturbation. d) Data showing open-circuit voltage versus capacitance (calculated as $C = \frac{\Delta Q}{\Delta V}$ (injected charge/voltage perturbation)) where for titania 1:3, two cells of different thickness, 2 μm (open center), and 0.8 μm (solid center) are shown. Error bars in panels (a) and (b) are a result of the measurement errors and are dominated by the roughness of the films. Error bars in panel (d) are set at 10% of the value shown since multiple measurements on a single device yield this degree of variation. The data shown in this figure is from measurements on the same devices for which the current voltage curves in Figure 4.7b are presented.

all compositions. For the solar cell to operate efficiently charges must be collected much faster than they recombine within the active layer. To estimate how far the charges travel at short-circuit before recombining, the charge lifetime (τ_e) was estimated in this regime by performing constant current transient photovoltage decay measurements at short-circuit. The electron diffusion length (L_D) can then be calculated as $L_D = \sqrt{D_e \tau_e}$. For the block copolymer derived devices the diffusion length drops slightly with increasing illumination intensity, and at the equivalent to full sun light intensity it is almost identical for the three titania recipes at about 3.5 μm. The diffusion lengths are lower at full sun intensity as compared to the standard nanoparticle based devices, but the current collection efficiency (η_{col}) at 100 mWcm^{-2} was estimated to be very similar for all devices at 94% for the titania 1:3, 97% for the titania 1:1, and 92% for the titania 2:1, as compared to 96% for the standard cell. Since current collection efficiencies are close to unity for all optimised devices, the variations observed in photovoltaic performance must stem from another process than from inefficient charge collection.

For further investigation, current collection and voltage perturbation measurements to probe the location and density of the sub bandgap states were used. See section 2.4 for details. A schematic of the density-of-states (DOS) is shown in Figure 4.9c. Figure 4.9d shows the sub bandgap density-of-states distribution, or chemical capacitance, extracted from these measurements. A clear and significant trend between the titania synthesized in the three different ways was observed. As the titania content is reduced, a deepening and a broadening of the DOS is observed. This systematic trend suggests that the crystallization environment strongly affects the electronic material properties of the copolymer directed titania. Titania films stemming from a network in which the inorganic component represents the majority phase (i.e. titania 2:1) lead to devices with fewer sub bandgap states, or to sub bandgap states that lie at higher energies. The more open monolith structures (titania 1:3, titania 1:1) lead to a deepening and broadening of the DOS distribution, which is most distinct when the crystallizing inorganic component represents the minority phase for titania 1:3. In comparison to the diblock copolymer directed devices, the standard nanoparticle based cell has an even deeper and broader DOS distribution. All mesoporous

films were subject to a surface treatment with $TiCl_4$ prior to re-sintering, which grows a thin shell of titania upon the surface. This suggests that the changes to the density-of-states observed are not due to states residing directly upon the surface of the mesoporous material, due to the presence of the $TiCl_4$ grown titania shell. Nor are they due to a change in the interaction between the titania and the spiro-OMeTAD phases.

The fine-tuning of the DOS distribution can be attributed to the existence of the surrounding reducing organic component, which may be acting as an oxygen sink during calcination. The density of sub bandgap states in Figure 4.9d is most likely due to oxygen vacancies which increase with increasing the volume fraction of the polymer surrounding the amorphous titania during calcination. It is therefore intriguing to further study the interplay of sample composition with annealing temperatures and atmosphere, to achieve full control over the sub bandgap DOS. Carbon contamination of the TiO_2 by the organic components is an unlikely explanation for the observed results given the increased efficiency of the devices with higher organic to inorganic ratio. Studies by Lee *et al.* have shown that the carbon content of the initially hybrid material is lost during the calcination process in an oxygen rich environment.[9]

To correlate device performance with the sub bandgap DOS, a clear trend of increasing photocurrent and reducing open-circuit voltage with increasing the depth and width of the DOS can be observed. The open-circuit voltage is generated by the offset of the quasi-Fermi level for electrons in the TiO_2 with the quasi-Fermi level for holes in the spiro-OMeTAD (or hole polaron level). The shallower and narrower the DOS distribution, the lower (closer to vacuum) the quasi-Fermi level for electrons will be for any given photogenerated charge density. This is in line with the findings of increasing open circuit voltage from 0.77 V for the standard nanoparticle based cell over 0.82 V for titania 1:3 up to 0.90 V for titania 2:1, shown in Figure 4.7b. The increasing photocurrent with increasing the depth of the density of sub bandgap states cannot be explained by considering transport and recombination, since these are remarkably unaffected by the titania synthesis. However, if photoinduced electron transfer from the dye to the titania is strongly influenced by the position and density of the sub bandgap states,[30] then the observed trend of increasing photocurrent with increasing depth of the

DOS distribution is justifiable. If electron transfer from the photoexcited dye into the TiO_2 is a tunneling process, then increasing the density-of-states into which the electron can be transferred would be expected to increase the rate and efficiency of electron transfer and charge generation. Since increased photocurrent is observed as the density of sub bandgap states in the mesoporous titania is increased, this implies that a large fraction of the electrons are not injected into the conduction band, but directly into the sub bandgap states. Koops *et al.* made a similar observation for the electron transfer from a ruthenium complex dye termed N719 into TiO_2 and conclude that intersystem crossing from the singlet to the triplet state competes with ultra-fast electron transfer into the TiO_2.[30] Due to the lower energy of the triplet state in the N719 dye, electron injection from this state has to proceed via the sub bandgap states and is hence dependent upon the position and density of such states. Since an all organic dye is used in this study, intersystem crossing is unlikely to be fast. However, dye aggregation has also been observed to slow down electron transfer,[31] and the indoline based organic dyes used here are prone to aggregation,[32] and specifically for D102 J-aggregates are known to form which result in a significant deepening of the dye LUMO level. Furthermore, if dye aggregation occurs then the excited state may delocalize over one or more dye molecules, significantly reducing both the excited state energy of the electron and the "push-pull" orientation of the excited state, and hence increase the requirement for a large density of sub bandgap states into which electron transfer can occur.

The intriguing result here is that by controlling the mesoscale morphology of the TiO_2 by diblock copolymer assisted self-assembly, it is possible to systematically vary the distribution of electronic sub bandgap states in the material. This work highlights the criticality of the energetic location and distribution of sub bandgap states, and their role in efficient photocurrent generation in solid-state DSCs.

4.4 Conclusions

In summary, mesoporous TiO_2 was synthesized in different crystallization environments through the use of the diblock copolymer PI-*b*-PEO. The influence of

the crystallization environment on the electronic properties of the materials and performance characteristics of solid-state DSCs incorporating the mesoporous TiO_2 was investigated. It was found that the density and distribution of sub bandgap states is a function of the synthesis conditions and critically affects the performance characteristics of self-assembled titania in hybrid solar cells. This allows a new degree of freedom to vary and optimize towards the goal of controlling functional electronic hybrid interfaces. Specifically here, as the width and depth of the density of sub bandgap states is increased, a significant enhancement in the photocurrent generation is observed. It is postulated that this is due to the requirement for an abundance of sub bandgap states into which efficient electron transfer can occur from the photoexcited sensitizers. Higher photocurrent generation is accompanied by an overall drop in open-circuit voltage with increasing density of sub bandgap states, reflected in a trade-off in terms of the overall power conversion efficiency. These findings do not necessarily imply that a high density of sub bandgap states are required in an ideal DSC, but rather serious losses in the charge generation mechanism take place. Reducing the heterogeneity and increasing the efficiency of this electron transfer and charge separation process are likely to be central goals for dramatic efficiency improvements in solid-state DSCs.

References

[1] Cheolmin Park, Jongseung Yoon, and Edwin L. Thomas. Enabling nanotechnology with self assembled block copolymer patterns. *Polymer*, 44(22):6725 – 6760, 2003. 44

[2] Paul J. Flory. Thermodynamics of high polymer solutions. *The Journal of Chemical Physics*, 10(1):51–61, 1942. 44

[3] Edward J. W. Crossland, Marleen Kamperman, Mihaela Nedelcu, Caterina Ducati, Ulrich Wiesner, Detlef M. Smilgies, Gilman E. S. Toombes, Marc A. Hillmyer, Sabine Ludwigs, Ullrich Steiner, and Henry J. Snaith. A bicontinuous double gyroid hybrid solar cell. *Nano Lett.*, 9(8):2807–2812, 2008. 45, 47

[4] Edward J. W. Crossland, Mihaela Nedelcu, Caterina Ducati, Sabine Ludwigs, Marc A. Hillmyer, Ullrich Steiner, and Henry J. Snaith. Block copolymer morphologies in dye-sensitized solar cells: Probing the photovoltaic structure-function relation. *Nano Lett.*, 9(8):2813–2819, 2009. 45, 47

[5] Markus Templin, Achim Franck, Alexander DuChesne, Heike Leist, Yuanming Zhang, Ralph Ulrich, Volker Schadler, and Ulrich Wiesner. Organically modified aluminosilicate mesostructures from block copolymer phases. *Science*, 278(5344):1795–1798, 1997. 45

[6] P. D. Yang, D. Y. Zhao, D. I. Margolese, B. F. Chmelka, and G. D. Stucky. Generalized syntheses of large-pore mesoporous metal oxides with semicrystalline frameworks. *Nature*, 396(6707):152–155, 1998. 45

[7] K.M Coakley, Y. Liu, M.D. McGehee, K.L. Frindell, and G.D. Stucky. Infiltrating semiconducting polymers into self-assembled mesoporous titania films for photovoltaic applications. *Advanced Functional Materials*, 13(4):301–306, 2003. 45

[8] D. Fattakhova-Rohlfing, M. Wark, T. Brezesinski, B. M. Smarsly, and J. Rathousky. Highly organized mesoporous TiO_2 films with controlled crystallinity: A li-insertion study. *Adv. Funct. Mater.*, 17(1):123–132, 2007. 45

[9] J. Lee, M. C. Orilall, S. C. Warren, M. Kamperman, F. J. Disalvo, and U. Wiesner. Direct access to thermally stable and highly crystalline mesoporous transition-metal oxides with uniform pores. *Nature Materials*, 7(3):222–228, 2008. 45, 46, 61

[10] Mihaela Nedelcu, Jinwoo Lee, Edward J. W. Crossland, Scott C. Warren, M. Christopher Orilall, Stefan Guldin, Sven Huttner, Catarina Ducati, Dominik Eder, Ulrich Wiesner, Ullrich Steiner, and Henry J. Snaith. Block copolymer directed synthesis of mesoporous TiO_2 for dye-sensitized solar cells. *Soft Matter*, 5(1):134, 2009. 45, 46, 47, 58

[11] P.F.W. Simon, R Ulrich, HW Spiess, and U Wiesner. Block copolymer-ceramic hybrid materials from organically modified ceramic precursors. *Chem. Mater.*, 13(10):3464–3486, 2001. 45

[12] J Kruger, R Plass, Michael Gratzel, PJ Cameron, and LM Peter. Charge transport and back reaction in solid-state dye-sensitized solar cells: A study using intensity-modulated photovoltage and photocurrent spectroscopy. *J. Phys. Chem. B*, 107(31):7536–7539, 2003. 45

[13] Francisco Fabregat-Santiago, Juan Bisquert, Le Cevey, Peter Chen, Mingkui Wang, Shaik M. Zakeeruddin, and Michael Gratzel. Electron transport and recombination in solid-state dye solar cell with spiro-ometad as hole conductor. *J. Am. Chem. Soc.*, 131(2):558–562, 2009. 45, 51

[14] T. Dittrich, E.A. Lebedev, and J. Weidmann. Electron drift mobility in porous tio$_2$ (anatase). *Phys. Status Solidi A*, 1998(165):R5–R6, 1998. 45

[15] Henry J Snaith and Michael Gratzel. Electron and hole transport through mesoporous TiO_2 infiltrated with spiro-ometad. *Adv. Mater.*, 19:3643–3647, 2007. 45

[16] Priti Tiwana, Patrick Parkinson, Michael B. Johnston, Henry J. Snaith, and Laura M. Herz. Ultrafast terahertz conductivity dynamics in mesoporous TiO_2 : Influence of dye sensitization and surface treatment in solid-state dye-sensitized solar cells. *J. Phys. Chem. C*, 114(2):1365–1371, 2010. 45

[17] Stefan Guldin, Sven Huttner, Priti Tiwana, M. Christopher Orilall, Burak Ulgut, Morgan Stefik, Pablo Docampo, Matthias Kolle, Giorgio Divitini, Caterina Ducati, Simon A. T. Redfern, Henry J. Snaith, Ulrich Wiesner, Dominik Eder, and Ullrich Steiner. Improved conductivity in dye-sensitised solar cells through block-copolymer confined TiO_2 crystallisation. *Energy Environ. Sci.*, 4(1):225–233, 2011. 46

[18] Pablo Docampo, Stefan Guldin, Morgan Stefik, Priti Tiwana, M. Christopher Orilall, Sven Huttner, Hiroaki Sai, Ulrich Wiesner, Ulrich Steiner, and Henry J. Snaith. Control of solid-state dye-sensitized solar cell performance by block-copolymer-directed TiO_2 synthesis. *Adv. Funct. Mater.*, 20(11):1787 – 1796, 2010. 46

[19] Stefan Guldin, Sven Huttner, Priti Tiwana, M. Christopher Orilall, Burak Ulgut, Morgan Stefik, Pablo Docampo, Matthias Kolle, Giorgio Divitini,

Caterina Ducati, Simon A. T. Redfern, Henry J. Snaith, Ulrich Wiesner, Dominik Eder, and Ullrich Steiner. Improved conductivity in dye-sensitised solar cells through block-copolymer confined TiO_2 crystallisation. *Energy Environ. Sci.*, 4(1):225–233, 2011. 46

[20] SA Bagshaw, E Prouzet, and TJ Pinnavaia. Templating of mesoporous molecular-sieves by nonionic polyethylene oxide surfactants. *Science*, 269(5228):1242–1244, 1995. 47

[21] Mihaela Nedelcu, Stefan Guldin, M. Christopher Orilall, Jinwoo Lee, Sven Huttner, Edward J. W. Crossland, Scott C. Warren, Caterina Ducati, Pete R. Laity, Dominik Eder, Ulrich Wiesner, Ullrich Steiner, and Henry J. Snaith. Monolithic route to efficient dye-sensitized solar cells employing diblock copolymers for mesoporous TiO_2. *J. Mater. Chem.*, 20:1261–1268, 2010. 47, 55

[22] S. Ito, P. Chen, P. Comte, M. K. Nazeeruddin, P. Liska, P. Pechy, and M. Gratzel. Fabrication of screen-printing pastes from TiO_2 powders for dye-sensitised solar cells. *Progress in photovoltaics*, 15(7):603–612, 2007. 48

[23] EL Crepaldi, GJDA Soler-Illia, D Grosso, F Cagnol, F Ribot, and C Sanchez. Controlled formation of highly organized mesoporous titania thin films: From mesostructured hybrids to mesoporous nanoanatase TiO_2. *J. Am. Chem. Soc.*, 125(32):9770–9786, 2003. 48

[24] Benjamin C. Garcia, Marleen Kamperman, Ralph Ulrich, Anurag Jain, Sol M. Gruner, and Ulrich Wiesner. Morphology diagram of a diblock copolymer-aluminosilicate nanoparticle system. *Chemistry of Materials*, 21(22):5397–5405, 2009. 48

[25] Haiying Huang, Zhijun Hu, Yongzhong Chen, Fajun Zhang, Yumei Gong, Tianbai He, and Chi Wu. Effects of casting solvents on the formation of inverted phase in block copolymer thin films. *Macromolecules*, 37(17):6523–6530, 2004. 48

[26] Henry J. Snaith, Robin Humphry-Baker, Peter Chen, Ilkay Cesar, Shaik M. Zakeeruddin, and Michael Gratzel. Charge collection and pore filling in solid-state dye-sensitized solar cells. *Nanotechnology*, 19(42), 2008. 51, 54

[27] I. K. Ding, N. Tetreault, J. Brillet, B. E. Hardin, E. H. Smith, S. J. Rosenthal, F. Sauvage, M. Gratzel, and M. D. McGehee. Pore-filling of spiro-ometad in solid-state dye sensitized solar cells: Quantification, mechanism, and consequences for device performance. *Adv. Func. Matter.*, 19(15):2431–2436, 2009. 54

[28] L. Schmidt-Mende, U. Bach, R. Humphry-Baker, T. Horiuchi, H. Miura, S. Ito, S. Uchida, and M. Gratzel. Organic dye for highly efficient solid-state dye-sensitized solar cells. *Adv. Matter.*, 17(7):813–815, 2005. 58

[29] J. van de Lagemaat and A. J. Frank. Nonthermalized electron transport in dye-sensitized nanocrystalline TiO_2 films: Transient photocurrent and random-walk modeling studies. *The Journal of Physical Chemistry B*, 105(45):11194–11205, 2001. 58

[30] S. Koops, B. O'Regan, P. R. F. Barnes, and J. R. Durrant. Parameters influencing the efficiency of electron injection in dye-sensitized solar cells. *J. Am. Chem. Soc*, 131(13):4808–4818, 2009. 61, 62

[31] B. Wenger, M. Gratzel, and J. E. Moser. Rationale for kinetic heterogeneity of ultrafast light-induced electron transfer from ru(ii) complex sensitizers to nanocrystalline TiO_2. *J. Am. Chem. Soc*, 127(35):12150–12151, 2005. 0002-7863. 62

[32] Henry J. Snaith, Annamaria Petrozza, Seigo Ito, Hidetoshi Miura, and Michael Gratzel. Charge generation and photovoltaic operation of solid-state dye-sensitized solar cells incorporating a high extinction coefficient indolene-based sensitizer. *Advanced Functional Materials*, 19(11):1810–1818, 2009. 62

Chapter 5

Triblock terpolymer assembled structures

5.1 Introduction

Despite their potential, DSCs incorporating self-assembled networks have still not reached the best efficiencies of nanoparticle based films. A major difficulty is associated with the large volume contraction of the block copolymer derived films during processing - evaporation of residual solvent, condensation of the inorganic network and in the later stage calcination of the polymer and crystallization. For films exceeding several hundred nm in thickness, this typically leads to crack formation and delamination [1]. Several concepts have been presented where block copolymer assembled photoanodes compete well with nanoparticle films for active layers below 1 μm [2, 3], but it proves difficult to scale with thickness. However, a recent study has established a route for the deposition of mesoporous block copolymer derived films beyond 2 μm , which significantly increased the power conversion efficiency of solid-state dye-sensitized solar cells fabricated from these films to an unprecedented over 4%.[4] This efficiency, while high, was still

lower than what can be achieved through conventional photoanode design.

An observed drawback of the experimental approaches used to date is the fact that the TiO_2 is generally assembled in the majority phase. Lateral stresses during volume reduction are therefore sufficient to lead to catastrophic crack formation. A further consideration is that the ratio between organic and inorganic material in the synthesis has a strong influence on the electronic properties of the resulting TiO_2 as was observed in the previous chapter. A mainly organic matrix leads to a strongly enhanced density of sub-bandgap electronic states, correlated to a significantly increased photocurrent in the devices. For these reasons, it would be favorable to lower the TiO_2 content in the hybrid composite. However, when reducing the TiO_2 content in a diblock copolymer assembled film, as presented in the previous chapter, the metal oxide becomes a non-continuous minority phase surrounded by the polymer. Upon calcination of the oxide and thermal combustion of the copolymer, film integrity is almost entirely lost due to removal of the supporting matrix. In the previous chapter, this was worked around by performing calcination in the bulk, and subsequently incorporating the as prepared material into a paste for film processing. However, the favorable ordered structure of the mesoporous assembly is entirely lost through this process. Clearly a more direct route with a 3D continuous network morphology as-made would be preferable.

In this chapter, a new self-assembly platform is presented for the fast and straightforward synthesis of mesoporous TiO_2 films, based on the triblock terpolymer poly(isoprene-*b*-styrene-*b*-ethylene oxide) (ISO). This polymer system directs the co-assembly of the oxide into a gyroid-like morphology, where the minority phase is a 3D interconnecting strut network composed of TiO_2.

5.2 Results and discussion

5.2.1 Triblock terpolymer ISO as a structure directing agent

Recently, there have been reports on the assembly of several network morphologies, including a 3D continuous alternating (single) gyroid niobia network, which

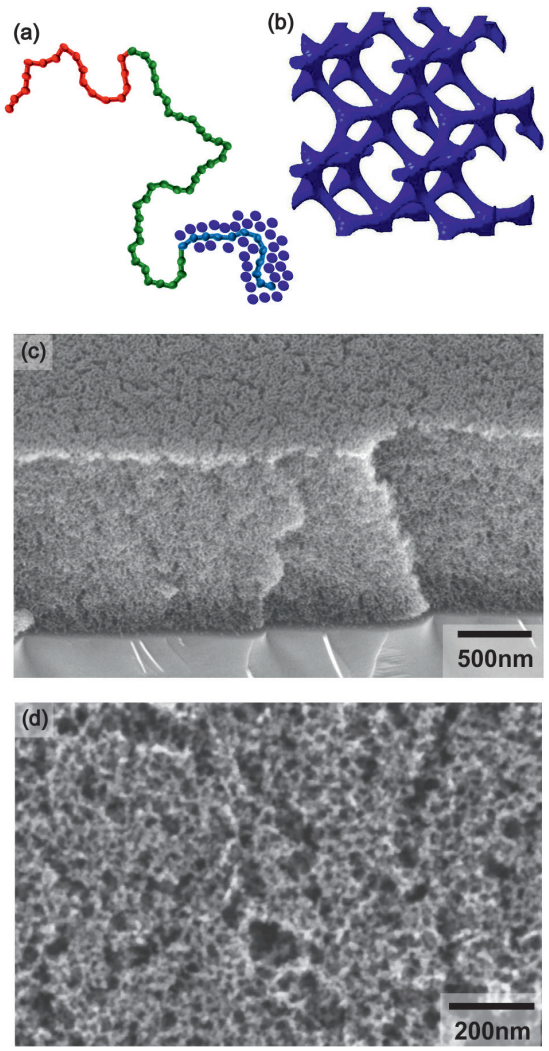

Figure 5.1: Material system and morphology.(a) The structure-directing macromolecule in this work is a triblock terpolymer poly(isoprene-*b*-styrene-*b*-ethylene oxide) with volume fractions of 31%, 53% and 16% for the isoprene (PI, red), styrene (PS, green) and ethylene oxide block (PEO, blue) respectively. The introduced sol (blue particles) are expected to preferentially reside in the hydrophilic PEO block due to attractive intermolecular forces. Under equilibrium conditions, the incompatibility of its covalently linked building blocks leads the block copolymer and its guest to assemble into its minimal energy morphology, which is in the present configuration an ordered network phase such as the alternating gyroid, where one gyroid network contains the PEO incorporating the oxide sol, and the second gyroid network contains the PI, surrounded by a PS matrix. (b) shows one such gyroid containing the PEO and the oxide phase. (c) Scanning electron microscopy image of a film deposited by doctor blade coating, shown after plasma etching to remove the polymer, which gives rise to a continuous, highly porous TiO_2 network. (d) Close-up scanning electron microscopy image of the mesostructure top surface after calcination at 500 °C exhibiting open and accessible pores. I acknowledge that all the images presented in this figure were acquired by Morgan Stefik in Cornell University.

arises from the coassembly of a triblock terpolymer poly(isoprene-*b*-styrene-*b*-ethylene oxide). In this configuration, the inorganic resides in the minority phase. Due to the fact that network phases are 3D continuous and self-supporting, the morphology is able to withstand removal of the polymer.[5] A similar system is used in this chapter. Figure 5.1a illustrates the chemical configuration: The triblock terpolymer in this work consists of a PI, PS, and PEO block with volume fractions of 31%, 53% and 16% respectively. The introduced TiO_2 sol (blue particles) are expected to preferentially reside in the hydrophilic PEO block due to attractive intermolecular forces.[6] The incompatibility of its covalently linked building blocks leads the macromolecule and its guest to co-assemble towards its energy minimal morphology [7, 8]. For the utilized volume fractions, an ordered cubic network such as a single "alternating" gyroid morphology of PEO and inorganics, surrounded by a PS matrix and a complementary gyroid network of PI, as illustrated in Figure 5.1b [5] is expected. For experimental realization, a PI-*b*-PS-*b*-PEO polymer (ISO) of M_n = 53.4kg/mol was dissolved in anisole. Separately a sol stock solution was prepared by adding titanium isopropoxide to HCl. The stock solution was then diluted and added to the polymer solution to match the aimed phase space. After deposition by doctor blade coating onto prepared FTO substrates, the films were annealed at 30 °C in an enclosed atmosphere for 24-48h, then aged at elevated temperatures for another 3 days before being calcined in air at 500°C to remove the organic structure directing agent and crystallize the inorganic network. See section 3.4.3 for more details. The as-cast films had a homogeneously networked morphology throughout the thickness as shown in Figure 5.1c. The hybrid films were based of an oxide:polymer mass ratio of 0.33:1.0, assuming complete condensation to TiO_2. This is equivalent to a volume uptake of 27.5% for the phase of PEO & TiO_2, i.e. the TiO_2 being in the minority phase. The film thickness and overall amount of TiO_2 deposited for each film was controlled with the solution concentration as well as the doctor blading height and velocity. The structural features were preserved throughout the crystallization process resulting in the generation of 20-30 nm mesopores as shown in Figure 5.1d. In contrast to earlier work using this triblock terpolymer to direct the structure assembly on more equilibrated morphologies in the bulk,[5] a specific space group cannot be identified due to the limited long-range struc-

tural ordering for thin film deposition. This is somewhat expected since drying kinetics in thin films lead to a quenching of the microphase separation process by the simultaneous sol-gel reaction before reaching its equilibrium morphology. Nevertheless, the TiO_2 photoanodes exhibit a continuous network of very high porosity which arises from the co-assembly of TiO_2 in the minority phase.

The as-calcined photoanodes were subsequently subject to a $TiCl_4$ treatment and resintering at 500°C as is conventionally done for dye-sensitized solar cells before being immersed in a dye solution and assembled into a solid-state DSC. Crystallite sizes are ∼12 nm for the triblock terpolymer-derived structures and ∼19 nm for the standard nanoparticle films via Scherrer analysis of the [101] anatase peak (see figure 3.6). The standard method to estimate the surface area and porosity of mesoporous oxides is to perform nitrogen desorption measurements. However, this proves difficult for thin films and furthermore a measure of the effective accessible surface area for dye adsorption may be more relevant for the electrode material. In order to estimate the surface roughness of the triblock terpolymer derived films we therefore compared the accessible surface area by a dye desorption technique (see section 3.2). Firstly, the standard nanoparticle based films, which have been well characterized by nitrogen desorption, were used as a standard control. From nitrogen desorption the standard nanoparticle films have a roughness factor of 116 fold per μm thickness of film. Following overnight sensitization with a ruthenium based dye, termed Z907, and subsequent dye desorption, Uv-Vis absorption measurements of the desorbed dye were taken. The dye was calculated to occupy around 1.6 nm^2 per dye molecule, consistent with reports in literature.[9, 10] With the assumption that the same dye loading will be achieved on both the anatase titania triblock terpolymer derived films and the standard anatase nanoparticles based films, we calculate the surface roughness to be 161 fold per μm thickness of film for the triblock terpolymer-derived films measured via Z907 dye desorption in methanol.

In order to estimate the porosity of the films spectroscopic ellipsometry was used to extract the optical constants for each film, and reconstructed an "effective medium" composed of differing volume fractions of air ($n \sim 1$) and anatase TiO_2 ($n = 2.5$) employing the Bruggeman effective medium approximation.[11] The refractive indices of the films were determined to be 1.39 (triblock terpolymer-

Film	Porosity (vol%)	Surface roughness (per μm)	Crystallite Size (nm)	Average pore diameter (nm)
Nanoparticle	48±4	116	19	18
Triblock	61±3	161	12	21

Table 5.1: Film characteristics. Values shown correspond to films treated with $TiCl_4$

derived films before $TiCl_4$), 1.52 (triblock terpolymer-derived films after $TiCl_4$), 1.62 (nanoparticles before $TiCl_4$), and 1.73 (nanoparticles after $TiCl_4$) respectively. It is already apparent simply from these values that the porosity reduces slightly after $TiCl_4$ treatment and that the porosity of the triblock terpolymer films is higher than the nanoparticle films. Specifically, the porosity of the triblock terpolymer-derived films was calculated to be 69±2 vol% before $TiCl_4$ treatment and 61±3 vol% after this surface treatment. In comparison, standard nanoparticle films before $TiCl_4$ treatment are calculated to be 55±2 vol% porous and 48±4 vol% after the surface treatment. The increase in refractive index after the $TiCl_4$ surface treatment corresponds to a ∼1 nm thick coating of the pore structure for both triblock terpolymer-derived films (average pore diameter ∼21 nm) and nanoparticle films (average pore diameter ∼18 nm), respectively. See ref. [12] for details. These porosity and surface area estimations indicate that structurally, the triblock terpolymer exhibits a higher accessible surface are for dye loading as well as enhanced porosity compared to the standard nanoparticle based films. A summary of all film characteristics can be found in Table 5.1.

5.2.2 Solar cell performance

Device characterization, shown in Figure 5.2 reveals the high efficiency of the presented photoanode. For comparison, the device performance of solid-state DSCs assembled from a diblock copolymer directed photoanode was included. Solar cells fabricated from the triblock terpolymer, where the cast hybrid mixture has a majority component of organic material (around 70% by volume), show a comparatively high short-circuit current (J_{sc}) of 6.7 $mAcm^{-2}$, and an open circuit voltage (V_{oc}) of 0.78 V. In the case of a diblock copolymer directed assembly, the TiO_2 resides in the majority phase, with a much higher inorganic to organic volume

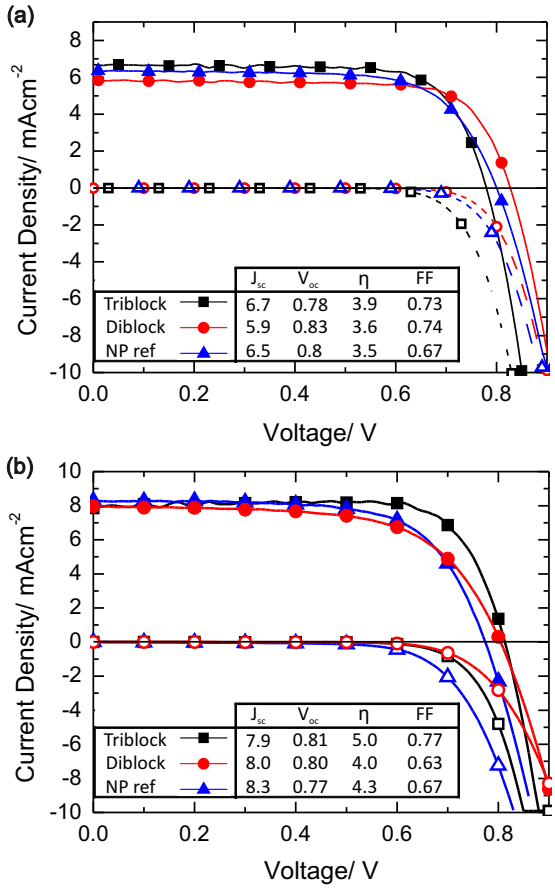

Figure 5.2: Current-voltage characteristics (a) Current-Voltage curves measured under AM1.5 simulated sun light of 100 mWcm^2 for devices incorporating triblock terpolymer co-assembled networks (■), diblock copolymer co-assembled networks (▲) and standard nanoparticle based devices (●) employing D102 as the sensitizer. Inset shows solar cell performance parameters for all 3 devices. (b) Current-Voltage curves for solid-state DSCs employing C220 as the dye-sensitizer[13].

ratio after film deposition. These photoanodes show an increased V_{oc} of 0.83 V while J_{sc} is reduced to 5.8 mAcm^{-2}. Devices based on conventional nanoparticle photoanodes lie in between, with $V_{oc} = 0.80$ V and $J_{sc} = 6.5$ mAcm^{-2}.

These findings are consistent with the observations from the previous chapter of the role of the inorganic to organic ratio in the block copolymer assembly process upon the device properties of the photoanode. The hybrid network within which the TiO_2 resides in during the calcination plays a decisive role for the electronic properties of the mesoporous TiO_2 even after the calcination step and $TiCl_4$ treatment. This has been associated to the reducing characteristic of the organics during polymer oxidation and TiO_2 crystallization at high temperatures. The organic materials may act as an oxygen sink, favoring the formation of oxygen vacancies which generate sub-bandgap states,[14, 15, 16, 17] broadening the tail of the conduction band states and subsequently aiding electron transfer from the photoexcited dye. A mainly organic matrix in the film preparation leads to a significantly increased generation of photocurrent, accompanied by a slight drop in V_{oc} in the final devices. Though photoanodes made from triblock terpolymer (highly porous continuous network), diblock copolymer (micellar arrangement) and conventional TiO_2 nanoparticles (random dense packing) are all very different, a similar strong dependence on its "organic to inorganic history" during materials assembly appears to be observed.

For devices incorporating one of the best performing dyes for solid-state DSCs, a donor-pi-acceptor organic dye termed C220,[13] a striking power conversion efficiency of 5.03% is obtained for triblock terpolymer directed photoanodes, shown in Figure 5.2b. This represents a 16% improvement in performance over standard optimized nanoparticle devices of 1.8 μm in thickness as prepared in the group's laboratory, demonstrating the potential of this approach for future high efficiency devices. As somewhat of a milestone for this materials approach, on a like-to-like comparison this is the first time the self-assembled oxides have out-performed the conventional state-of-the art nanoparticle based photoanodes in dye-sensitized solar cells. Unfortunately, the maximum current from the JV curve for the triblock devices does not occur at short-circuit. This effect is sometimes observed, though not fully understood, for some sensitizers when used in solid-state dye-sensitized solar cells,[18] however investigating its exact nature is outside of the scope of

this work.

5.2.3 Electronic properties

In the previous chapter, the effect of the film morphology was eliminated and found no significant differences in charge transport and recombination. In contrast, here over two-fold increase in charge transport rate at short-circuit for films with diblock copolymer directed structures is observed, compared to the ones assembled with the triblock terpolymer (background bias light around 100 $mWcm^{-2}$). This trend is maintained over a wide span of light intensities down to 2 $mWcm^{-2}$, which corresponds to a photocurrent of about 0.2 $mAcm^{-2}$ in these devices. This significant difference, shown in Figure 5.3a, probably arises from the larger crystal size and the denser TiO_2 network of the diblock copolymer directed structures.[19, 20] Recombination dynamics are very similar in all 3 systems, as shown in Figure 5.3b, where almost all data points overlap at similar background bias light intensities.

Along with higher electron transport rates, increased photocurrents are expected from systems with better charge collection efficiencies. In contrast, a 15% loss in photocurrent for the "highly diffusive" diblock directed films is observed compared to the triblock systems. However, the charge collection efficiency, as calculated from the balance of rates for charge collection and recombination under short-circuit conditions, is over 95% for all systems. To resolve this peculiarity, differential capacitance-voltage measurements were performed which directly gives the shape of the sub-bandgap density of states (DOS) in the TiO_2 photoanodes. Figure 5.3c clearly shows a large increase in the sub-bandgap DOS for the triblock devices compared to the diblock solar cells. This effect is consistent with the postulation from the previous chapter that the organic components partially reduce the surface of the TiO_2 during thermal degradation and calcination, with the more numerous oxygen vacancies increasing the density of sub-bandgap states. Indeed, others have reported that oxygen vacancies induce adjacent Ti^{4+} ions which generate states $\sim$1 eV below the CB.[16] This suggests that the differences in photovoltaic parameters found in the JV curves of Figure 5.2 are dominated by the underlying shift in the distribution of sub-bandgap

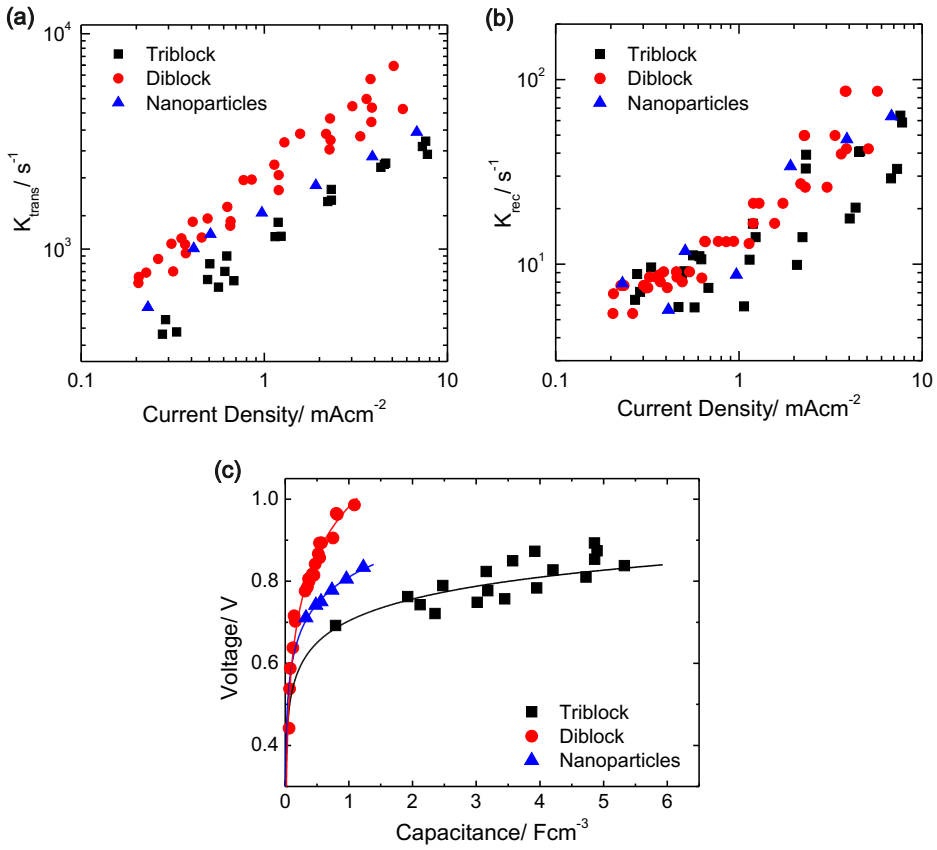

Figure 5.3: Device characteristics. Transport (a) and recombination (b) rates at short circuit conditions for devices incorporating triblock terpolymer co-assembled networks (■), diblock copolymer co-assembled networks (●) and standard nanoparticle based devices (▲). (c) Density of states plot per cm^{-3} of titania, for devices incorporating triblock terpolymer co-assembled networks (■), diblock copolymer co-assembled networks (●) and standard nanoparticle based devices (▲). Lines correspond to single exponential fits of the data points. We note that the transient photocurrent and photovoltage measurements were carried out at short-circuit under potentiostatic or galvanostatic modes respectively, with the short-circuit current set and varied by changing the white light bias.

states, rather than charge collection efficiencies, again, consistent with the previous chapter. In this instance, not only must the available sub-bandgap states lie at a low enough energy to enable efficient electron transfer, but also the energy loss must be minimized to avoid a trade-off between current and voltage and hence marginalize performance improvements. In the case of the triblock terpolymer derived structures, the sub-bandgap states are also confined in a relatively narrow energy band, allowing the maximization of the photocurrent while still maintaining minimal losses to open-circuit voltage. This results in higher power conversion efficiencies than standard nanoparticle-based devices measured under similar conditions.

Since the transport rates are around two orders of magnitude faster than recombination rates at short-circuit for all systems studied, the improved functioning of the triblock terpolymer assembled photoanodes is associated to the fact that the metal oxide/dye/hole-transporter interface can be engineered to maximize the availability of sub-bandgap states for electron-transfer, while still maintaining a low enough recombination rate and high enough open-circuit voltage.

5.3 Conclusions

A new self-assembly platform was presented for the fast and straightforward synthesis of mesoporous TiO_2 films, based on the triblock terpolymer poly(isoprene-*b*-styrene-*b*-ethylene oxide). This material route has strong advantages over the state-of-the-art photoanodes in solid-state dye-sensitized solar cells. From a purely materials basis, the terpolymer route enables the direct assembly of a continuous network of anatase TiO_2 resulting in films with extremely high porosity and internal surface area. This assembled material is superior to the standard nanoparticle based films on both dye-loading capacity (for a given thickness) and on open pore area. Electronically, the triblock terpolymer derived TiO_2 exhibits a larger density of sub-bandgap states, than the standard nanoparticle based material. This high availability of sub-bandgap states improves photoinduced electron transfer from the dye-sensitizers. As a consequence, for the first time the self-assembled mesoporous oxide system outperforms the conventional nanoparticle

based electrodes fabricated and tested under the same conditions, with power conversion efficiencies of 5% demonstrated.

References

[1] S.Y. Choi, M. Mamak, N. Coombs, N. Chopra, and G. A. Ozin. Thermally stable two-dimensional hexagonal mesoporous nanocrystalline anatase, meso-nc-TiO_2: Bulk and crack-free thin film morphologies. *Adv. Funct. Mater.*, 14(4):335–344, 2004. 68

[2] Marketa Zukalova, Arnost Zukal, Ladislav Kavan, Mohammad K Nazeeruddin, Paul Liska, and Michael Gratzel. Organized mesoporous TiO_2 films exhibiting greatly enhanced performance in dye-sensitized solar cells. *Nano Lett.*, 5(9):1789–92, 2005. 68

[3] Stefan Guldin, Sven Huttner, Priti Tiwana, M. Christopher Orilall, Burak Ulgut, Morgan Stefik, Pablo Docampo, Matthias Kolle, Giorgio Divitini, Caterina Ducati, Simon A. T. Redfern, Henry J. Snaith, Ulrich Wiesner, Dominik Eder, and Ullrich Steiner. Improved conductivity in dye-sensitised solar cells through block-copolymer confined TiO_2 crystallisation. *Energy Environ. Sci.*, 4(1):225–233, 2011. 68

[4] Stefan Guldin, Pablo Docampo, Morgan Stefik, Gen Kamita, Ulrich Wiesner, Henry J. Snaith, and Ullrich Steiner. Layer-by-layer formation of block-copolymer-derived TiO_2 for solid-state dye-sensitized solar cells. *Small*, 8(3):432–440, 2012. 68

[5] Morgan Stefik, Suntao Wang, Robert Hovden, Hiroaki Sai, Mark W. Tate, David A. Muller, Ullrich Steiner, Sol M. Gruner, and Ulrich Wiesner. Networked and chiral nanocomposites from abc triblock terpolymer coassembly with transition metal oxide nanoparticles. *J. Mater. Chem.*, 22(3):1078–1087, 2012. 71

[6] SA Bagshaw, E Prouzet, and TJ Pinnavaia. Templating of mesoporous

molecular-sieves by nonionic polyethylene oxide surfactants. *Science*, 269(5228):1242–1244, 1995. 71

[7] Markus Templin, Achim Franck, Alexander DuChesne, Heike Leist, Yuanming Zhang, Ralph Ulrich, Volker Schadler, and Ulrich Wiesner. Organically modified aluminosilicate mesostructures from block copolymer phases. *Science*, 278(5344):1795–1798, 1997. 71

[8] P.F.W. Simon, R Ulrich, HW Spiess, and U Wiesner. Block copolymer-ceramic hybrid materials from organically modified ceramic precursors. *Chem. Mater.*, 13(10):3464–3486, 2001. 71

[9] V. Shklover, Yu. E. Ovchinnikov, L. S. Braginsky, S. M. Zakeeruddin, and M. Gratzel. Structure of organic/inorganic interface in assembled materials comprising molecular components. crystal structure of the sensitizer bis[(4,4 '-carboxy-2,2 '-bipyridine)(thiocyanato)]ruthenium(ii). *Chem. Mater.*, 10(9):2533–2541, 1998. 72

[10] Giorgio Bazzan, James R. Deneault, Tae-Sik Kang, Barney E. Taylor, and Michael F. Durstock. Nanoparticle/dye interface optimization in dye-sensitized solar cells. *Adv. Funct. Mater.*, 21(17):3268–3274, 2011. 72

[11] D. A. G. Bruggeman. Calculation of various physics constants in heterogenous substances i dielectricity constants and conductivity of mixed bodies from isotropic substances. *Ann. Phys.*, 24(7):636–664, 1935. 72

[12] Stefan Guldin, Mathias Kolle, Morgan Stefik, Richard Langford, Dominik Eder, Ulrich Wiesner, and Ullrich Steiner. Tunable mesoporous bragg reflectors based on block-copolymer self-assembly. *Adv. Mater.*, 23(32):3664–3668, 2011. 73

[13] Ning Cai, Soo-Jin Moon, Le Cevey-Ha, Thomas Moehl, Robin Humphry-Baker, Peng Wang, Shaik M. Zakeeruddin, and Michael Gratzel. An organic d-p-a dye for record efficiency solid-state sensitized heterojunction solar cells. *Nano Lett.*, 11(4):1452–1456, 2011. 74, 75

[14] Benjamin J. Morgan and Graeme W. Watson. A dft + u description of oxygen vacancies at the TiO_2 rutile (1 1 0) surface. *Surf. Sci.*, 601(21):5034 – 5041, 2007. 75

[15] Victor E. Henrich, G. Dresselhaus, and H. J. Zeiger. Observation of two-dimensional phases associated with defect states on the surface of TiO_2. *Phys. Rev. Lett.*, 36:1335–1339, 1976. 75

[16] P.Madhu Kumar, S. Badrinarayanan, and Murali Sastry. Nanocrystalline TiO_2 studied by optical, ftir and x-ray photoelectron spectroscopy: correlation to presence of surface states. *Thin Solid Films*, 358(1-2):122 – 130, 2000. 75, 76

[17] Wha-Tek Kim, Chang-Dae Kim, and Q. Won Choi. Sub-band-gap photoresponse of tio2-x thin-film-electrolyte interface. *Phys. Rev. B*, 30:3625–3628, 1984. 75

[18] Henry J. Snaith, Annamaria Petrozza, Seigo Ito, Hidetoshi Miura, and Michael Gratzel. Charge generation and photovoltaic operation of solid-state dye-sensitized solar cells incorporating a high extinction coefficient indolene-based sensitizer. *Advanced Functional Materials*, 19(11):1810–1818, 2009. 75

[19] K. D. Benkstein, N. Kopidakis, J. van de Lagemaat, and A. J. Frank. Influence of the percolation network geometry on electron transport in dye-sensitized titanium dioxide solar cells. *J. Phys. Chem. B*, 107(31):7759–7767, 2003. 76

[20] Stefan Guldin, Sven Huttner, Priti Tiwana, M. Christopher Orilall, Burak Ulgut, Morgan Stefik, Pablo Docampo, Matthias Kolle, Giorgio Divitini, Caterina Ducati, Simon A. T. Redfern, Henry J. Snaith, Ulrich Wiesner, Dominik Eder, and Ullrich Steiner. Improved conductivity in dye-sensitised solar cells through block-copolymer confined TiO_2 crystallisation. *Energy Environ. Sci.*, 4(1):225–233, 2011. 76

Chapter 6

Pore-filling of mesoporous TiO_2 structures

6.1 Introduction

While issues with efficient charge generation have been extensively addressed (though not resolved) in earlier work and in the previous chapters,[1, 2, 3, 4, 5, 6, 7] the related challenges of effective pore filling and sufficient panchromatic absorption remains unsolved. The use of novel panchromatic absorbers may extend the absorption range from currently 425-650 nm to 425-940 nm, with a potential gain of 60% extra in short-circuit current, thus an extra 25% in power conversion efficiency despite the accompanied loss in voltage due to the reduced bandgap of the absorber.[8] However, in order to utilize panchromatic absorbers efficiently, film thickness needs to exceed the current apparent limit of 2 μm.

The pore filling mechanism in solid-state dye-sensitized solar cells has recently been the focus of a number of research groups. Multiple studies suggest that pore filling is the limiting factor to achieving thick cells (on the order of 5 μm),[9, 10, 11, 12] and thus impeding effective light absorption by the most common sensitizers.

It is therefore of central importance to measure this quantity as accurately as possible, and to fully understand if the pore filling alone is really responsible for the thickness limitation.

Several strategies have been proposed in order to measure pore-filling in solid-state dye-sensitized solar cells. One method employs photoinduced absorption spectroscopy, however this only allows determination of the uniformity of "pore wetting" - the actual filling fraction cannot be quantified.[13] A second method estimates the pore filling fraction by comparing films coated from the same solutions under identical conditions on both flat and porous substrates. Accounting for the initial solution which soaks into the mesoporous film, estimations of the pore filling fraction can be made by measuring the film thickness in cross-sectional SEM, and assuming that all the material which is not on top of the mesoporous films is in the pores.[9] A third method is similar to the 2^{nd}, but instead of comparing to a film coated on a flat substrate, the quantity of hole-transporter in the mesoporous film is quantified by redissolving the hole transporter in a chlorobenzene solution. Knowing the amount of solvent and the absorption spectra of the solution, the molarity of the hole transporter in the solution can be calculated. From this number and the geometry of the cell, the pore filling can be estimated.[10]

Neither SEM microscopy nor photoinduced absorption measurements allow an accurate measure of the pore filling fraction. The recently introduced redissolution technique has proven effective, yet this method requires making assumptions on the porosity of the film and the occupied volume fraction of the chemisorbed dye that lead to some ambiguity in the results. Furthermore this method requires the destruction of the cell in order to be measured, and is critically dependent upon the estimation of the density of the hole-transporter, which as will be discussed later is a potential source for error.

Herein, a simple, non-destructive method to determine the pore-filling of mesoporous photoanodes by an optical method is proposed. Based on thin film interference, the spectral reflection of the films allows the determination of the wavelength dependent refractive index of the films with a conventional spectrophotometer. Following the Bruggeman effective medium approximation, the volume fractions of all of the film components can be estimated. Furthermore, a

simplified method whereby the pore filling fractions and the capping layer thickness can be measured through the determination of the averaged effective refractive index for a range of hole transporter concentrations in the casting solution is proposed.

6.2 Results and discussion

6.2.1 Estimating the refractive index

When a beam of light travels through an interface between two materials with different indices of refraction, it will divide into a transmitted component and a reflected component.[14] A diagram of such a beam is schematically represented in figure 6.1 for light traveling to a surface at an incident angle for clarity. The relative fractions of the split beams are given by the Fresnel coefficients, which in the case of light traveling parallel to the normal of the interface reduce to:

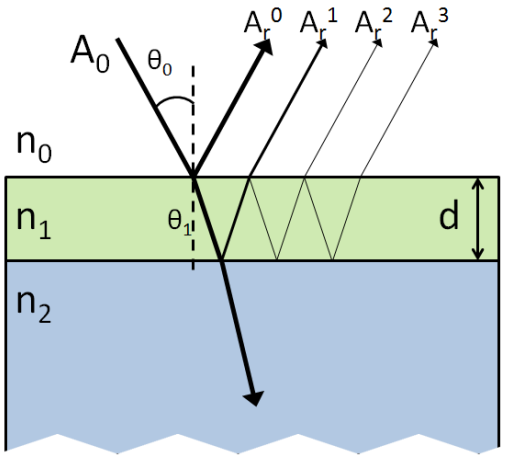

Figure 6.1: Schematic illustration of the multiple reflections occurring at a thin film interface.

$$r_{jk} = \frac{n_j - n_k}{n_j + n_k} \; ; \qquad t_{jk} = \frac{2n_j}{n_j + n_k}; \tag{6.1}$$

Where r_{jk} and t_{jk} are the Fresnel coefficient for reflected and transmitted light respectively from material j into material k, where j and k can be any consecutive materials in the stack, and n_j is the refractive index of each of the components. For a beam reflected from a thin film as represented in figure 6.1, there will be a phase difference (Δ), for the component reflected off the back surface with respect to component reflected from the front surface, and a subsequent phase shift of Δ

for each subsequent reflection due to the fact that light has traveled increasingly far through the thin film. The total amplitude (A_r) of the electric field of the reflected beam will be the result of adding all the individual reflections:

$$\begin{aligned}
A_r^0 &= A_0 r_{01} \\
A_r^1 &= A_0 (t_{01} t_{10} r_{12}) e^{i\Delta} \\
A_r^2 &= A_0 (t_{01} t_{10} r_{12}^2 r_{10}) e^{2i\Delta} \\
A_r^3 &= A_0 (t_{01} t_{10} r_{12}^3 r_{10}^2) e^{3i\Delta} \\
&\vdots \\
A_r^j &= A_0 (t_{01} t_{10} r_{12}^j r_{10}^{j-1}) e^{ji\Delta}
\end{aligned}$$

$$A_r = A_r^0 + A_r^1 + A_r^2 + \cdots = A_0 (r_{01} + (t_{01} t_{10} \sum_{j=1}^{\infty} r_{12}^j r_{10}^{j-1} e^{ji\Delta}) \tag{6.2}$$

$$r_{01} = -r_{10} \text{ and } t_{01} t_{10} = \sqrt{1 - r_{01}} \sqrt{1 - r_{10}} = 1 - r_{01}^2 \tag{6.3}$$

Combining equations 6.2 and 6.3 gives:

$$A_r = A_0 \frac{r_{01} + r12 e^{i\Delta}}{1 + r_{12} r_{01} e^{i\Delta}} \tag{6.4}$$

The reflectance of the film is defined as $R = |A_r / A_0|^2$, and where λ is the wavelength of the incident light, hence:

$$R = \frac{r_{10}^2 + 2 r_{12} r_{01} cos\Delta + r_{12}^2}{1 + 2 r_{12} r_{01} cos\Delta + r_{10}^2 r_{12}^2} \tag{6.5}$$

$$\Delta = \frac{4\pi d n_1}{\lambda} \tag{6.6}$$

From equation 6.5, the reflectance will have a local maximum when cosΔ is maximum, and with equation 6.6 the relative positions of two consecutive maxima can be determined:[15]

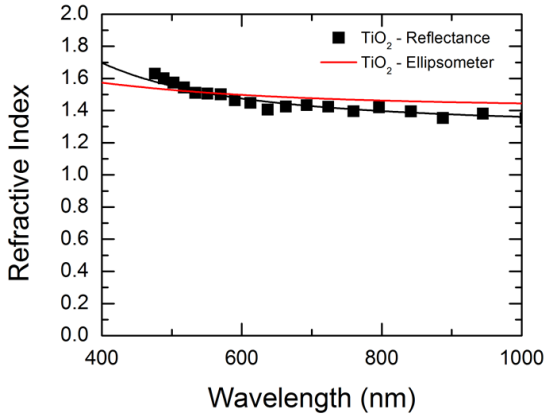

Figure 6.2: Wavelength dependent Refractive index, calculated from the reflectance spectrum (■) and measured with an spectroscopic ellipsometer (red line). Black line is the Cauchy function fit to the points calculated from the reflectance spectrum. I acknowledge that the ellipsometry data was acquired and analyzed by Stefan Guldin in the University of Cambridge.

$$\Delta_1 - \Delta_2 = \frac{4\pi d n_1}{\lambda_1} - \frac{4\pi d n_1}{\lambda_2} = 2\pi \tag{6.7}$$

From equation 6.7 the refractive index of the film can be determined:[16]

$$n_1 = \frac{1}{2d(\frac{1}{\lambda_1} - \frac{1}{\lambda_2})} \tag{6.8}$$

In dispersive media, such as in TiO_2, the refractive index will also depend on the incident wavelength, but its relationship can be approximated through a Cauchy function:[17]

$$n = A + \frac{B}{\lambda^2} \tag{6.9}$$

Thus, the wavelength-dependent refractive index of the films can be determined by measuring the reflectance of the films, identifying the local refractive index through the positions of consecutive maxima and minima with equation 6.8. Finally extract the refractive index can be extracted as a function of wavelength

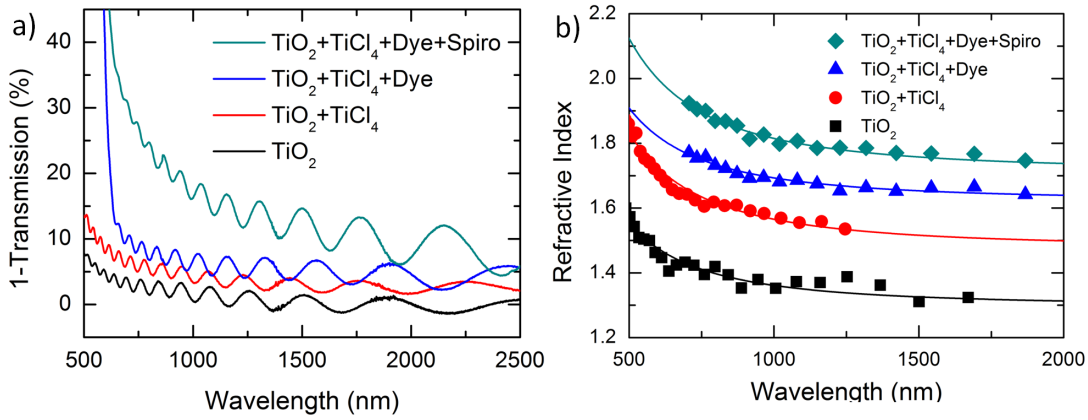

Figure 6.3: Wavelength dependent plots of a) reflectance spectra and b) refractive index for bare mesoporous TiO_2 films (■, bottom), TiO_2 with $TiCl_4$ surface treatment (●, 2nd from bottom), TiO_2 with $TiCl_4$ surface treatment and dye (▲, 2nd from top), TiO_2 with $TiCl_4$ surface treatment, dye and spiro-OMeTAD (◆, top). Lines in b) correspond to fits to the data with a Cauchy function.

by fitting the resulting dispersion with the Cauchy function 6.9. figure 6.3a shows the reflectance spectrum of typical films fabricated from mesoporous TiO_2 before and after the standard $TiCl_4$ treatment, with the addition of dye-sensitization and finally with the additional filling with the hole transporting material used in solid-state dye-sensitized solar cells, spiro-OMeTAD. figure 6.3b shows the estimated refractive indices as a function of wavelength and fit with equation 6.9. To further validate the proposed technique, thin films of mesoporous TiO_2 (∼500 nm) were measured with an ellipsometer, shown in Figure 6.2, where the results show excellent agreement between the two techniques with about a 5% difference between the calculated values at all studied wavelengths. Thicker films could not be measured in the ellipsometer due to scattering effects arising from the roughness of the films, as was found by other researchers.[17]

6.2.2 Estimating the film composition and pore filling

The TiO_2 photoanodes used in solid-state dye-sensitized solar cells are composed of nanocrystals about 20 nm in diameter, much smaller than the wavelength of light. For this reason, the occupied relative volume of TiO_2 and interstitial air voids can be related to the effective refractive index of the film using Bruggeman's

mean field approximation, where v_{air} refers to the volume fraction occupied by air, n_{TiO_2} to the refractive index of anatase TiO_2, and n_{film} to the refractive index of the film:[18, 19, 20]

$$(1 - v_{air})\frac{(n_{TiO_2}^2 - n_{film}^2}{n_{TiO_2}^2 + 2n_{film}^2} + v_{air}\frac{1 - n_{film}^2}{(1 + 2n_{film}^2} = 0 \tag{6.10}$$

Assuming a refractive index of 2.5 for anatase TiO_2 at 600 nm,[19] a porosity (v_{air}) of 62 $\pm$ 1% for mesoporous films prepared with a TiO_2 nanoparticle paste can be extracted, which reduces to 49 $\pm$ 1% after treatment with an aqueous $TiCl_4$ solution to improve photoanode performance in DSCs.[21, 22] Once the porosity of the film is known, a linear approximation can be used to estimate the volume fraction of the rest of the components, where v_i and n_i refer to the volume fraction and refractive index of the i^{th} component respectively:[23]

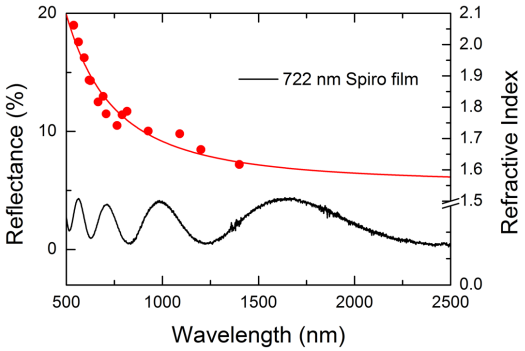

Figure 6.4: Plot of reflectance (left) and refractive index (right) against wavelength for a 722nm spiro-OMeTAD thick film. Red line corresponds to the fit of the refractive index points with a Cauchy function.

$$n_f = \sum_i v_i n_i = v_{air}n_{air} + v_{TiO_2}n_{TiO_2} + v_{dye}n_{dye} + v_{spiro}n_{spiro} \tag{6.11}$$

This linear approximation proves sufficiently accurate for multicomponent systems.

To calculate the volume fraction of the dye in the system, dye desorption was carried out with a solution of potassium hydroxide in methanol. Measuring the absorption spectrum of the desorbed dye solution (of controlled volume) allows the calculation of the solution molarity and hence amount of chemisorbed dye and thus its occupied volume in the mesoporous film (assuming that the density

of the dye is similar to that of its main indoline constituent component which is approximately 1 gml^{-1}). Consequently, a refractive index of 1.73±0.02 at 600 nm was extracted from reflectance measurements of the dye-sensitized films for the indoline based dye used in this study, termed D102. The refractive index of a thin film of spiro-OMeTAD was determined from the reflectance spectra, shown in Figure 6.4 where a value of 1.93±0.03 at 600 nm was found, in reasonable agreement with other organic semiconductors used in photovoltaic devices.[24]

Once a solution of a sufficiently high concentration of spiro-OMeTAD has been spin-coated on the mesoporous film, a capping layer will form on top of the infiltrated film. Once this happens, the optical system has to be extended to account for this extra layer of spiro-OMeTAD. However, the refractive index of the active layer with maximally filled pores without a capping layer and the refractive index of spiro-OMeTAD are rather similar (at 600 nm, 1.93 for the former and 2.11 for the latter), and thus reflections arising from the capping layer and the filled mesoporous TiO_2 interface shall be neglected in the following analysis. The difference in phase between two consecutive maxima at normal incidence, where n_{CL} is the contribution to the refractive index arising from the capping layer, can be written as:

$$\Delta_1 - \Delta_2 = \frac{4\pi(t_{TiO_2} n_f + n_{spiro} t_{CL})}{\lambda_1} - \frac{4\pi(t_{TiO_2} n_f + n_{spiro} t_{CL})}{\lambda_2} = 2\pi \qquad (6.12)$$

where d_{TiO_2} is the thickness of the mesoporous TiO2 layer, d_{CL} the thickness of the spiro-OMeTAD capping layer, and n_{CL} its contribution to the refractive index

$$n_f = \frac{1}{2t_{TiO_2}(\frac{1}{\lambda_1} - \frac{1}{\lambda_2})} - \frac{n_{spiro} t_{CL}}{t_{TiO_2}} \qquad (6.13)$$

$$n_{CL} = \frac{n_{spiro} t_{CL}}{t_{TiO_2}} \qquad (6.14)$$

In figure 6.6.a the pore filling fractions attained for different concentrations of the spiro-OMeTAD casting solution calculated using equation 6.11 are shown. To extract the refractive index of the films when no capping layer is present,

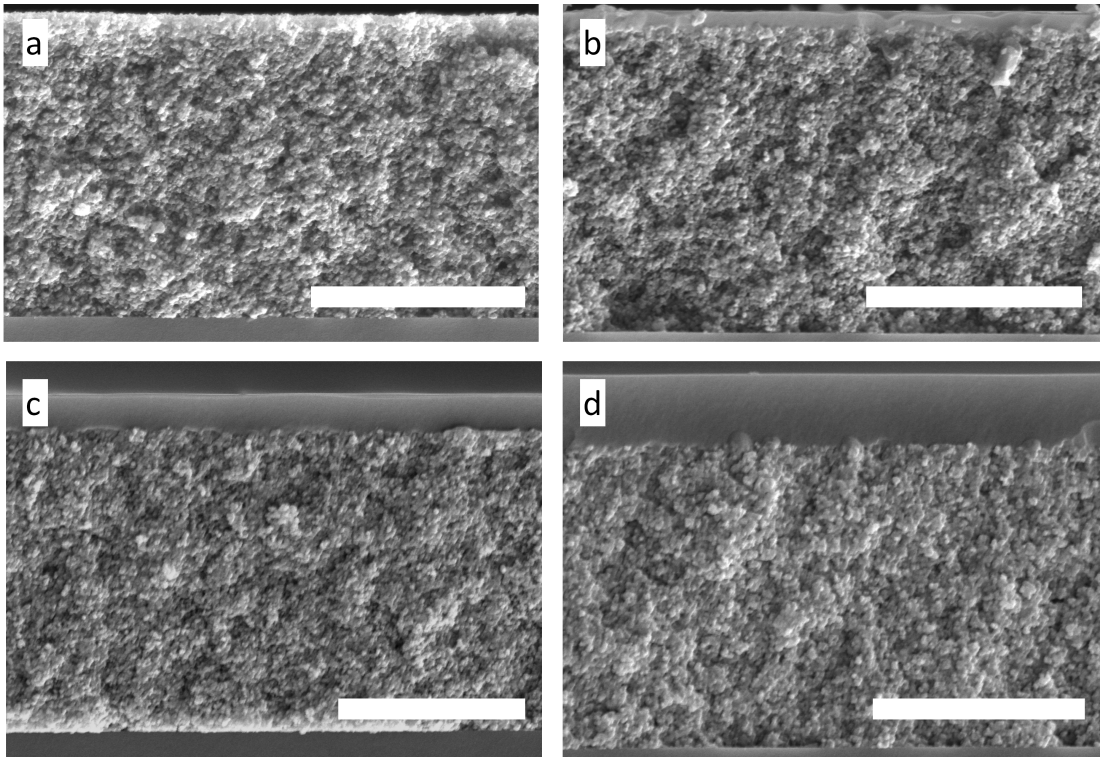

Figure 6.5: Cross-sectional SEM images of mesoporous TiO_2, after $TiCl_4$ treatment, with dye and filled from solutions of a) 11%, b) 13%, c) 15% and d) 17% of spiro-OMeTAD. Scale bars correspond to a length of 2 μm.

equation 6.8 was used, and once this layer forms, equation 6.13 was used. To monitor the capping layer thickness, cross sectional SEMs of all concentrations were taken, shown in Figure 6.5, and the results are summarized in figure 6.6.b.

Table 6.1 summarizes the volume fractions and refractive indices of the different components of an optimized photoanode.

The method presented above is a relatively straight forward route to estimating the pore filling fraction. The only assumption is that the pore filling is uniform from top to bottom, which is well supported by previous literature.[7, 9, 10] However, beyond simply measuring the pore filling, it would be useful to have a predictive tool which can enable the estimation of the pore filling for given coating conditions. The parameters which will strongly influence the coating and pore-filling are film porosity, coating spin-speed, environment temperature and atmosphere, solvent viscosity, hole-transporter concentration in the solvent (c)

	n at 600 nm
n_{TiO_2} [19]	2.5
n_{dye}	1.73 ±0.02
n_{spiro}	1.93 ±0.03
n_{film} (air/TiO_2+$TiCl_4$)	1.73 ±0.02
n_{film} (air/TiO_2+$TiCl_4$/dye)	1.81 ±0.02
n_{film} (air/TiO_2+$TiCl_4$/dye/spiro)	2.11 ±0.03
v_{dye}	0.04 ±0.03
v_{TiO_2}	0.52 ±0.01
v_{spiro}	0.33±0.05
v_{air}	0.10
filling fraction	0.78±0.11

Table 6.1: Summary of the refractive indices and volume fractions of each of the components in an optimized photoanode.

and solution viscosity (if there are any changes to viscosity with increasing hole-transporter concentration). For a given spin-speed and coating environment, the hole-transporter concentration is the main parameter to be tuned to optimize the pore filling. If the assumption that the solution viscosity does not change significantly with spiro-OMeTAD concentration (which appears to be true) is made, then an expression for the filling fraction as a function of solution concentration (c) can be formulated.

When coating a mesoporous film of thickness t and porosity p the total amount spiro-OMeTAD available to fill the pores at the start of spin-coating is the sum of the amount of material within the solution soaked into the mesoporous film ($t \cdot c \cdot p$), plus the amount of material on top of the mesoporous film within the wet solution film right at the start of spin-coating ($c \cdot t_{wet}$).Where the initial thickness of the wet solution layer before solvent evaporation starts is t_{wet}. Once solvent drying has occurred and complete film formation finalized, any of this available material which does not infiltrate into the mesoporous film, forms a capping layer on top with thickness t_{CL}. A schematic of this process to aid the reader is shown in figure 6.7. Hence, as described elsewhere, the pore-filling fraction (PF) can be

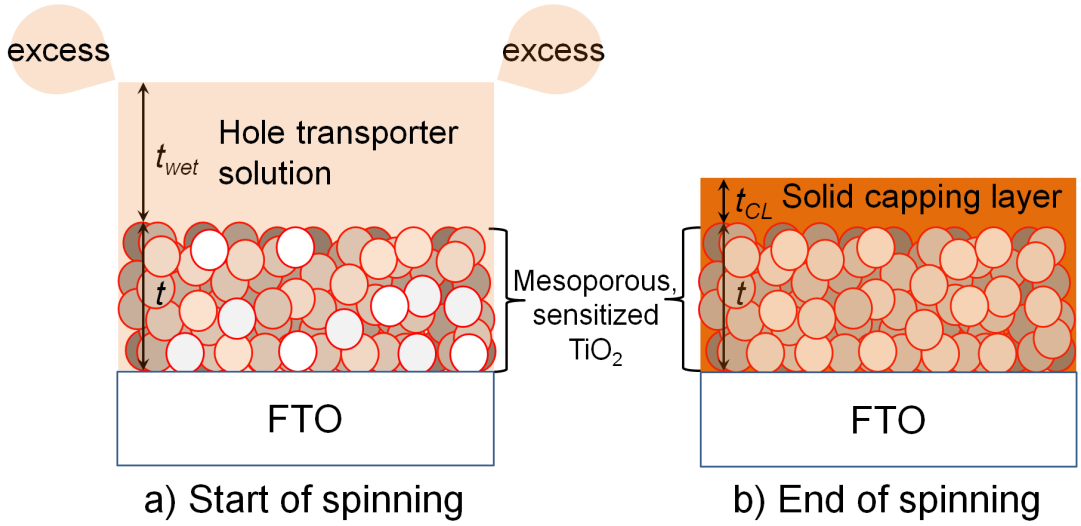

Figure 6.7: Schematic representation of the spincoating process. a) In the initial stages of spin-coating, a large quantity of solution flows off the substrate (labeled excess) and a wet layer of uniform thickness (t_{wet}) is formed above the mesoporous substrate prior to evaporation. b) Represents the final result after the solvent has completely evaporated and where the hole transporter that has not infiltrated the pores remains over the mesostructure, forming a solid capping layer of uniform thickness (t_{CL}).

written as:[9]

$$PF = c + \frac{t_{wet}c - t_{CL}}{tp} \tag{6.15}$$

Using this equation to fit the data in figure 6.6.a, a wet layer thickness of 6.9±0.5 μm was extracted, consistent with other reports in literature.[9, 10] Calculating the concentration of the spiro-OMeTAD:chlorobenzene solution requires knowledge of the density of spiro. This property was calculated by re-dissolving films of Spiro-OMeTAD of known thickness and area in chlorobenzene, and then taking UV-visible absorption spectra of the resulting solution to deduce the concentration (see section 3.3). This gave a value of 1.02±0.03 gcm^{-3},[1] in agreement with estimations used previously.[9]

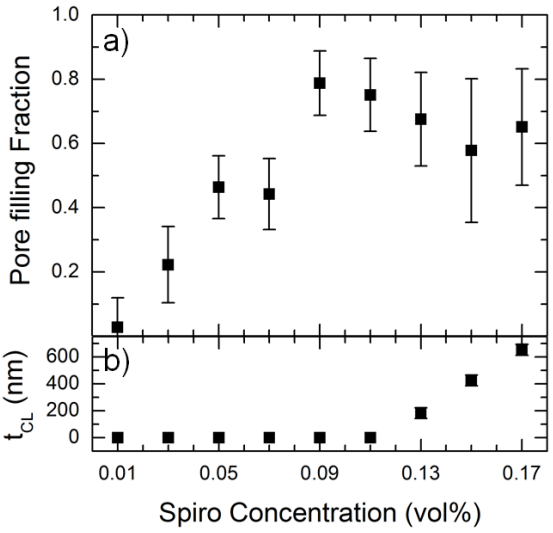

Figure 6.6: a) Pore filling fraction and b) capping layer thickness estimated by SEM images versus the concentration of spiro-OMeTAD in the casting solution. The underlying films constituted of mesoporous TiO_2 with $TiCl_4$ surface treatment, dye and spiro-OMeTAD. Error bars were estimated from the propagation of the error in the fit of the Cauchy function.

So far, the method described requires the determination of the refractive index from consecutive fringes, which is then fitted to a Cauchy function, while the capping layer thickness has to be determined by an alternative method. Unfortunately, this requires access to expensive equipment such as SEM or other optical instruments, introduces extra error since the capping layer estimation is highly subject to local

[1] This value is significantly different to 1.82 gcm^{-3} obtained by Ding et al. by measuring the mass of a silicon wafer before and after coating with Spiro-OMeTAD.[10] I believe this has introduced an error in their concentration values leading to a significant underestimation of the pore filling fractions reported.

thickness variations, and is also destructive and hence not useful for inline determination of pore filling in a production setting. However, it should be possible to monitor the capping layer thickness by its optical footprint in the UV-Vis reflectance. As is apparent from figure 6.6.a, the concentration at which the pores are optimally filled corresponds to the concentration at which the capping layer starts to form. In principle, when this layer is added, the reflectance spectrum will exhibit secondary cosine terms arising from the interface between the capping layer and the filled mesoporous layer. From this interaction the capping layer thickness can also be extracted. Unfortunately, the refractive indices of these layers are very similar, as mentioned previously, and the available wavelength range is limited. For these reasons the accurate determination of the capping layer through these means was practically impossible.

Another simpler option is to define an effective refractive index (n_{eff}) for a film of fixed thickness t where the contribution from the capping layer is integrated with that of the filled mesoporous layer using equation 6.13. By combining equations 6.8, 6.11 and 6.15, assuming that the pore filling fraction remains approximately constant after the formation of the capping layer and knowing from eq. 6.13 that the contribution from the capping layer scales as n_{CL}, then:

$$n_{eff} = \begin{cases} v_{pores} + v_{TiO_2} n_{TiO_2} + v_{dye} n_{dye} + (n_{spiro} - 1) \frac{1+t_{wet}}{t_{TiO_2} v_{pores}} v_{pores} c & \text{if } t_{CL} = 0, \\ n_{eff,CL=0} + \frac{n_{spiro} t_{CL}}{t_{TiO_2}} & \text{if } t_{CL} \neq 0 \end{cases} \tag{6.16}$$

Where $n_{eff,CL=0}$ is the maximum refractive index of the film before the capping layer forms. It is clear from this equation that the effective refractive index of the film will scale as a function of the refractive index of spiro-OMeTAD, wet layer thickness, thickness of TiO_2 and the volume of the pores with increasing spiro-OMeTAD concentration when no capping layer is present. When this layer is formed, the effective refractive index will have an additional component within the sum, which scales as n_{CL}. Finding the concentration value which results in the maximum pore filling fraction is then a simple matter of plotting the effective refractive index against spiro-OMeTAD concentration and checking at which point the change in slope appears.

Furthermore, using this simple effective refractive index approximation, accurate values for the capping layer thickness can be extracted since the gradient of the effective refractive index versus concentration after the formation of the capping layer will be proportional to this quantity. As seen from SEM measurements, the capping layer thickness can be fitted with a linear model, where A is the equivalent solid thickness of the spiro-OMeTAD in the pores at the maximum pore filling fraction:

$$t_{CL} = A + Bc \tag{6.17}$$

We have found experimentally that the uncertainty in the measurements can be considerably reduced, particularly after the formation of the capping layer, if a wavelength averaged effective refractive index ($n_{av,eff}$) in the region where none of the constituent components absorb (650 to 2500 nm in the present system) is used:

$$n_{av,eff} = \frac{\#\text{ of maxima}}{2t_{TiO_2}(\frac{1}{\lambda_1} - \frac{1}{\lambda_2})} \tag{6.18}$$

To apply this averaged, effective refractive index, the values for the wavelength dependent refractive index of TiO_2, dye and spiro-OMeTAD also need to be averaged between the studied interval of 650 to 2500 nm. With the value for v_{dye} calculated dye desorption measurements, an averaged refractive index of 1.65 for the D102 dye used was extracted. The averaged refractive index for spiro-OMeTAD of 1.81 was calculated from reflectometry measurements on a flat film, shown in Figure 6.4. Finally, the averaged refractive index of 2.17 for TiO_2 was calculated from the experimental data for the mesoporous TiO_2 presented in this chapter.

In figure 6.8.a) the averaged, effective refractive index is shown against a range of concentrations. It is apparent that a change in slope is found when the capping layer is formed, (points shown as red circles). The behavior of the averaged effective refractive index can be predicted using equation 6.16, shown as

a blue line in figure 6.8.a), with $t_{wet} = 6.9\mu m$ (see figure 6.6.a) and the parameters for the capping layer thickness A=-1340 and B=11740 nm 6.17 (extracted from SEM measurements, see Figure 6.5).

The two presented methods to extract the pore filling fraction of the films, i.e. using wavelength dependent refractive index, as shown in figure 6.6.a) and those extracted from the averaged effective refractive index, can be checked for consistency. Indeed, by extracting the slope of the experimental data for films which do not exhibit a capping layer, shown in figure 6.8.a) as black squares, a wet layer thickness (t_{wet}) of 7.2±0.3 μm can be calculated, which is within experimental error to the one found by using the wavelength dependent refractive index (6.9±0.5 μm) from figure 6.6.a.

In figure 6.8.b the pore filling fractions calculated from the averaged, effective refractive index are shown against spiro-OMeTAD concentration. The use of the averaged, effective refractive index has significantly reduced the pore filling fraction error as compared to the data presented in figure 6.6.a.

By performing a linear fit with the points after the capping layer has been formed (shown as red circles in figure 6.8.a), the capping layer thickness can be extracted from its slope for a known spiro-OMeTAD concentration at the point of maximally filled pores. For this system, it was determined visually as 11%. The results are shown in figure 6.8.c), where the calculated capping layer thickness very closely follows the measured thicknesses via SEM cross sectional images. At the highest concentrations, a slight discrepancy between the thickness estimation of the capping layer and SEM measurements was observed. This can be associated with the assumption of a constant pore filling fraction after the capping layer has formed. Indeed, the values for the pore filling fractions shown in figure 6.8.b) seem to slightly decrease after the formation of the capping layer. However, this is debatably constant considering the error margins.

In figure 6.8.d, the concentration of spiro-OMeTAD which results in optimally filled pores against thickness is predicted for a range of available pore volumes of the mesostructure In order to calculate these values, t_{wet} was taken as 7.2 μm and was assumed independent of spiro-OMeTAD concentration, available pore volume fraction and thickness of the mesoporous TiO_2 layer. It is very interesting to note that reduced porosity should counter intuitively deliver improved pore filling in

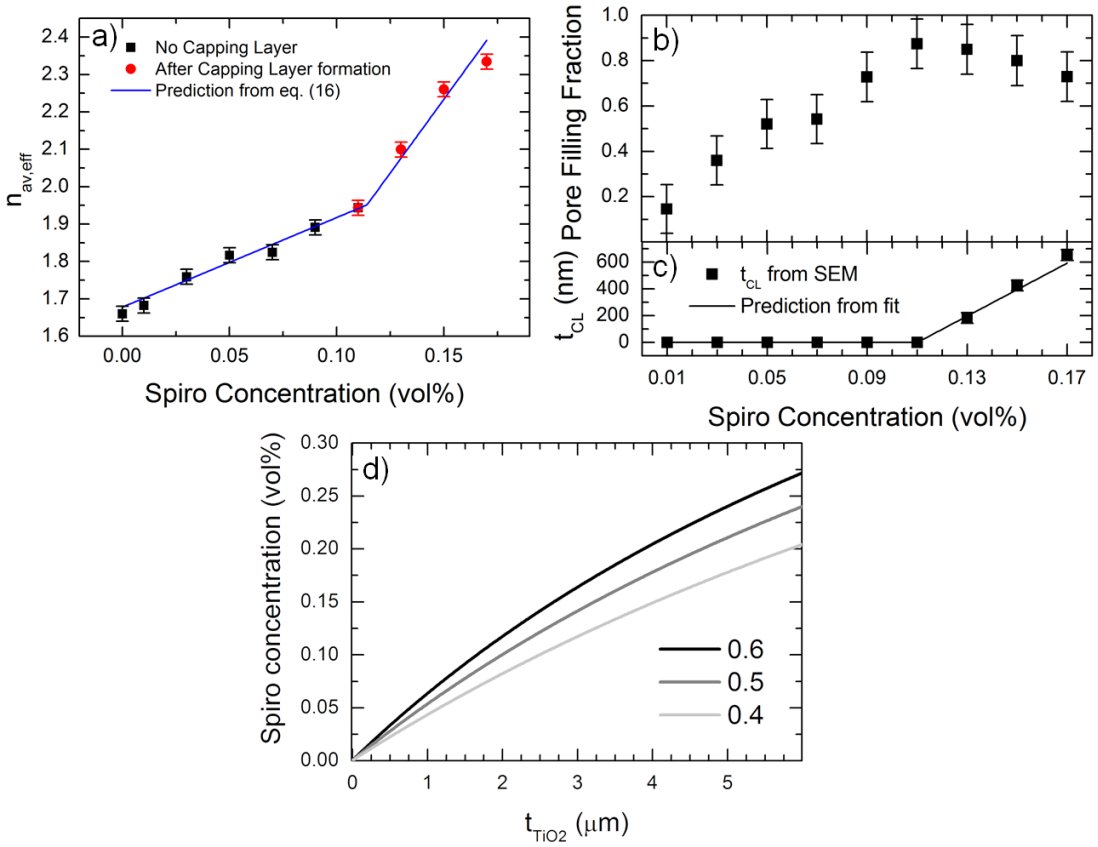

Figure 6.8: (a) Plot of averaged, effective refractive index against casting spiro-OMeTAD solution concentration on mesoporous TiO_2 films after $TiCl_4$ treatment and dye-sensitization. Data points prior to the formation of a capping layer are shown as ■, data points once the capping layer is formed are shown as ●. The blue line corresponds to the theoretical prediction by using the calculated t_{wet} from figure 6.6.a and equation 6.16. (b) Calculated pore filling fractions against spiro-OMeTAD concentration from the averaged effective refractive index and equation 6.11, shown as ■. Error bars are estimated from the typical standard deviation found for 4 different substrates. (c) Capping layer thickness estimated from SEM measurements (■) plotted against casting spiro-OMeTAD solution concentration. The black line corresponds to the expected capping layer anticipated from (a). d) Prediction of spiro-OMeTAD casting solution concentrations that result in optimally filled pores against thickness of the mesostructured electrode for a range of available pore volumes, where (black, top) approximately corresponds to a typical mesoporous TiO_2 film fabricated from commercial pastes, (gray, middle) to the same substrate after the $TiCl_4$ treatment and (light gray, bottom) to the final dye-sensitized film. To calculate these concentrations, a t_{wet} was taken as 7.2 μm, and a maximum pore filling fraction of 80% was assumed.

thicker films, which represents an interesting future study.

As is apparent from figure 6.8.a, it is clearly discernible at which concentration the highest pore filling is achieved; i.e.no further analysis is needed for experimental pore filling optimization. If the viscosity of the solution did vary considerably with increasing concentration, the relationship between wet film thickness (t_{wet}) and concentration would have to be determined and added to the pore filling relation, equation 6.15. Although, equally notable, the observation that the pore filling scales linearly with concentration indicates that there is no significant change in this system to t_{wet} with the concentration range studied.

6.2.3 Device characterization

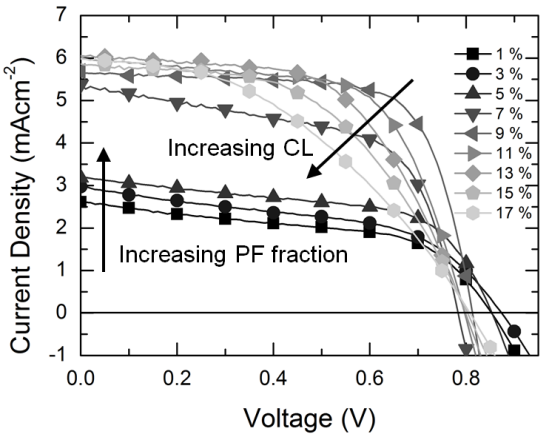

Figure 6.9: Current density against voltage plots for solid-state dye-sensitized solar cells fabricated with different vol% concentrations of spiro-OMeTAD measured under AM1.5 simulated sun light of 100mWcm^{-2} irradiance. Lighter shades of grey indicate higher concentrations (see legend). CL refers to the capping layer thickness and PF to the pore-filling fraction.

In order to relate the effects of pore filling to the photovoltaic performance, solid-state dye-sensitized solar cells were fabricated from a variety of spiro-OMeTAD, concentrations in the casting solution resulting in different pore filling fractions. The resulting JV curves are shown in figure 6.9, where a steady increase in short circuit current can be clearly seen as the pore filling fraction is increased until a maximum of 6.0 mAcm^{-2} is reached at the spiro-OMeTAD concentration corresponding to the highest pore filling fraction. As the concentration of the spiro-OMeTAD casting solution is increased further, the short circuit current changes minimally, but a lower fill factor of the cells is observed, indicating the increase of a series resistance, probably due to the increasing

c (vol%)	J_{SC}	η	V_{OC}	FF
1	0.2	0.1	0.73	0.36
3	3.0	1.3	0.87	0.5
5	3.2	1.6	0.85	0.58
7	5.4	2.5	0.78	0.59
9	5.7	3.2	0.81	0.71
11	6.0	3.1	0.80	0.66
13	6.0	2.7	0.80	0.57
15	5.9	2.4	0.80	0.52
17	6.0	2.0	0.81	0.42

Table 6.2: Photovoltaic performance parameters for a range of spiro casting solution concentrations

thickness of the spiro-OMeTAD capping layer. The maximum in power conversion efficiency of 3.2% occurs at 9% spiro-OMeTAD concentration, however the value for the optimum pore filling fraction, 11%, is very similar at 3.1% and well within experimental error. The results are summarized in table 6.2

To further probe the charge carrier kinetics of the system, photovoltage and photocurrent decay measurements at short circuit conditions were performed for cells of a variety of spiro-OMeTAD concentrations, shown in figure 6.11. A trend of prolonged recombination lifetimes with increasing pore filling fractions up to the highest pore filling fractions (after 9 vol% spiro-OMeTAD, or equivalently 60% pore filling fractions) can be seen. After this point, all the cells with the measured concentrations behave in a similar way, with overlapping points at all bias light intensities studied.

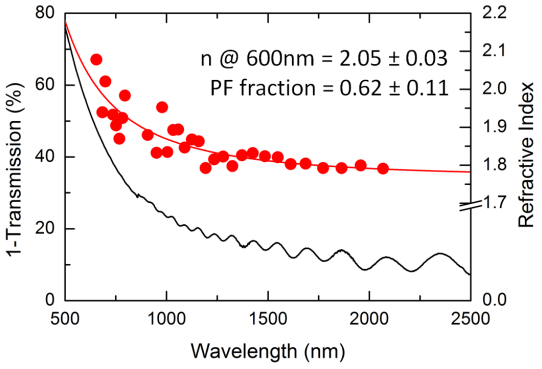

Figure 6.10: Transmittance (left) and refractive index (right) plot against wavelength for a 5.05 μm thick film filled with a spiro-OMeTAD concentration of 17 vol% (without dye). Red line corresponds to the fit of the refractive index points with a Cauchy function.

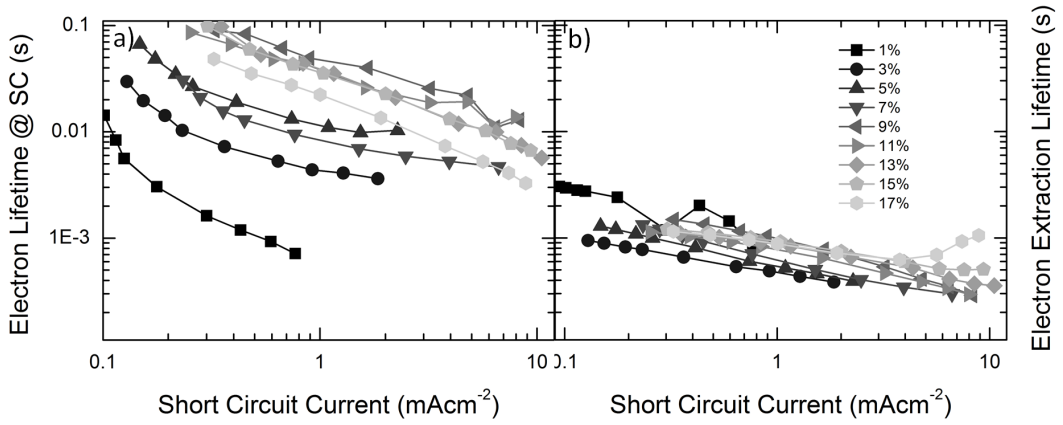

Figure 6.11: Photovoltage (a) and photocurrent (b) decay measurements at short circuit conditions against short circuit current for a range of spiro-OMeTAD casting solution concentrations (see legend).

These results are in good agreement with a study by Melas-Kyriazi et al,where improved pore filling was found to extend the electron lifetime at short circuit to around 10 ms.[25]

While the electron lifetime becomes longer the higher the pore-filling fraction, no trend was observed in regards to extraction lifetimes at high light bias, as shown in figure 6.9.b). In fact, most measurement points overlap. Longer lifetimes are only observed once the capping layer is formed, which allows to subsequently establish a correlation between capping layer thickness and electron extraction time at high light biases.

Following results from the device and pore-filling study, a pore-filling fraction with Spiro-OMeTAD of at least 60% is required to achieve optimized performance in solid-state dye-sensitized solar cells. In order to probe the upper limit for photoanode infiltration, 5.05 μm thick TiO_2 films were subjected to the $TiCl_4$ treatment and filled with a range of spiro-OMeTAD concentrations. A pore-filling fraction of 62±11% was measured, as shown in Figure 6.10, for the highest concentration used in this study. This proves that sufficient pore-filling of thick structures is in fact possible, and the limitations to the device thickness are rather due to poor charge collection issues related to the high recombination rates exhibited by this type of solar cell.[26, 27] Further studies optimising the com-

position of the hole-transporter and further adaptations to inhibit recombination in thicker films may alleviate this issue.

6.3 Conclusions

In summary, an optical technique based on the thin film interference effects of typical photoanodes used in solid-state dye-sensitized solar cells was developed to reliably estimate the pore-filling fractions of the assembled devices. By calculating the refractive index from the reflectance spectrum of the films and fitting the resulting values with a Cauchy function, the volume fraction of the constituent materials can be extracted. This non-destructive method can be used for films at the various stages of the fabrication process and does not require any material assumptions. Accordingly, pore-filling fractions of up to 80% were estimated for the optimized photoanodes. A simpler analysis can be applied after defining an "overall effective refractive index", which allows direct determination of the maximum pore-filling fraction for a range of hole-transporter casting solution concentrations. The photovoltage and photocurrent decay technique was used to determine the charge carrier transport and recombination lifetimes at short-circuit conditions as a function of pore-filling. It was found that with increasing pore-filling fractions, the lifetime of electrons was extended, while no trend was found in the transport kinetics. The main result of this work is that a pore-filling fraction of at least 60% is required to achieve optimized performance in solid-state dye-sensitized solar cells. Since it is possible to optimally fill structures up to 5 m in thickness, the limitations to device thickness must stem from the poor electron diffusion exhibited by these nanocrystalline TiO_2 networks combined with the high recombination rates caused by using spiro-OMeTAD as the hole transporter.

References

[1] Pablo Docampo, Stefan Guldin, Ullrich Steiner, and H. J. Snaith. Triblock terpolymer directed self-assembly of mesoporous TiO_2 - high performance

photoanodes for solid state dye-sensitized solar cells. *Advanced Energy Materials*, Accepted(–):–, 2012. 82

[2] Pablo Docampo, Stefan Guldin, Morgan Stefik, Priti Tiwana, M. Christopher Orilall, Sven Huttner, Hiroaki Sai, Ulrich Wiesner, Ulrich Steiner, and Henry J. Snaith. Control of solid-state dye-sensitized solar cell performance by block-copolymer-directed TiO_2 synthesis. *Adv. Funct. Mater.*, 20(11):1787 – 1796, 2010. 82

[3] Y. Tachibana, J. E. Moser, M. Gratzel, D. R. Klug, and J. R. Durrant. Subpicosecond interfacial charge separation in dye-sensitized nanocrystalline titanium dioxide films. *Journal of Physical Chemistry*, 100(51):20056–20062, 1996. 82

[4] J.E. Kroeze, N. Hirata, L. Schmidt-Mende, C. Orizu, S.D. Ogier, K. Carr, M. Gratzel, and J.R. Durrant. Parameters influencing charge separation in solid-state dye-sensitized solar cells using novel hole conductors. *Advanced Functional Materials*, 16(14):1832–1838, 2006. 82

[5] J. E. Kroeze, N. Hirata, S. Koops, M. K. Nazeeruddin, L. Schmidt-Mende, M. Gratzel, and J. R. Durrant. Alkyl chain barriers for kinetic optimization in dye-sensitized solar cells. *Journal of the American Chemical Society*, 128(50):16376–16383, 2006. 82

[6] S. Koops, B. O'Regan, P. R. F. Barnes, and J. R. Durrant. Parameters influencing the efficiency of electron injection in dye-sensitized solar cells. *J. Am. Chem. Soc*, 131(13):4808–4818, 2009. 82

[7] Agnese Abrusci, I. Kang Ding, Mohammed Al-Hashimi, Tamar Segal-Peretz, Michael D. McGehee, Martin Heeney, Gitti L. Frey, and Henry J. Snaith. Facile infiltration of semiconducting polymer into mesoporous electrodes for hybrid solar cells. *Energy & Environmental Science*, 4(8):3051–3058, 2011. 82, 90

[8] H. J. Snaith. Estimating the maximum attainable efficiency in dye-sensitized solar cells. *Advanced Functional Materials*, 20(1):13–19, 2010. 82

[9] Henry J. Snaith, Robin Humphry-Baker, Peter Chen, Ilkay Cesar, Shaik M. Zakeeruddin, and Michael Gratzel. Charge collection and pore filling in solid-state dye-sensitized solar cells. *Nanotechnology*, 19(42), 2008. 82, 83, 90, 93

[10] I. K. Ding, N. Tetreault, J. Brillet, B. E. Hardin, E. H. Smith, S. J. Rosenthal, F. Sauvage, M. Gratzel, and M. D. McGehee. Pore-filling of spiro-ometad in solid-state dye sensitized solar cells: Quantification, mechanism, and consequences for device performance. *Adv. Func. Matter.*, 19(15):2431–2436, 2009. 82, 83, 90, 93

[11] H.J. Snaith and L. Schmidt-Mende. Advances in liquid-electrolyte and solid-state dye-sensitized solar cells. *Adv. Mater.*, 19(20):3187–3200, 2007. 82

[12] Lukas Schmidt-Mende and Michael Gratzel. Tio2 pore-filling and its effect on the efficiency of solid-state dye-sensitized solar cells. *Thin Solid Films*, 500(12):296–301, 2006. 82

[13] U. B. Cappel, E. A. Gibson, A. Hagfeldt, and G. Boschloo. Dye regeneration by spiro-meotad in solid state dye-sensitized solar cells studied by photoinduced absorption spectroscopy and spectroelectrochemistry. *Journal of Physical Chemistry C*, 113(15):6275–6281, 2009. 83

[14] Max Born. Principles of optics : electromagnetic theory of propagation, interference and diffraction of light. *Cambridge University Press*, 7th Edition, 1999. 84

[15] Paul D. T. Huibers and Dinesh O. Shah. Multispectral determination of soap film thickness. *Langmuir*, 13(22):5995–5998, 1997. doi: 10.1021/la960738n. 85

[16] C. Pickering, M. I. J. Beale, D. J. Robbins, P. J. Pearson, and R. Greef. Optical properties of porous silicon films. *Thin Solid Films*, 125(12):157–163, 1985. 86

[17] Adam J. Moule, Henry J. Snaith, Markus Kaiser, Heike Klesper, David M. Huang, Michael Gratzel, and Klaus Meerholz. Optical description of solid-

state dye-sensitized solar cells. i. measurement of layer optical properties. *Journal of Applied Physics*, 106(7):073111–9, 2009. 86, 87

[18] D. A. G. Bruggeman. Calculation of various physics constants in heterogenous substances i dielectricity constants and conductivity of mixed bodies from isotropic substances. *Ann. Phys.*, 24(7):636–664, 1935. 88

[19] S. Y. Kim. Simultaneous determination of refractive index, extinction coefficient, and void distribution of titanium dioxide thin film by optical methods. *Applied Optics*, 35(34):6703–6707, 1996. 88, 91

[20] M. Khardani, M. Bouaicha, and B. Bessais. Bruggeman effective medium approach for modelling optical properties of porous silicon: comparison with experiment. *physica status solidi (c)*, 4(6):1986–1990, 2007. 88

[21] P. M. Sommeling, B. C. O'Regan, R. R. Haswell, H. J. P. Smit, N. J. Bakker, J. J. T. Smits, J. M. Kroon, and J. A. M. van Roosmalen. Influence of a $TiCl_4$ post-treatment on nanocrystalline TiO_2 films in dye-sensitized solar cells. *The Journal of Physical Chemistry B*, 110(39):19191–19197, 2006. 88

[22] Brian C. O'Regan, James R. Durrant, Paul M. Sommeling, and Nicolaas J. Bakker. Influence of the $TiCl_4$ treatment on nanocrystalline TiO_2 films in dye-sensitized solar cells. 2. charge density, band edge shifts, and quantification of recombination losses at short circuit. *The Journal of Physical Chemistry C*, 111(37):14001–14010, 2007. 88

[23] J. R. Birchak, C. G. Gardner, J. E. Hipp, and J. M. Victor. High dielectric constant microwave probes for sensing soil moisture. *Proceedings of the IEEE*, 62(1):93–98, 1974. 88

[24] Nils-Krister Persson, Mengtao Sun, Par Kjellberg, Tonu Pullerits, and Olle Inganas. Optical properties of low band gap alternating copolyfluorenes for photovoltaic devices. *The Journal of Chemical Physics*, 123(20):204718–9, 2005. 89

[25] John Melas-Kyriazi, I. Kang Ding, Arianna Marchioro, Angela Punzi, Brian E. Hardin, George F. Burkhard, Nicolas Tetreault, Michael Gratzel,

Jacques-E. Moser, and Michael D. McGehee. The effect of hole transport material pore filling on photovoltaic performance in solid-state dye-sensitized solar cells. *Advanced Energy Materials*, 1(3):407–414, 2011. 100

[26] Stefan Guldin, Sven Huttner, Priti Tiwana, M. Christopher Orilall, Burak Ulgut, Morgan Stefik, Pablo Docampo, Matthias Kolle, Giorgio Divitini, Caterina Ducati, Simon A. T. Redfern, Henry J. Snaith, Ulrich Wiesner, Dominik Eder, and Ullrich Steiner. Improved conductivity in dye-sensitised solar cells through block-copolymer confined TiO_2 crystallisation. *Energy Environ. Sci.*, 4(1):225–233, 2011. 100

[27] Francisco Fabregat-Santiago, Juan Bisquert, Le Cevey, Peter Chen, Mingkui Wang, Shaik M. Zakeeruddin, and Michael Gratzel. Electron transport and recombination in solid-state dye solar cell with spiro-ometad as hole conductor. *J. Am. Chem. Soc.*, 131(2):558–562, 2009. 100

Chapter 7

The role of an MgO shell on SnO_2-based dye-sensitized solar cells

7.1 Introduction

Shells of metal oxides have a profound impact on the different solar cell performance parameters. They affect diverse characteristics from inhibiting recombination, to enabling a higher degree of dye loading depending on the isoelectric point.[1, 2, 3] Of particular interest is a thin MgO layer over SnO_2-based DSCs, as it enables the efficient operation of this type of devices under normal simulated sunlight conditions, where devices barely reach 1% power conversion efficiencies without treatment in some cases and can reach over 7% after the addition of the MgO layer.[4, 5, 6] Although dye-sensitized solar cells fabricated from TiO_2 nanoparticles reach higher power conversion efficiencies than those fabricated from SnO_2, there is scope for large improvements in the latter system. Indeed, the use of TiO_2 as the mesostructured material limits the choice

of dyes that can transfer charge efficiently to its CB, which in state-of-the-art devices typically means an optical band-gap of about 1.48 eV. In SnO_2 the CB is located between 0.3 and 0.5 eV further from vacuum than TiO_2. This enables targeting narrower band-gap sensitizers in combination with currently available electrolyte/hole-transport systems, which in turn opens up the possibility of aiming for higher achievable power conversion once all losses have been minimized.[7] Beyond possible efficiency motivations, concerning stability, SnO_2 has a band gap of 3.8 eV and is a less effective photocatalyst than TiO_2 which should give less stringent demands for UV filtration.

When the TiO_2 in the mesostructure is substituted for SnO_2 in solid-state based dye-sensitized solar cells, and a conformal, thin shell of MgO is deposited, a near unity internal photon-to-electron conversion efficiency has been observed.[8] Despite MgO having been extensively employed for SnO_2 based DSCs, there is still not a clear understanding of its complete function in the solar cells. In this chapter, the effects of the deposition of a shell of MgO over SnO_2 based DSCs on their electronic properties were studied, using both a conventional low volatile iodide/triiodide "Robust" liquid electrolyte and Spiro-OMeTAD as the hole transporters.

7.2 Results and discussion

7.2.1 Photovoltaic characteristics

For the remainder of the chapter, solar cells incorporating a thin MgO layer chemically deposited via a 20 mM ethanolic bath of Mg-acetate for 1 minute under boiling conditions over the SnO_2 mesostructure prior to dyeing will be referred to as "SnO_2-MgO" devices. Devices where the surface was not modified will be referred to as "bare" or "SnO_2". In figure 7.1.a the current voltage curves for both liquid electrolyte (7.1.a) and solid-state (7.1.b) DSCs are shown. In all previous reports on SnO_2 based DSCs the introduction of a MgO interlayer results in a significant increase in the photocurrent generated by the solar cell. In this study however, the opposite was repeatedly observed and the bare SnO_2 devices already exhibit extremely high photocurrents, as shown in Figure 7.1.a where the

cell generates 17.1 mAcm^{-2}. For the SnO_2-MgO liquid electrolyte based solar cells, the short-circuit current is reduced, as shown in the example of figure 7.1 where the SnO_2-MgO device generates 15.7 mAcm^{-2} under 100 mWcm^{-2} AM 1.5 simulated solar light. However, for the solid-state DSCs the expected trend was observed, where the current increased with the addition of MgO from 2.7 to 5.2 mAcm^{-2}. The results are summarized in table 7.1.

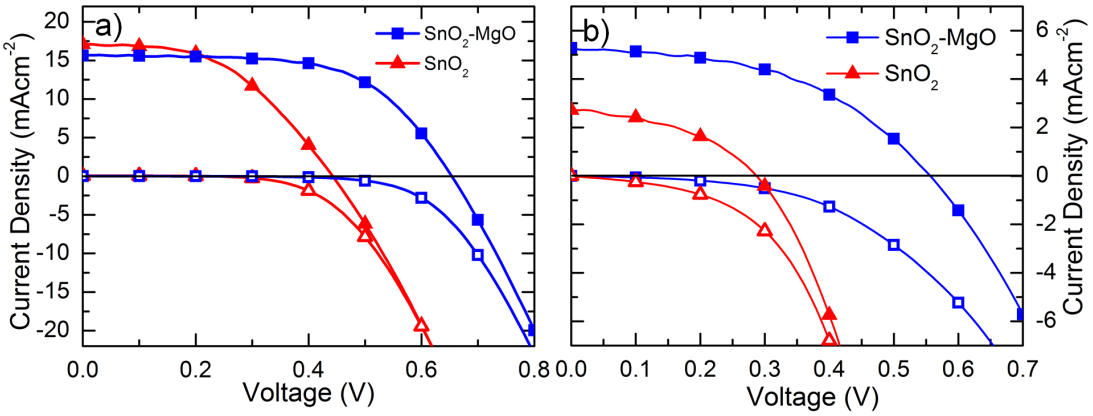

Figure 7.1: Current voltage characteristics of devices incorporating a thin MgO layer (■) and no surface treatment, labeled bare (▲), where a) are liquid electrolyte based devices, b) solid-state based devices. I acknowledge that Henry J. Snaith in the University of Oxford fabricated and measured the electrolyte cells presented in this figure.

Both solid-state and electrolyte based cells show an overall significant increase in efficiency upon MgO treatment. However, the contrary shifts in short-circuit photocurrent indicate that multiple competing factors may be at play. In previous studies, increased photocurrent has been explained by the higher isoelectric point of MgO compared to SnO_2 which would allow a higher dye loading. [3, 4] Higher dye loading is indeed observed, however, absorption spectra for films with and without the MgO surface treatment indicate that the magnitude of the increase in light absorption, which is only a 9% difference over the solar spectrum, does not account for the difference in short-circuit current (figure 7.2).

In addition to the changes in photocurrent, for both liquid and solid-state cells an increase in open-circuit voltage of ∼200 to 300 mV for SnO_2-MgO devices is observed, as compared to the bare devices. This has been attributed in the past

	Electrolyte		Solid-State	
	SnO_2	SnO_2-MgO	SnO_2	SnO_2-MgO
J_{sc} (mAcm^{-2})	17.1	15.7	2.72	5.28
V_{oc} (V)	0.45	0.67	0.28	0.57
FF	0.47	0.61	0.42	0.48
η (%)	3.65	6.40	0.33	1.40

Table 7.1: Summary of the photovoltaic parameters resulting from the JV curves from figure 7.1.

to either a CB shift or to reduced recombination at the SnO_2/hole transporter interface.[2, 4, 5, 6, 9, 10, 11, 12, 13]

7.2.2 Electronic characteristics

To further elucidate the role of this layer in the devices, small perturbation transient photocurrent and photovoltage measurements were performed to extract information about the transport and recombination characteristics. In figure 7.3 these parameters are shown for DSCs incorporating the MgO coating and bare devices, plotted against charge density. All measurements are taken under a background illumination from white light diodes with a range of light intensities ranging from an equivalent 100mWcm^{-2} solar illumination to 2.5 mWcm^{-2}. The transport lifetimes at short-circuit conditions for the devices with and without the MgO coating are overlapping at most points studied in the electrolyte cells, as shown in figure 7.3.a. For the solid-state cells, although slightly different, the transport lifetimes are close at

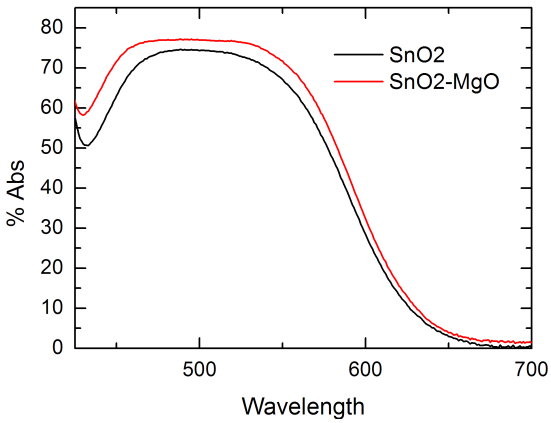

Figure 7.2: Absorption spectrum against wavelength for the films used in the solid-state devices incorporating a thin MgO layer (SnO_2-MgO, red line) and films without a surface treatment (SnO_2, black line)

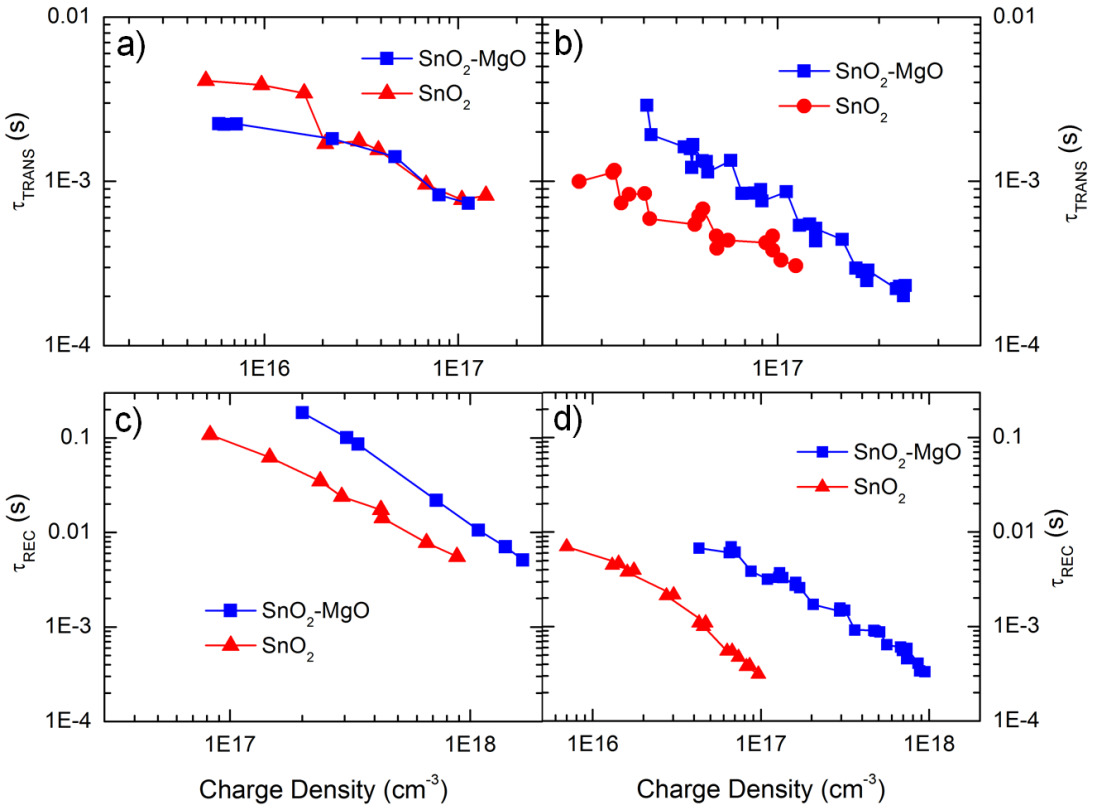

Figure 7.3: a) and b) are the transport lifetimes (τ_{TRANS}) extracted at short-circuit conditions and b) and d) are the recombination lifetimes (τ_{REC}) extracted at open-circuit conditions, plotted against charge density for devices incorporating a thin MgO layer (SnO_2-MgO, ■) and devices with no surface treatment (SnO_2, ▲). a) and c) correspond to devices fabricated with a liquid electrolyte and b) and d) to devices fabricated with a solid-state hole transporter.

high illumination conditions indicating that the MgO treatment has had little influence on the transport limiting trap sites. The charge collection rate in the solid-state cells is a few times faster than the electrolyte cells, presumably due to the thinner films employed (2 versus 8 μm).

Concerning the electron recombination lifetimes, there appears to be an upward shift to longer times in the curves of recombination lifetime versus charge density, i.e. the MgO treated cells have slower recombination under the same charge density conditions. For liquid electrolyte devices, the change is small at just about twice the recombination lifetime at the same charge density, whereas the trend for the solid-state cells is much more pronounced, where a change of almost an order of magnitude is observed. This suggests that the MgO layer is passivating the surface states, or presenting a physical barrier inhibiting recombination.[14] It is likely that the MgO is passivating recombination sites, since this method for deposition only results in what appears to be a monolayer coating of MgO upon the SnO_2 surface.[8] Although the reduction in the recombination lifetime is significant (2 fold for electrolyte and 10 fold for solid-state DSCs) it is not enough to explain the 200 to 300 mV shift of the open-circuit potential. Over 100 fold increase in the recombination lifetime would be required to induce such a shift in open-circuit voltage.[15] If the total increase in open-circuit voltage cannot be accounted for by inhibited recombination, then it is possible that the addition of the MgO interlayer results in a shift in the surface potential of the oxide. Indeed, such a shift has been postulated before for both SnO_2 and ZnO coated with MgO or Al2O3.[1, 16] To probe this transient photovoltage and charge collection measurements were performed to extract a differential capacitance as a function of open-circuit voltage. This capacitance-voltage data is presented in Figure 7.4, and is representative of the location and shape of the tail of the density of sub-band-gap states in the metal oxide with respect to the electrolyte/hole-transporter redox potential. For both the electrolyte and solid-state cells there is a clear positive shift in the position of the "density-of-states" (DOS) of around 200 mV. This result, in addition to the reduction of electron-hole recombination of about 2 fold for the electrolyte and an order of magnitude for the solid-state cells, entirely accounts for the relative shift in open-circuit voltage observed in the JV curves of the solar cells presented in figure 7.1.

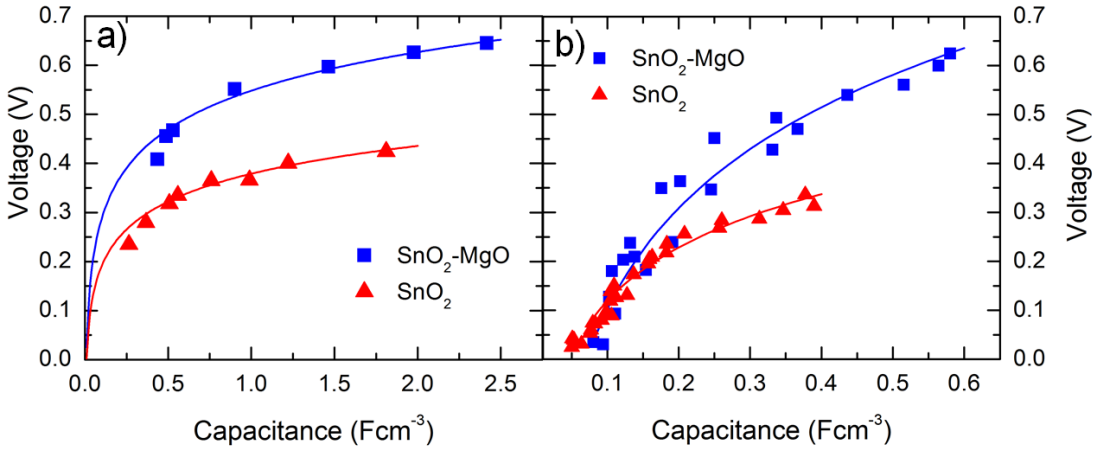

Figure 7.4: Voltage against capacitance plot of devices incorporating a thin MgO layer (SnO_2-MgO, ■) and devices without a surface treatment (SnO_2, ▲). a) corresponds to liquid electrolyte based devices and b) to devices fabricated with a solid-state hole transporter. Solid lines correspond to exponential fits of the experimental data which were used to calculate the charge density of figures 7.3.a and b.

To check whether the shift in short-circuit current for solid-state devices is due to poor charge collection efficiencies, recombination lifetime at short-circuit was estimated as a function of light intensity (in galvanostatic mode, or constant current transient photovoltage decay). In combination with the results from figure 7.3.a and b, the charge collection efficiencies for both electrolyte and solid-state devices was calculated, as shown in figure 7.5. With the MgO interlayer, the solid-state cells exhibit a charge collection efficiency of over 85%, however this drops to as low as 60% for the bare devices at full solar light intensity conditions. Coupled with a slight reduction in dye loading, this quantitatively accounts for the reduction in short circuit current for the bare solid-state cells. In the case of liquid-electrolyte based devices, figure 7.5.a), the charge collection efficiencies for both devices incorporating the MgO interlayer and bare mesostructures are remarkably similar, at over 95% for the whole range studied. This is in contradiction to most literature on this subject where usually bare devices incur extreme recombination losses which lead to poor charge collection efficiencies, completely limiting the device performance to under 1% power conversion efficiencies. For the liquid electrolyte devices fabricated in this study, the main role of the thin MgO

layer is that of a surface potential shift toward vacuum. The fact that recombination characteristics only vary by a factor of two for both treated and untreated cells is particularly important to the viability of using SnO_2 as the mesoporous metal oxide for low band-gap dyes. Comparing the overall recombination rate for the electrolyte based cells to the solid-state cells, as shown in Figure 7.3, is helpful to understand why a much stronger inhibition to recombination is observed for the solid-state cells upon MgO treatment. For the bare devices under a similar charge density of 10^{17} cm^{-3}, the recombination for the electrolyte cells is 300 fold slower than the solid-state cells, and for the SnO_2-MgO devices under a charge density of 10^{18} cm^{-3} the electrolyte cells are 30 fold slower. The characteristic slow recombination in the iodide/triiodide system is due to specific nature of the multistep charge generation and recombination mechanism. This exceptionally slow reaction appears to be the rate determining process, rather than changes to the metal oxide surface.

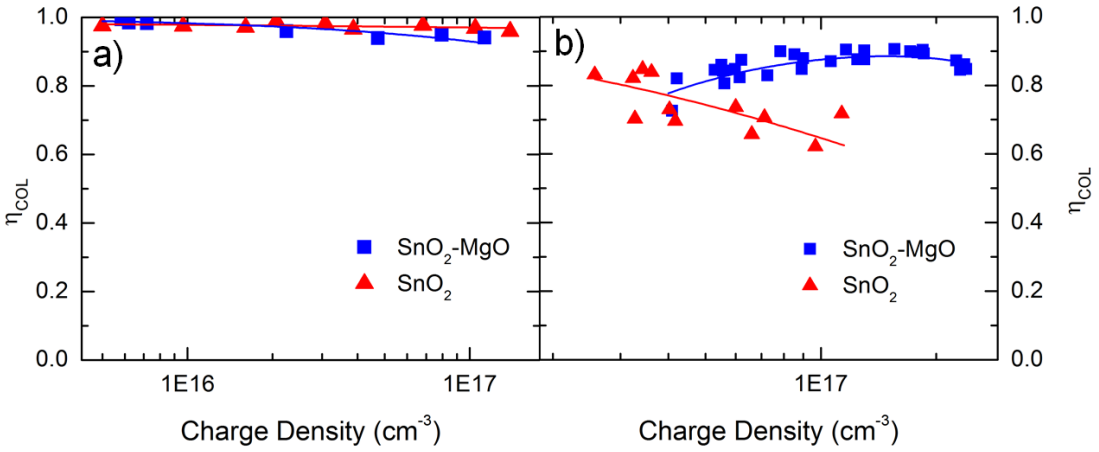

Figure 7.5: Charge collection efficiencies (η_{COL}) against charge density for electrolyte cells (a) and solid-state solar cells (b), for devices incorporating a thin MgO layer (SnO_2-MgO, ■) and devices without a surface treatment (SnO_2, ▲). The lines are the result of interpolating the experimental data.

7.2.3 Terahertz spectroscopy

Almost all the results can be explained by the influence of the MgO treatment upon recombination and surface potential. However, the anomaly of higher

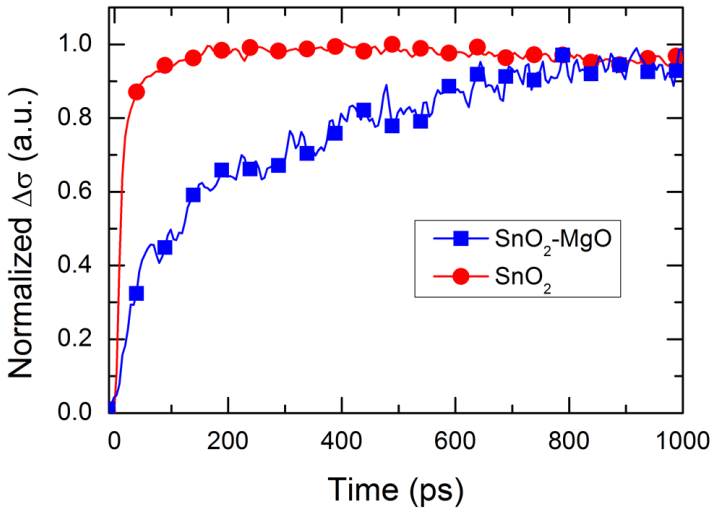

Figure 7.6: Photoconductivity dynamics measured in mesoporous SnO_2 sensitized with Z907 dye, wit (■) and without (▲) MgO treatment, using optical-pump terahertz-probe (OPTP) spectroscopy. Photoexcitation was carried out with 550 nm wavelength 90 fs pulses with 7 x 10^{14} photons cm^{-2} fluence. The curves have been normalized at their respective maxima, for trend comparison. I acknowledge that Priti Tiwana collected and analyzed all the data presented in this figure.

photocurrent observed in the bare electrolyte cells still requires explanation. This has been observed every time, with a number of different SnO_2 pastes over tens of experiments. To probe possible changes to charge generation time-resolved terahertz-pump optical-probe photoconductivity spectroscopy was employed. The samples studied are dye-sensitized mesoporous SnO_2 in vacuum where Z907 is used as the sensitizer. There is no electrolyte or hole-transporter present in order to purely probe the electron transfer phenomena. Z907 was used as the sensitizer here since D102 gave very little signal in the THz set up, possibly due to the requirement for the presence of a polar medium to operate effectively.[17] As the THz radiation passes through the sample it accelerates mobile charge carriers and is hence attenuated. The magnitude of the change in transmission of the THz pulse following photoexcitation of the system is proportional to the photoinduced change in conductivity ($\Delta\sigma$) and hence representative of the number of free carriers injected into the SnO_2 conduction band ($\Delta\sigma = e\Delta n\mu$) were e is the charge of an electron, Δn is photoinjected electron

density and μ is its mobility).

In figure 7.6 the normalized transient photoconductivity signal is shown. Complete charge injection in SnO_2 sensitized with Z907 takes place within the first few hundred picoseconds, slightly slower than TiO_2 though still fast.[18] However, in case of MgO treated SnO_2, charge injection is significantly slower and still not complete within the nanosecond measurement window. As will be discussed elsewhere,[19] there is a light-soaking effect in sensitized SnO_2 films, both with and without MgO treatment, where injection and photocurrent improve during illumination. The data presented in figure 7.6 corresponds to the final steady-state value in both cases. The absolute photoconductivity values cannot be directly compared with each other, due to sample-to-sample variation, however the general trend observed is that higher photoconductivity values at 1ns are observed for bare devices. The time-resolved photo conductivity measurements are consistent with faster and more efficient electron transfer in the bare dye-sensitized systems. The slower injection in the dye-sensitized SnO_2-MgO films is consistent with poorer electron transfer and at this rate of hundreds of ps to ns, it would be expected that the injection does not compete entirely favorably with non-radiative decay channels. Hence this spectroscopy is entirely consistent with the slightly higher short-circuit photocurrent for the bare SnO_2 liquid electrolyte cells.

7.3 Conclusions

The role of a thin MgO layer, chemically deposited over mesoporous SnO_2 structures in liquid electrolyte and solid-state dye-sensitized solar cells has been investigated. The treatment has 4 significant influences upon the optical and electronic characteristics of the solar cells, and these effects have differing levels of importance for either solid-state or liquid electrolyte based solar cells:

- There is approximately a 200mV positive shift in the conduction band edge which is the predominant factor increasing the open-circuit voltage in both cells.

- There is an increase in the electron lifetime by approximately 2 fold for elec-

trolyte and 10 fold for solid-state cells. This has only a small influence on the electrolyte cells, though significantly contributes to further increased open-circuit voltage and increased photocurrent (charge collection efficiency) for the solid-state cells.

- There is a reduction in the electron injection rate and efficiency which results in a marginal drop in photocurrent for the electrolyte cells upon MgO treatment. Notably for the solid-state cells, the possibility of reductive quenching of the excited dye (where hole transfer can occur prior to electron transfer) may contribute to making this aspect of lower importance.
- There is a marginal increase in the dye loading upon MgO treatment, which will contribute slightly to increasing the photocurrent in the solid-state cells, but will have negligible influence upon the thicker electrolyte cells.

These clear finding ascertains the viability of using SnO_2 electrodes for DSCs and indicate that careful choice and control of the surface coating could result in competitive electrodes for DSCs and open new possibilities for low band gap dyes and stability.

References

[1] Chaiya Prasittichai and Joseph T. Hupp. Surface modification of sno2 photoelectrodes in dye-sensitized solar cells: Significant improvements in photovoltage via al2o3 atomic layer deposition. *The Journal of Physical Chemistry Letters*, 1(10):1611–1615, 2010. 106, 111

[2] E. Palomares, J. N. Clifford, S. A. Haque, T. Lutz, and J. R. Durrant. Control of charge recombination dynamics in dye sensitized solar cells by the use of conformally deposited metal oxide blocking layers. *Journal of the American Chemical Society*, 125(2):475–482, 2003. 106, 109

[3] H. Park, D. J. Yang, J. S. Yoo, K. S. Mun, W. R. Kim, H. G. Kim, and W. Y. Choi. Surface passivation of highly ordered TiO_2 nanotube arrays and application to dye-sensitized solar cells using the concept of isoelectric point. *Journal of the Ceramic Society of Japan*, 117(1365):596–599, 2009. 106, 108

[4] A. Kay and M. Gratzel. Dye-sensitized core-shell nanocrystals: Improved efficiency of mesoporous tin oxide electrodes coated with a thin layer of an insulating oxide. *Chemistry of Materials*, 14(7):2930–2935, 2002. 106, 108, 109

[5] M. K. I. Senevirathna, Pkddp Pitigala, E. V. A. Premalal, K. Tennakone, G. R. A. Kumara, and A. Konno. Stability of the SnO_2/mgo dye-sensitized photo electrochemical solar cell. *Solar Energy Materials and Solar Cells*, 91(6):544–547, 2007. 106, 109

[6] K. Tennakone, J. Bandara, P. K. M. Bandaranayake, G. R. A. Kumara, and A. Konno. Enhanced efficiency of a dye-sensitized solar cell made from mgo-coated nanocrystalline SnO_2. *Japanese Journal of Applied Physics Part 2-Letters*, 40(7B):L732–L734, 2001. 106, 109

[7] H. J. Snaith. Estimating the maximum attainable efficiency in dye-sensitized solar cells. *Advanced Functional Materials*, 20(1):13–19, 2010. 107

[8] H. J. Snaith and C. Ducati. SnO_2-based dye-sensitized hybrid solar cells exhibiting near unity absorbed photon-to-electron conversion efficiency. *Nano Letters*, 10(4):1259–1265, 2010. 107, 111

[9] J. Bandara and U. W. Pradeep. Tuning of the flat-band potentials of nanocrystalline TiO_2 and SnO_2 particles with an outer-shell mgo layer. *Thin Solid Films*, 517(2):952–956, 2008. 109

[10] A. N. M. Green, E. Palomares, S. A. Haque, J. M. Kroon, and J. R. Durrant. Charge transport versus recombination in dye-sensitized solar cells employing nanocrystalline TiO_2 and SnO_2 films. *Journal of Physical Chemistry B*, 109(25):12525–12533, 2005. 109

[11] H. S. Jung, J. K. Lee, M. Nastasi, S. W. Lee, J. Y. Kim, J. S. Park, K. S. Hong, and H. Shin. Preparation of nanoporous mgo-coated TiO_2 nanoparticles and their application to the electrode of dye-sensitized solar cells. *Langmuir*, 21(23):10332–10335, 2005. 109

[12] H. Park, D. J. Yang, H. G. Kim, S. J. Cho, S. C. Yang, H. Lee, and W. Y. Choi. Fabrication of mgo-coated TiO_2 nanotubes and application to dye-sensitized solar cells. *Journal of Electroceramics*, 23(2-4):146–149, 2009. 109

[13] S. Wu, H. W. Han, Q. D. Tai, J. Zhang, S. Xu, C. H. Zhou, Y. Yang, H. Hu, B. L. Chen, B. Sebo, and X. Z. Zhao. Enhancement in dye-sensitized solar cells based on mgo-coated TiO_2 electrodes by reactive dc magnetron sputtering. *Nanotechnology*, 19(21), 2008. 109

[14] Francisco Fabregat-Santiago, Jorge Garcia-Canadas, Emilio Palomares, John N. Clifford, Saif A. Haque, James R. Durrant, Germa Garcia-Belmonte, and Juan Bisquert. The origin of slow electron recombination processes in dye-sensitized solar cells with alumina barrier coatings. *Journal of Applied Physics*, 96(11):6903–6907, 2004. 111

[15] H. J. Snaith, L. Schmidt-Mende, M. Gratzel, and M. Chiesa. Light intensity, temperature, and thickness dependence of the open-circuit voltage in solid-state dye-sensitized solar cells. *Physical Review B*, 74(4), 2006. 111

[16] D.C. Olson, S.E. Shaheen, M.S. White, W.J. Mitchell, M.F.A.M. van Hest, R.T. Collins, and D.S. Ginley. Band-offset engineering for enhanced open-circuit voltage in polymeroxide hybrid solar cells. *Advanced Functional Materials*, 17(2):264–269, 2007. 111

[17] Agnese Abrusci, I. Kang Ding, Mohammed Al-Hashimi, Tamar Segal-Peretz, Michael D. McGehee, Martin Heeney, Gitti L. Frey, and Henry J. Snaith. Facile infiltration of semiconducting polymer into mesoporous electrodes for hybrid solar cells. *Energy & Environmental Science*, 4(8):3051–3058, 2011. 114

[18] Priti Tiwana, Pablo Docampo, Michael B. Johnston, Henry J. Snaith, and Laura M. Herz. Electron mobility and injection dynamics in mesoporous ZnO, SnO_2, and TiO_2 films used in dye-sensitized solar cells. *ACS Nano*, 5(6):5158–5166, 2011. doi: 10.1021/nn201243y. 115

[19] Priti Tiwana, Pablo Docampo, Michael B. Johnston, Laura M. Herz, and H. J. Snaith. Improved device performance in SnO_2 dye sensitized solar cells with exposure to light. [Submitted]. 115

Chapter 8

Limits to the electron transport in mesoporous TiO_2 photoanodes

8.1 Introduction

Although progress has been made in the last few years, the factors limiting the charge collection length in solid-state dye-sensitized solar cells have not been solved. While most literature link inefficient pore filling to this limitation, I have shown in chapter 6 that this is unlikely to be the case. In order to increase the charge collection efficiencies in the devices, the charge recombination lifetime must be extended or the diffusion coefficient of the films must be increased or both. In chapter 7, I have studied the effects of a thin MgO layer on SnO_2 based devices and observed that this treatment extends the electron lifetimes by an order of magnitude. However, this is accompanied by a reduction in the charge generation efficiency when applied to TiO_2. This effect is not unique to MgO, other insulating metal oxides such as Al_2O_3 have been extensively used in other research publications and a similar trade-off between current and voltage is generally observed. For this reason, the use of insulating metal oxide coatings, while extending the charge collection length, is unlikely to lead to com-

petitive power conversion efficiencies and therefore a different solution must be sought. The other aspect limiting the diffusion length is the transport through thenanocrystaline structure. Charge transport in DSCs based on nanocrystalline TiO_2 appears to be electron-limited,[1, 2, 3] so a good starting point is to change the mesoporous metal oxide to another one with faster electron mobility in order to check if this parameter is limiting the device performance. This is in principle feasible since only free charges, i.e. charges in the conduction band, can move freely through the films. Typical materials with faster electron mobilities and suitable energy levels for the conduction and valence band that have been amply used for DSCs are ZnO[4, 5, 6] and SnO_2[7, 8]. The bulk mobility for these two materials is around 200 $cm^2V^{-1}s^{-1}$ [9, 10] which is more than a full order of magnitude above TiO_2[11]. However, the electron transport dynamics are very similar for the three systems.[12, 13, 14] In fact, changes to the diffusion coefficient are usually correlated to changes in the crystal size of the mesoporous oxide used,[14, 15, 16, 17, 18, 19] where even photoanodes with very different morphologies, such as one dimensional nanotubes compared to typical nanoparticle based photoanodes, still show similar diffusion coefficients due to their similar crystal size.[20, 21] This suggests that the trapping/detrapping mechanism is dominating the transport characteristics of solar cells fabricated from nanocrystalline materials. In order to make improvements to charge transport, the characteristics of transport-limiting traps must be studied in further detail.

8.2 Results and discussion

8.2.1 Transport-limiting traps

The electron transport in mesoporous, nanocrystalline photoanodes is generally described by a charge multiple-trapping model.[22, 23] First, electrons are transferred into the mesoporous oxide where they become trapped at sub bandgap states. Then, they are thermally released into the conduction band, where they are free to move until they become trapped again. In this way, transport is governed by detrapping times, which become longer for the deeper traps.[24, 25, 26, 27] The conductivity of the films, and hence charge transport, depends strongly

on the occupancy of electrons in the conduction band (n_{FREE}), which in turn is determined by the quasi Fermi level (E_F) of the electrons in the film. The occupancy of the conduction band can be calculated from the Fermi-Dirac distribution (F_A). If an exponential distribution of sub bandgap states is assumed, then:

$$F_A = \frac{1}{1 + e^{\frac{E - E_F}{kT}}} \tag{8.1}$$

$$n_{TRAP} = N_A F_A \tag{8.2}$$

$$n_{FREE} = N_{CB} e^{\frac{E_F - E_{CB}}{kT}} \tag{8.3}$$

The free electron charge density (n_{FREE}) will depend upon the trapped charge density (n_{TRAP}), the effective density of conduction band states (N_{CB}) and the trap density (N_A) in the film as $n^{\alpha}_{FREE} = \frac{N_A}{N^{\alpha}_{CB}} n_{TRAP}$.[27] Clearly, if the trap density is reduced then an increase in the free electron density at the same quasi Fermi level should follow, and hence faster transport should be achieved. For these reasons it is important to understand the nature and location of the trap states, as they will be critical in determining the charge transport characteristics of the material.

Kopidakis *et al.* have studied the spatial location of traps in a system where the particle size was varied while keeping the porosity constant, leading to a range of films with very different available surface areas.[16] By estimating the number of traps and comparing them to the surface area of the film, they found that the trap density scales up with the surface area. However, since the size of the particles was changed, the internal surface area between the particle grains was also changed due to the synthesis method utilized. An argument was put forward then that if the number of traps is proportional to the intergrain boundaries, a dependence on transport proportional to the number of particles in the film should be found.[16] This is not clear since the intergrain contact area must also change according to the size of the particle, and hence, a similar dependence with exposed surface area would be expected.

It is very challenging to disentangle the change in exposed surface area with

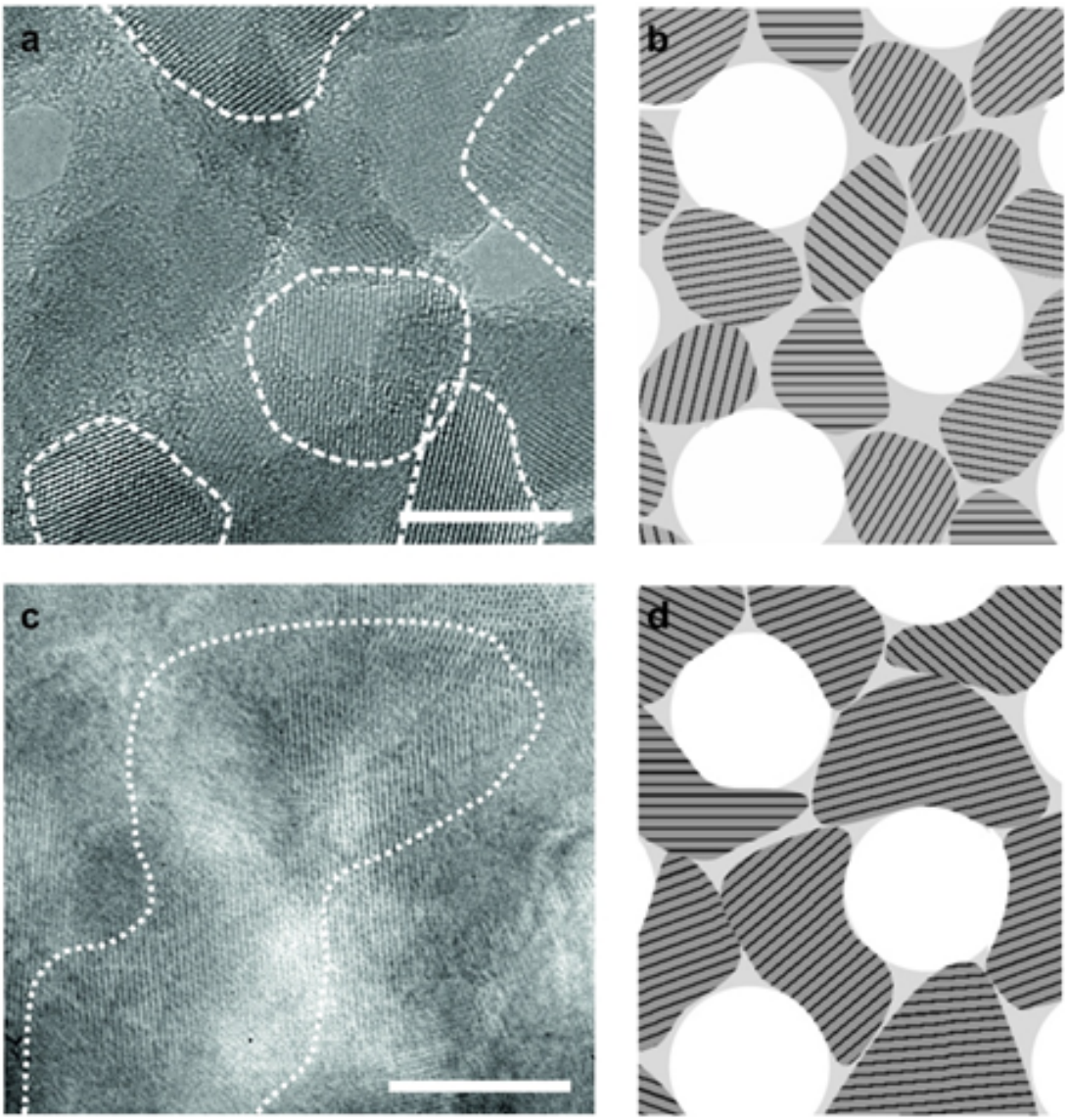

Figure 8.1: Assembly of nanocrystals within the mesoporous TiO_2 network. Left: High resolution transmission electron microscopy images (HRTEM) of samples crystallized at 450°C (a) and 650°C (c). For guidance, white dotted lines are superimposed to visualize the individual crystallites. Right: Schematic of the observed crystallite assembly at 450°C (b) and 650°C (d). Samples calcined at temperatures between 400°C and 500°C exhibit randomly distributed crystals that are significantly smaller than the length scale of the porous template. For samples calcined at 650°C and beyond, the crystal size exceeds the length scale of the BCP-dictated confinement, resulting in anisotropic growth within the network. I acknowledge that the images presented in this figure were collected by Stefan Guldin in the University of Cambridge.

changes in interparticle contact area by using conventional colloidally synthesized nanocrystalline electrodes. When the TiO_2 nanoparticles are synthesized, they must be reconstituted into a paste with some kind of binder. Subsequent calcination and sintering of the films at temperatures above 400°C results in a TiO_2 network where the porosity arises from the packing of the constituent nanoparticles. For this reason, the morphology is always random and the surface area is governed by the particle size. The structure formation process of block copolymer-directed inorganic films is fundamentally different and has recently led to promising results when used as photoanodes in ss-DSCs.[28, 29] This route makes precise morphology and crystallinity control possible.

In practice, by using this system, the surface area of the film can be tuned by the ratio between the block copolymer and the inorganic sol introduced. The calcination temperature then sets the particle size of the films, with minimal changes to the exposed surface area, making this the ideal system to study the effects of grain boundaries on the transport properties of the solid-state dye-sensitized solar cell.

The films used in this chapter were assembled with the diblock copolymer poly(isoprene-*b*-ethylene oxide) (PI-PEO). In a typical synthesis, PI-PEO is dissolved in tetrahydrofouran (THF) and then the titania sol from mixing Titanium ethoxide with hydrochloric acid is added. The solution is then cast in a petri dish, where the solvent is allowed to slowly evaporate at 50°C. After all the solvent has been evaporated, the mixture is recovered and redissolved in an azeotrope solvent mixture of 1-butanol and toluene. This solution is finally spincoated onto the substrate samples, which are then calcined at a range of temperatures. In figure 8.1.a) and b) high resolution TEM images of the formed structure for substrates annealed at 400°C and 600°C are shown. The different crystal sizes can be clearly observed. Further characterization was performed via XRD.[28]

8.2.2 Density of states distribution

Changes to the surface properties of the photoanodes are usually reflected in the density of sub-bandgap states of the material, since these states are usually linked to surface related defects, including oxygen vacancies.[19, 30] Here, although the

different calcination temperatures result in very different crystal sizes, a big shift in the sub band-gap states is not expected, since the available surface area of the films has been kept relatively constant for all the temperatures studied as well as the crystallization environment.

In order to study the DOS of the films, the solar cells were measured through transient photovoltage and photocurrent decay measurements. By doing these two measurements at either open or short circuit, the capacitance of the system can be directly measured. A plot of this quantity against bias is shown in figure 8.2. For higher biases, there are barely any differences between the different photoanodes. This is expected, since the surface area for these materials is very similar, and the crystallization environment, which can have a big effect in this distribution, [30] was the same for all samples. At lower biases, however, a small but consistent shift towards fewer available states as the temperature is increased can be observed. The curve corresponding to 700°C clearly shows less available sub bandgap states at all measured potentials, consistent with the reduced surface area of the film.

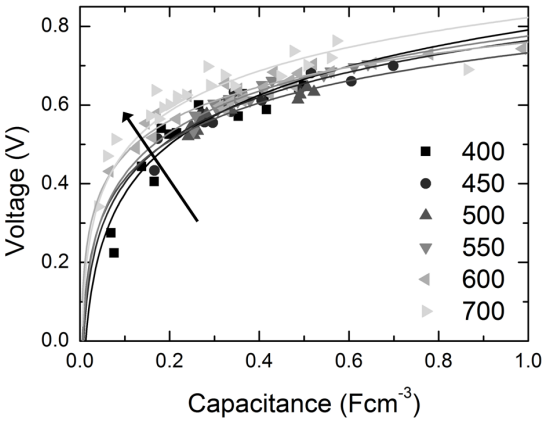

Figure 8.2: Voltage against capacitance plot for photoanodes which were subjected to a range of calcination temperatures (see legend)

8.2.3 Transport and recombination kinetics

From the photovoltage decay measurements and integrating the DOS from figure 8.2, the recombination lifetime and its dependence with charge density can be extracted. The results are shown in figure 8.3.a). In this instance, no systematic trend is observed with temperature, where all the points are roughly on the same line. This is again consistent with the similar surface areas of the films, since recombination probably occurs through these surface states.[31]

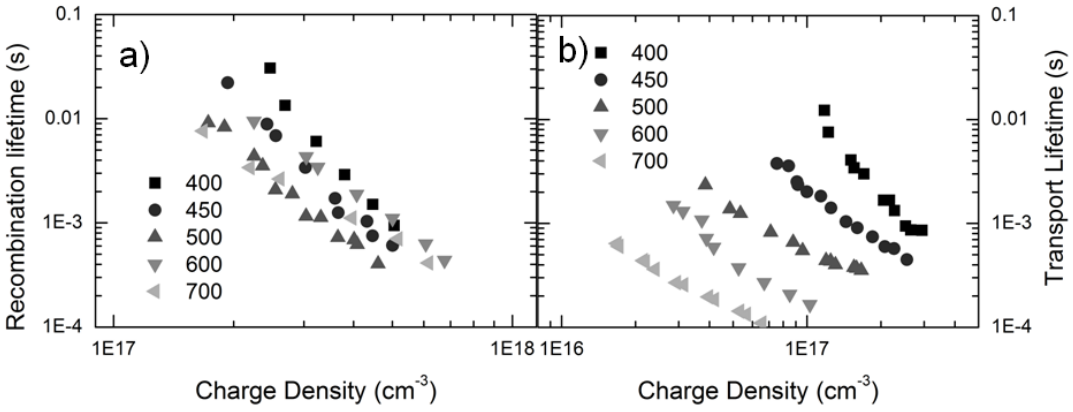

Figure 8.3: Photovoltage decay (a) and photocurrent decay (b) against charge density plots for photoanodes which were subjected to a range of calcination temperatures (see legend).

In order to probe the transport of the films, the charge density at short circuit conditions was calculated iteratively as explained in section 3.6.1.2. The results are plotted in figure 8.3. b), where a very clear trend can be seen where films calcined at higher temperatures achieve over an order of magnitude faster transport at lower charge densities. In fact, the calculated diffusion coefficient at 100 mWcm^{-2} AM1.5 illuminating conditions is 5.7 10^{-6} cm^{2}s^{-1} for films calcined at 400°C, and 4.19 10^{-5} cm^{2}s^{-1} for films calcined at 700°C. This is consistent with a reduction of transport limiting traps located at the grain boundaries. In fact, if transport at constant charge density ($\sim 10^{17}$ cm^{-3}) is compared, the difference is over 3 orders of magnitude.

A similar analysis to the one performed by Kopidakis *et al.*[16] can be effectuated by plotting the charge density of the films against their short circuit current, as shown in figure 8.4.a). The curves can then be fit as: $n = N_{TOT} C_2 J_{SC}^{\alpha}$, where N_{TOT} is the number of traps, without any assumptions on their distribution, and C_2 is a particle independent constant according to Kopidakis *et al.* The fitted logarithm of $C_2 N_{TOT}$ was then plotted against the logarithm of the average particle diameter, as shown in figure 8.4.b). If the traps are situated at the intergrain boundaries, Kopidakis *et al.* would expect them to scale with the number of particles in the film [32]. This is indeed the case in this system, although the reasoning seems suspect since a dependency with the number of particles in the

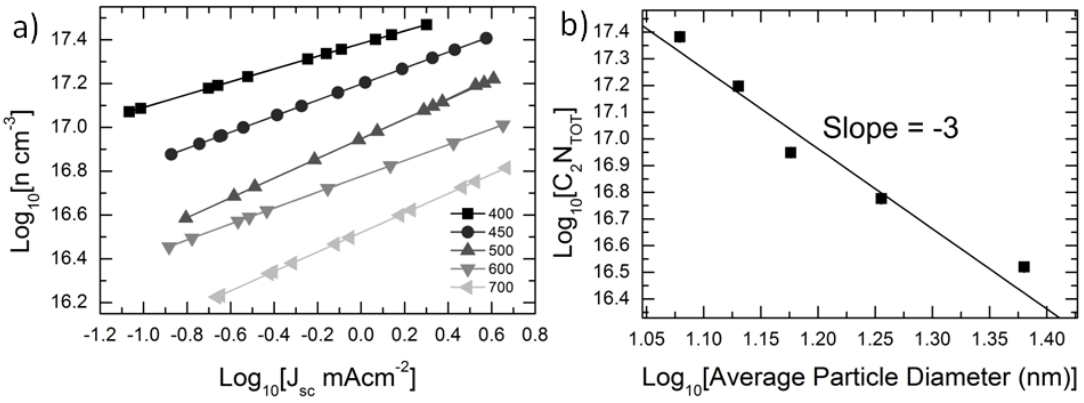

Figure 8.4: Log - Log lot of charge density against short circuit current (a) for photoanodes which were subjected to a range of calcination temperatures (see legend). The lines correspond to fits of the data where $n = N_{TOT}C_2J_{SC}^{\alpha}$. The resulting fits are plotted against the average particle diameter of the films in (b). The line corresponds to the expected slope of -3.

film does not equal a dependency with the intergrain surface area.

This result seems to be in direct opposition to the one found by Kopidakis *et al.*, where after doing the analysis detailed in the previous paragraph, the number of traps was found to scale with the roughness of the film, rather than with the number of particles in the film. These contradictory results may be explained if the lower charge density of the films forming the solid-state dye-sensitized solar cell system is considered. In the case of the films studied in this chapter, for particles of similar size (∼20nm) in comparison with the ones in Kopidakis' study, almost a full order of magnitude difference in charge density at similar full sun conditions was found. This would have the consequence that the solid-state system is much more sensitive to deep traps within the system. There is some evidence that suggests that traps arising from inter-grain boundaries have very deep energies, i.e. away from vacuum,[33] and due to the lower charge density of the solid-state films, they might not be filled. Furthermore, the model employed limits the factors affecting the transport of electrons to the films to just traps. It is entirely possible that other interactions are present, such as potential barriers due to charge trapped at the intergrain boundary.[14, 34, 35, 36] Further work is necessary to develop a new model that takes different charge interactions into

account.

While the particular mechanism of charge transport through the film is unclear, it is overwhelmingly evident that reducing the number of intergrain boundaries has a positive effect in this parameter. This clearly suggests that to achieve thick films which can be used in conjunction with panchromatic absorbers, films with high enough surface area and reduced grain boundaries must be used. Further evidence that this is the case was presented in a recent study by Xu *et al.*,[37] where ~10 μm thick single crystalline wires were sequentially grown on the same substrate to a maximum thickness of 50 μm, resulting in a structure where from top to bottom, only 4 intergrain boundaries can be found. This system achieves an astounding 5.65% power conversion efficiency, with a high fill factor and high short circuit current, conclusively proving that the limits to diffusion length arise from the nanocrystalline nature of the typical photoanodes.

8.3 Conclusions

Factors limiting the diffusion of electrons through mesoporous TiO_2 films were examined through block copolymer assembled films. Here, the inorganic morphology is confined by the organic macromolecule, leading to films where by subjecting the photoanodes to different calcination temperatures, the exposed surface area is kept almost constant, but a range of crystal sizes is achieved. This system is ideal to study the effects of interparticle boundaries on transport. It is found that by increasing the size of the particles and reducing the intergrain boundaries, at least an order of magnitude faster transport can be achieved and up to 3 orders of magnitude if compared at the same film charge density. However, the analysis performed on the results does not perfectly match the results found by Kopidakis *et al.* In fact, the result found in this chapter is in direct opposition to the one found by the aforementioned authors. Although differences in charge density are present which could potentially affect the interaction with the trap states, it is my opinion that the model previously employed does not correctly reflect the transport in the films. Further work is thus necessary to develop a model that correctly incorporates the effects of the intergrain boundaries on the transport of electrons through the films.

References

[1] Henry J Snaith and Michael Gratzel. Electron and hole transport through mesoporous TiO_2 infiltrated with spiro-ometad. *Adv. Mater.*, 19:3643–3647, 2007. 121

[2] Anneke Hauch and Andreas Georg. Diffusion in the electrolyte and charge-transfer reaction at the platinum electrode in dye-sensitized solar cells. *Electrochimica Acta*, 46(22):3457–3466, 2001. 121

[3] Nikos Kopidakis, Kurt D. Benkstein, Jao van de Lagemaat, and Arthur J. Frank. Transport-limited recombination of photocarriers in dye-sensitized nanocrystalline tio2 solar cells. *The Journal of Physical Chemistry B*, 107(41):11307–11315, 2003. doi: 10.1021/jp0304475. 121

[4] Idriss Bedja, Prashant V. Kamat, Xiao Hua, A. G. Lappin, and Surat Hotchandani. Photosensitization of nanocrystalline ZnO films by bis(2,2'-bipyridine)(2,2;-bipyridine-4,4'-dicarboxylic acid)ruthenium(ii). *Langmuir*, 13(8):2398–2403, 1997. 121

[5] Karin Keis, Eva Magnusson, Henrik Lindstrom, Sten-Eric Lindquist, and Anders Hagfeldt. A 5% efficient photoelectrochemical solar cell based on nanostructured ZnO electrodes. *Solar Energy Materials and Solar Cells*, 73(1):51 – 58, 2002. 121

[6] Nafiseh Memarian, Isabella Concina, Antonio Braga, Seyed Mohammad Rozati, Alberto Vomiero, and Giorgio Sberveglieri. Hierarchically assembled ZnO nanocrystallites for high-efficiency dye-sensitized solar cells. *Angewandte Chemie International Edition*, 50(51):12321–12325, 2011. 121

[7] A. Kay and M. Gratzel. Dye-sensitized core-shell nanocrystals: Improved efficiency of mesoporous tin oxide electrodes coated with a thin layer of an insulating oxide. *Chemistry of Materials*, 14(7):2930–2935, 2002. 121

[8] K. Tennakone, J. Bandara, P. K. M. Bandaranayake, G. R. A. Kumara, and A. Konno. Enhanced efficiency of a dye-sensitized solar cell made from

mgo-coated nanocrystalline SnO_2. *Japanese Journal of Applied Physics Part 2-Letters*, 40(7B):L732–L734, 2001. 121

[9] D.C. Look, D.C. Reynolds, J.R. Sizelove, R.L. Jones, C.W. Litton, G. Cantwell, and W.C. Harsch. Electrical properties of bulk ZnO. *Solid State Communications*, 105(6):399 – 401, 1998. 121

[10] Masahiro Nagasawa, Shigeo Shionoya, and Shoji Makishima. Vapor reaction growth of sno_2 single crystals and their properties. *Japanese Journal of Applied Physics*, 4(3):195–202, 1965. 121

[11] L. Forro, O. Chauvet, D. Emin, L. Zuppiroli, H. Berger, and F. Levy. High mobility n-type charge carriers in large single crystals of anatase (TiO_2). *Journal of Applied Physics*, 75(1):633–635, 1994. 121

[12] Richard L. Willis, Carol Olson, Brian O'Regan, Thierry Lutz, Jenny Nelson, and James R. Durrant. Electron dynamics in nanocrystalline zno and tio2 films probed by potential step chronoamperometry and transient absorption spectroscopy. *The Journal of Physical Chemistry B*, 106(31):7605–7613, 2002. doi: 10.1021/jp020231n. 121

[13] Yosuke Fukai, Yusuke Kondo, Shogo Mori, and Eiji Suzuki. Highly efficient dye-sensitized SnO_2 solar cells having sufficient electron diffusion length. *Electrochemistry Communications*, 9(7):1439–1443, 2007. 121

[14] Maria Quintana, Tomas Edvinsson, Anders Hagfeldt, and Gerrit Boschloo. Comparison of dye-sensitized zno and tio2 solar cells: studies of charge transport and carrier lifetime. *The Journal of Physical Chemistry C*, 111(2):1035–1041, 2006. doi: 10.1021/jp065948f. 121, 127

[15] Kang-Le Li, Zhi-Bin Xie, and Stefan Adams. Fast charge transport of titania nanotube arrays in dye-sensitized solar cells. *Zeitschrift fr Kristallographie*, 225(05):173–179, 2010. doi: 10.1524/zkri.2010.1238. 121

[16] N. Kopidakis, N. R. Neale, K. Zhu, J. van de Lagemaat, and A. J. Frank. Spatial location of transport-limiting traps in TiO_2 nanoparticle films in dye-sensitized solar cells. *Appl. Phys. Lett.*, 87(20), 2005. 121, 122, 126

[17] S. Nakade, M. Matsuda, S. Kambe, Y. Saito, T. Kitamura, T. Sakata, Y. Wada, H. Mori, and S. Yanagida. Dependence of tio2 nanoparticle preparation methods and annealing temperature on the efficiency of dye-sensitized solar cells. *The Journal of Physical Chemistry B*, 106(39):10004–10010, 2002. doi: 10.1021/jp020051d. 121

[18] S. Nakade, Y. Saito, W. Kubo, T. Kitamura, Y. Wada, and S. Yanagida. Influence of tio2 nanoparticle size on electron diffusion and recombination in dye-sensitized tio2 solar cells. *The Journal of Physical Chemistry B*, 107(33):8607–8611, 2003. doi: 10.1021/jp034773w. 121

[19] Pablo Docampo, Stefan Guldin, Ullrich Steiner, and H. J. Snaith. Triblock terpolymer directed self-assembly of mesoporous TiO_2 - high performance photoanodes for solid state dye-sensitized solar cells. *Advanced Energy Materials*, Accepted(–):–, 2012. 121, 124

[20] K. Zhu, N. R. Neale, A. Miedaner, and A. J. Frank. Enhanced charge-collection efficiencies and light scattering in dye-sensitized solar cells using oriented tio_2 nanotubes arrays. *Nano Letters*, 7(1):69–74, 2007. 121

[21] Yoshinori Ohsaki, Naruhiko Masaki, Takayuki Kitamura, Yuji Wada, Takumi Okamoto, Toru Sekino, Kohichi Niihara, and Shozo Yanagida. Dye-sensitized TiO_2 nanotube solar cells: fabrication and electronic characterization. *Physical Chemistry Chemical Physics*, 7(24), 2005. 121

[22] Joseph Orenstein and Marc Kastner. Photocurrent transient spectroscopy: Measurement of the density of localized states in $\alpha - As_2Se_3$. *Physical Review Letters*, 46(21):1421–1424, 1981. PRL. 121

[23] T. Tiedje and A. Rose. A physical interpretation of dispersive transport in disordered semiconductors. *Solid State Communications*, 37(1):49–52, 1981. 121

[24] Laurence M. Peter. Dye-sensitized nanocrystalline solar cells. *Phys. Chem. Chem. Phys.*, 9:2630–2642, 2007. 121

[25] Jenny Nelson and Rosemary E. Chandler. Random walk models of charge transfer and transport in dye sensitized systems. *Coordination Chemistry Reviews*, 248(1314):1181 – 1194, 2004. 121

[26] Jenny Nelson. Continuous-time random-walk model of electron transport in nanocrystalline TiO_2 electrodes. *Phys. Rev. B*, 59:15374–15380, Jun 1999. 121

[27] Juan Bisquert and Vyacheslav S. Vikhrenko. Interpretation of the time constants measured by kinetic techniques in nanostructured semiconductor electrodes and dye-sensitized solar cells. *The Journal of Physical Chemistry B*, 108(7):2313–2322, 2004. 121, 122

[28] Stefan Guldin, Sven Huttner, Priti Tiwana, M. Christopher Orilall, Burak Ulgut, Morgan Stefik, Pablo Docampo, Matthias Kolle, Giorgio Divitini, Caterina Ducati, Simon A. T. Redfern, Henry J. Snaith, Ulrich Wiesner, Dominik Eder, and Ullrich Steiner. Improved conductivity in dye-sensitised solar cells through block-copolymer confined TiO_2 crystallisation. *Energy Environ. Sci.*, 4(1):225–233, 2011. 124

[29] Stefan Guldin, Pablo Docampo, Morgan Stefik, Gen Kamita, Ulrich Wiesner, Henry J. Snaith, and Ullrich Steiner. Layer-by-layer formation of block-copolymer-derived TiO_2 for solid-state dye-sensitized solar cells. *Small*, 8(3):432–440, 2012. 124

[30] Pablo Docampo, Stefan Guldin, Morgan Stefik, Priti Tiwana, M. Christopher Orilall, Sven Huttner, Hiroaki Sai, Ulrich Wiesner, Ulrich Steiner, and Henry J. Snaith. Control of solid-state dye-sensitized solar cell performance by block-copolymer-directed TiO_2 synthesis. *Adv. Funct. Mater.*, 20(11):1787 – 1796, 2010. 124, 125

[31] Juan Bisquert, Arie Zaban, and P. Salvador. Analysis of the mechanisms of electron recombination in nanoporous TiO_2 dye-sensitized solar cells. nonequilibrium steady-state statistics and interfacial electron transfer via surface states. *The Journal of Physical Chemistry B*, 106(34):8774–8782, 2002. doi: 10.1021/jp026058c. 125

[32] Jao van de Lagemaat, Kurt D. Benkstein, and Arthur J. Frank. Relation between particle coordination number and porosity in nanoparticle films: implications to dye-sensitized solar cells. *The Journal of Physical Chemistry B*, 105(50):12433–12436, 2001. doi: 10.1021/jp013369z. 126

[33] Thomas Berger, Teresa Lana-Villarreal, Damian Monllor-Satoca, and Roberto Gomez. An electrochemical study on the nature of trap states in nanocrystalline rutile thin films. *The Journal of Physical Chemistry C*, 111(27):9936–9942, 2007. doi: 10.1021/jp071438p. 127

[34] J. W. Orton and M. J. Powell. The hall effect in polycrystalline and powdered semiconductors. *Reports on Progress in Physics*, 43(11):1263, 1980. 127

[35] John Y. W. Seto. The electrical properties of polycrystalline silicon films. *Journal of Applied Physics*, 46(12):5247–5254, 1975. 127

[36] Gerrit Boschloo and Anders Hagfeldt. Activation energy of electron transport in dye-sensitized TiO_2 solar cells. *The Journal of Physical Chemistry B*, 109(24):12093–12098, 2005. 127

[37] Chengkun Xu, Jiamin Wu, Umang V. Desai, and Di Gao. High-efficiency solid-state dye-sensitized solar cells based on TiO_2-coated ZnO nanowire arrays. *Nano Letters*, 2012. 128

Chapter 9

Oxygen-free solid-state dye-sensitized solar cells

9.1 Introduction

Solid-state organic based semiconductors are commercially attractive due to the prospect of low cost solution processing of electronic devices.[1, 2] The efficiency of solar cells incorporating these materials is increasing rapidly and within the near future commercially viable device concepts are expected to be realized.[3, 4, 5] Further to initial efficiency, the solar cells must last for at least 20 years outdoor usage to be a feasible technology for large scale power generation.[6] The combination of oxygen and sunlight is catastrophic for the stability of organic semiconductors.[7, 8] However, with relatively cheap encapsulation techniques, i.e. lamination between two glass sheets, the oxygen can be excluded enabling suitable stability of many organic materials.[7]

The solid-state dye-sensitized solar cell should be an ideal concept for excellent stability; unlike polymer solar cells it is composed of a preformed mesoporous metal oxide electrode which is not susceptible to structural degradation. Follow-

ing light absorption, the dye is completely regenerated from its oxidized state within a few hundred picoseconds, orders of magnitude faster than in the iodide/triiodide based liquid electrolyte cell, where dye regeneration occurs in the microsecond timescale.[9] The extremely rapid regeneration dynamics, as compared to the liquid electrolyte alternative, may play a big role in improved long-term stability of the solid state cell, as the dye is most likely to degrade in its oxidized state.[10]

Despite these apparent advantages over competing concepts, until now researchers have not been able to properly test the stability of solid-state DSCs. Upon encapsulation in an inert atmosphere and operation under sunlight, the devices lose their open-circuit voltage and fill factor within minutes due to a dramatic reduction in the cell shunt resistance, rendering them useless. Surprisingly, the devices completely recover to initial performance when re-exposed to air. Although Wang et al. have shown the stability of the system over a period of 1000h in a dry air atmosphere,[11] degradation of the organic hole transporter is likely to occur in long-term testing if oxygen is not excluded. There have only been a few reports of this effect. A previous study by Al-Dmour et al., predominantly based on impedance analysis, concludes that there is a dramatic increase in the recombination between electrons in the metal oxide and hole in the hole-transporter which renders the observed characteristics.[12, 13]

Here, a device study investigating mesoporous SnO_2 based solid-state DSCs is performed. The oxygen-free "photo-shunting" of the cell predominantly results from direct contact of the top metallic electrode with the mesoporous oxide. When exposed to oxygen, this contact forms a Schottky barrier[14] and is relatively unnoticeable in the standard cells. However, under an anaerobic atmosphere and sunlight the height of the Schottky barrier diminishes and "good" electronic contact is made between the cathode and the metal oxide. This results in a very effective shunting path which destroys the solar cell efficiency. A simple approach to block this contact would be to use a wide bandgap oxide such as MgO or Al_2O_3 in a core-shell configuration,[15, 16, 17] however the thin layer deposited in this manner still allows a tunneling current through the top contact when encapsulated in an inert atmosphere. In contrast, by introducing a thin interlayer of mesoporous alumina on top of the semiconducting metal oxide prior

to dye loading and hole-transporter infiltration, effective electronic blocking of this contact is made, and the rapid degradation dynamics are no longer observed. Initial results suggest that the oxygen-free devices are stable and this opens the possibility for long term stability tests and optimization.

9.2 Results and discussion

9.2.1 Device architecture

The issue of enabling the solid-state DSC to operate in an oxygen-free atmosphere has perplexed researchers in this area for the last five years. In Figure 9.1 the typical behavior devices fabricated from SnO_2[18] before and after sealing in Nitrogen under simulated sun light for a range of times are shown. After only 5 minutes measuring in nitrogen the open-circuit voltage has dropped from 0.47 to 0.22 V and the overall efficiency reduced from 1.26% in air to 0.51%.

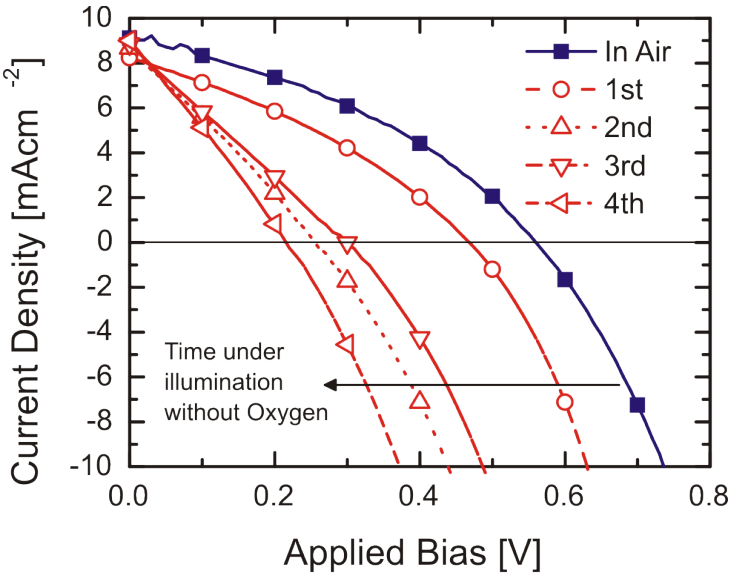

Figure 9.1: Current voltage characteristics for a SnO_2 based dye-sensitized solar cell measured under AM1.5 simulated sun light of 100mWcm^{-2}, in air (blue curve, solid-■) and when encapsulated in an air free environment (1ppm oxygen) (red curves, open-symbols). The 1^{st}, 2^{nd} 3^{rd} and 4^{th} scan of the encapsulated cell were taken at 40 second intervals.

The cause of this strange phenomenon could either be due to increased recombination at the dye sensitized interface,[12] or due to the opening of a short-circuiting path through the device. One possibility is that the hole-transporter is becoming much more conductive by an unknown mechanism. However, since highly conductive poly(3,4-ethylenedioxythiophene) works very well in dye-sensitized solar cells,[19, 20] this explanation seems unlikely. Furthermore, spiro-OMeTAD appears to be doped by air, so if any trend existed it would be expected to become less conductive in an inert atmosphere.

Another feasible possibility is that conductivity in the metal oxide increases considerably, resulting in either increased recombination at the heterojunction, or short-circuiting of the function of the compact underlayer, required to block contact of the hole-transporter to the FTO anode. This could be caused by nitrogen doping under light. To test whether this is the case, cells were encapsulated in pure argon and pure nitrogen atmospheres. Similar deteriorations in cell performance occurs for the cells sealed in the two gases (data not shown), suggesting that nitrogen doping is not the main cause for the phenomenon. Though this suggests that nitrogen doping does not occur, increased oxygen vacancy density in the metal oxide cannot be ruled out,[21] with each oxygen vacancy liberating two free electrons to the lattice, causing an increase in conductivity,[22] and potentially causing enhanced recombination or shunting through the compact underlayer.

The situation is thus; a low resistance shunting path switches on under illumination in an oxygen-free atmosphere, suggesting a light and oxygen sensitive switching mechanism is present somewhere between the FTO and metal electrode, most likely in the form of a barrier that disappears or is bypassed under these conditions. An electronic Schottky barrier is typically created when metals contact metal oxides, and Schottky barriers are extremely sensitive to charge density and the nature of surface states, which could be induced under light illumination. There are two possible locations of such contacts within the devices: the first one between the metal oxide and the FTO, and the second one between the metal oxide and the silver top electrode (cathode). In the first case, a change in the JV curve towards an "S" shape is expected in the case of a Schottky barrier,[23, 24] and in fact illuminating this barrier should be beneficial for the solar cell and

have negligible influence on open-circuit voltage.[23, 24]

Researchers have always assumed that the overstanding capping layer of spiro-OMeTAD is continuous and smooth so the contact between the mesoporous oxide and the metallic cathode is prevented. As shown in the atomic force microscopy images presented in figure 9.2, the over-standing layer of spiro-OMeTAD is not completely smooth, with around 40 nm roughness. The average thickness of this overlayer tends to be between 100 and 200 nm in optimized devices,[25] while the roughness of typical doctor bladed TiO_2 films as shown on figure 9.2.c is around 100 nm. It is proposed here that there are regions or pinholes where contact is made between the silver cathode and protruding peaks from the mesoporous metal oxide.[1]

9.2.2 Schottky diodes

In Figure 9.3a a schematic of the structure of the standard device is shown to aid the reader. Clearly if there is a contact between the top silver electrode and the metal oxide, a Schottky barrier at this contact would be beneficial to inhibit direct "shorting" between the electrodes through this metal oxide. To test whether this potential shorting path could facilitate the observed "shunting" of the device, simple diodes of mesoporous SnO_2 sandwiched between FTO and silver electrodes were fabricated. In Figure 9.4a the current voltage curves for such devices fabricated from SnO_2 are shown, measured in air and sealed in nitrogen, measured in the dark and under simulated AM1.5 sun light of 100mWcm^{-2}. Results for devices fabricated from mesoporous SnO_2 and mesoporous SnO_2 with a surface coating of MgO are shown, which is required for efficient solar cell operation.[18] The dark current through the SnO_2 devices in air is rather large, on the order of 40 mAcm^{-2} at 0.4V (where the maximum power conversion efficiency in solar cells is expected to be), but this is reduced considerably with the MgO surface coating to around 3 mAcm^{-2} at 0.4V. Similar curves, although slightly higher current, are observed when the diodes are illuminated by simulated AM1.5

[1] This is not conclusive evidence that pinholes exists, but it is suggestive of such. XPS depth profiling by Ding et al on TiO_2 based cells also suggests that the Ti signal increases over a thickness of ~300nm, suggestive of potential issues with pin holes through the thin spiro-OMeTAD overstanding layer.[26]

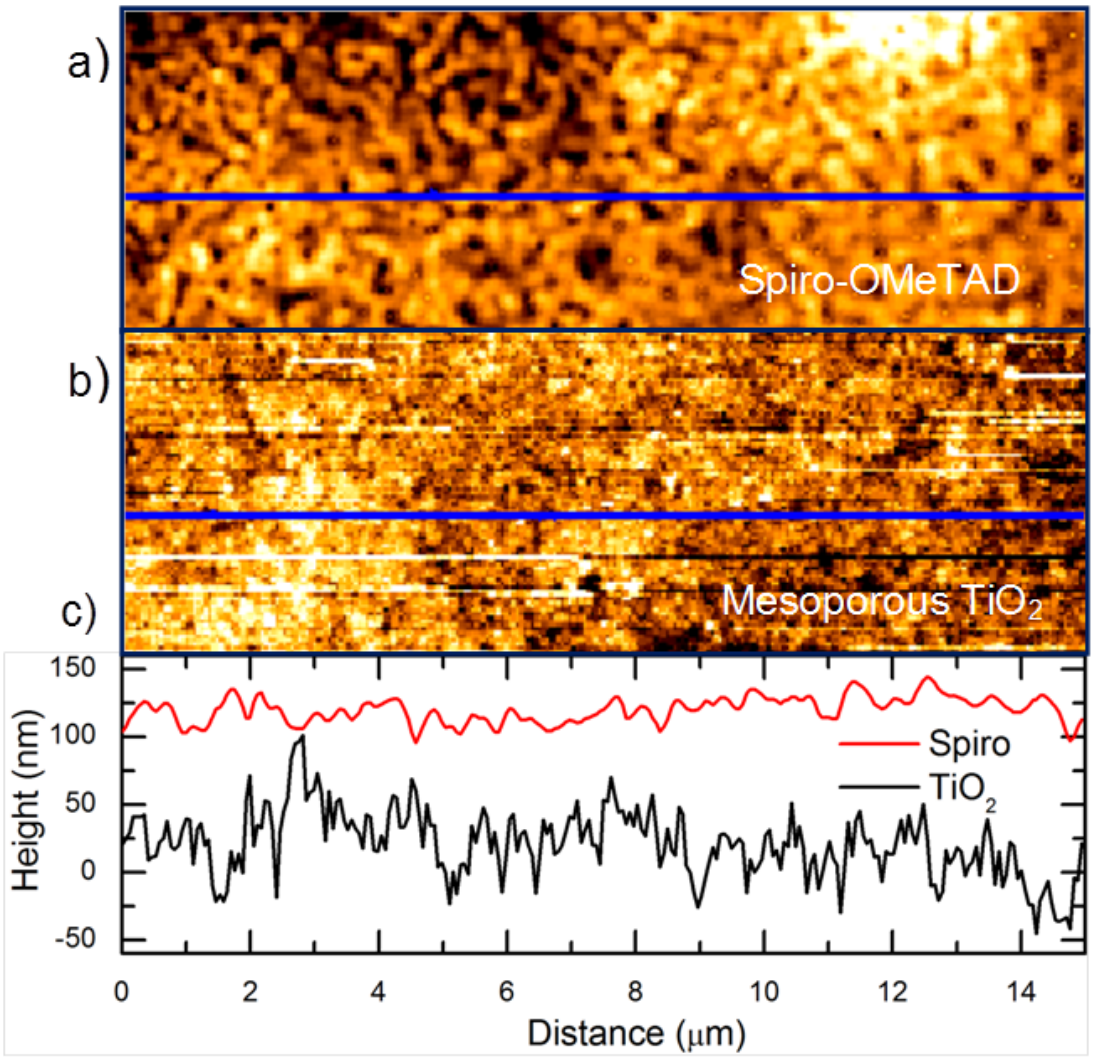

Figure 9.2: AFM images of the surface of (a) a spiro-OMeTAD coated mesoporous TiO_2 sample and (b) the same TiO_2 sample without the hole transporter. On (c) two line scans marked in (a, Spiro) and (b, TiO_2) with a typical vertical offset of 120 nm are shown. I acknowledge that the images presented in this figure were collected by Jack Alexander-Webber in the University of Oxford.

sun light at 100mWcm^{-2}. When encapsulated in nitrogen, the current is similar in the dark as when they were exposed to air, but for both the SnO_2 and SnO_2-MgO films the current density shoots up at low voltages when the films are illuminated in an oxygen free atmosphere, from 2 to 20mAcm^{-2} for the SnO_2-MgO film at 0.3V. This is consistent with the effective Schottky barrier at the silver cathode metal oxide contact reducing considerably when encapsulated in nitrogen and exposed to light. This is likely to be due to desorption of oxygen from the contact interface, and to the creation of oxygen vacancies which dope the interfacial region, an effect which has been observed in many different metal oxides. [14, 27, 28]

In order to quantify the nature of this contact, the existence of a Schottky barrier was assumed to exist at the silver SnO_2 interface, and fitted the current voltage curves, to the Schottky diode equation,

$$J = J_s e^{\frac{qV}{kT-1}} \tag{9.1}$$

$$\text{where } J_s = A^* T^2 e^{\frac{-q\Phi_B}{kT}} \tag{9.2}$$

$$\text{and } A^* = \frac{4\pi q m^* k^2}{h^3} \tag{9.3}$$

where J is the current density, J_s is the saturation current which is extrapolated from the current density at 0 V, V is the applied bias, q is the electron charge, k the Boltzmann constant, T the temperature, A^* the Richardson constant for thermionic emission, Φ_B the Schottky barrier height, m^* the effective electron mass and h is Plank's constant. This assumes that all the injection current is via thermionic emission, and ignores the shape of the barrier and tunneling currents.[29] An approximated value of the Richardson constant[1] A^*=36.06 Acm^{-2}K^{-2} was calculated from $m^* \sim 0.3 m_0$ for SnO_2.[30, 31]

The results for the calculated Schottky barrier heights under the different measurement conditions are summarized in Table 9.1 (these values are calculated from the linear fits shown in figure 9.4). As would be expected the barrier heights follow the trend observed for the JV curves, and range from 0.27 eV for

[1] A^* was not evaluated specifically for this system so the values derived for the barrier heights are taken as approximate

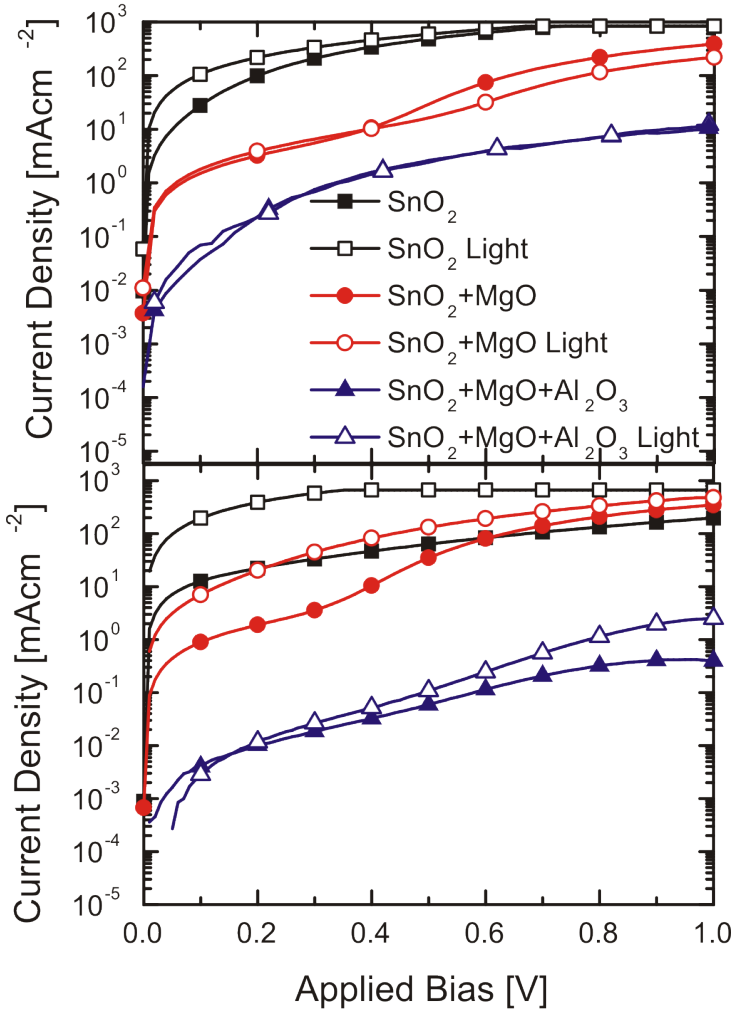

Figure 9.4: Current voltage curves for "Schottky diodes" composed of FTO-SnO_2-Ag (■), FTO-MgO coated SnO_2-Ag (●) and FTO-MgO coated SnO_2-mAl_2O_3-Ag (▲) measured in the dark (solid-symbols) and under AM1.5 simulated sun light of 100mWcm^{-2}(open-symbols). (top) Measured in air, and (bottom) encapsulated in a nitrogen filled glove box with ∼1ppm oxygen. Dotted lines are the linear fits used for the calculation of the barrier heights.

Device	Dark Φ_B (eV)	Light Φ_B (eV)
SnO_2 in air	0.27 ± 0.01	0.26 ± 0.01
SnO_2 in N_2	0.31 ± 0.04	0.25 ± 0.01
SnO_2+MgO in air	0.39 ± 0.01	0.38 ± 0.02
SnO_2+MgO in N_2	0.40 ± 0.03	0.32 ± 0.02

Table 9.1: Schottky barrier heights for diodes measured under different atmospheres estimated by fitting the JV curves in Figure 9.4 with Equation 9.2

SnO_2 in nitrogen under illumination, to 0.40 eV for SnO_2-MgO in air in the dark. These values are similar to those found in literature of 0.4 eV for polycrystalline SnO_2/Pt[14] contacts and 0.5-0.6 eV for SnO_2/Au contacts[32, 33]. Under illumination, the barrier height for the MgO coated substrates (SnO_2-MgO) in a N_2 atmosphere drop from 0.40 eV to 0.32 eV, which results in a ten-fold increase in the "leakage" current. The purpose of this investigation is not to develop a complete description of the nature of the electronic contact between nanostructured SnO_2 and metallic contacts, but to illustrate that an oxygen and light sensitive contact can exist at this location in the solar cell. Another possible explanation for the increased conductivity in the air-free diodes could be the reduction of a tunneling barrier at the grain boundaries (nanocrystal contacts). Indeed, the presence of an oxygen sensitive Schottky barrier at intergrain boundaries in oxides is the underlying sensing element in some metal oxide oxygen sensors. [34] However, this requires the grains to be significantly larger than the oxygen induced depletion regions at these interfaces, which is typically on the order of hundreds of nm. Since the samples prepared in this study consist of nanocrystalline SnO_2 in the order of 35 nm in size, see figure 3.3 for details, flattening of the bands is expected within the nanocrystals and negligible barriers are expected at the contact between identical particles.[35, 36] Further evidence to support the notion that the silver metal-oxide contact is responsible for the trends observed in Figure 9.4, comes from looking at the transport characteristics in fully functional solid-state dye-sensitized solar cells. [18]

Previously, it was shown that the addition of the MgO surface treatment did not change the electron transport properties significantly.[18] Despite this, here up to 1 to 2 orders of magnitude suppression in the current density through the

Schottky diodes is observed as compared to the bare SnO_2 diodes, suggesting that this is due to the contact between the SnO_2 and the silver, and not due to changes in the inter-SnO_2 nanoparticle contact. Also, the change in Schottky barrier height when comparing the SnO_2 diodes in air, to the SnO_2-MgO diodes in air is approximately 120 mV. This shift is similar to the CB shift found in chapter 7 for devices incorporating a thing MgO layer.

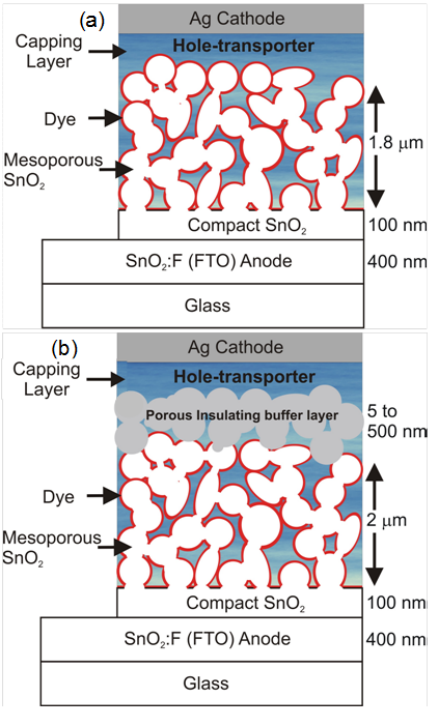

Figure 9.3: Schematic illustration of a SnO_2 based solid-state dye-sensitized solar cell (a) as is usually fabricated and (b) with the addition of a mesoporous inter-layer of Al_2O_3 on top of the mesoporous SnO_2.

A possible route to overcome the issue of leakage through the metal oxide is to include a thin insulating interlayer on top of the mesoporous n-type oxide. To test this, simple diodes with the addition of a 200 nm thick layer of mesoporous Al_2O_3 (m-Al_2O_3) on top of mesoporous MgO treated SnO_2 were fabricated. The JV curves for such SnO_2 based diodes are also shown in Figure 9.4a-b. A considerably lower current for the m-Al_2O_3-SnO_2-MgO devices encapsulated under illumination of 20 μAcm^{-2} at 0.4 V was observed, as compared to 20 mAcm^{-2} for the SnO_2-MgO diodes, illustrating successful electronic blocking of this contact. The photocurrent in a normal working device is only on the order of 10 mAcm^{-2} which will clearly be dominated by the direct conductivity through the mesoporous metal oxide, if a significant contact area exists. It is also noticeable that this contact is significantly influenced by the MgO surface treatment to the metal oxide. Bearing this in mind it is very likely that ourselves and others may have previously misinterpreted changes to this contact as apparent changes in the recombination dynamics at the dye-sensitized heterojunction.

9.2.3 Electronic properties

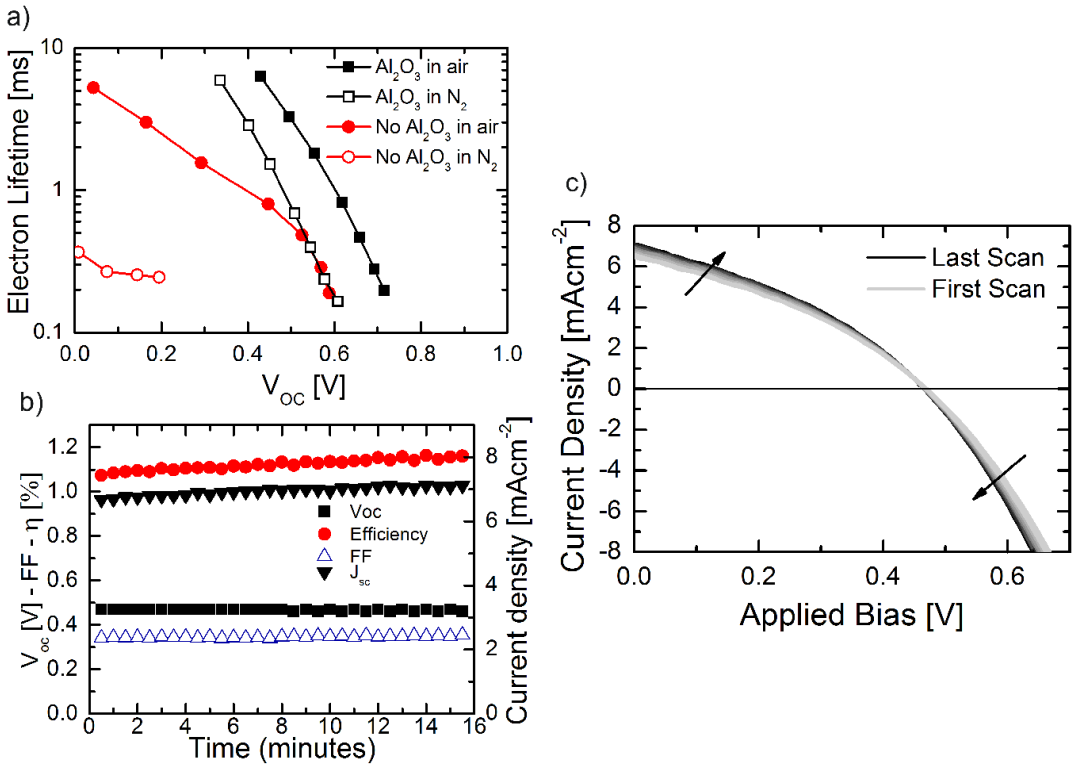

Figure 9.5: a) Electron lifetime versus open circuit voltage for devices incorporating an SnO_2 electrode with an MgO treatment and Al_2O_3 buffer layer (■) and without the Al_2O_3 layer (●) measured before (closed symbols) and after (open symbols) sealing in a N_2 atmosphere with <1 ppm oxygen. b) Evolution of the current voltage curves for a SnO_2 based solid-state DSC incorporating an Al_2O_3 buffer layer against time, encapsulated in a nitrogen filled glove box with 1ppm oxygen, measured under AM 1.5 simulated sun light of 100 mWcm^{-2}, 20 scans are plotted with the first scan in light gray and the last scan in black, the time between each scan was ∼40 seconds. c) photovoltaic performance parameters as a function of measuring time, extracted from the JV data in (b).

With the encouraging results of the diodes incorporating the m-Al_2O_3, and the potential identification of the cause of the "oxygen-free" phenomenon, solid-state DSCs from mesoporous SnO_2 electrodes with and without the addition of the mesoporous Al_2O_3 interlayer were fabricated. All SnO_2 devices have a surface coating of MgO, as described in the experimental section. A schematic of the

devices incorporating the Al_2O_3 interlayers is shown in Figure 9.3b. The current voltage curves for a SnO_2 device measured in air and when sealed in nitrogen are shown in Figure 9.5b. For the SnO_2 based devices (with MgO coating and an Al_2O_3 interlayer), all the photovoltaic parameters improve, even in air, with the addition of the Al_2O_3 interlayer. A detailed investigation of the effect of improving the overall efficiency of the SnO_2 based cells will be presented elsewhere. When sealed in nitrogen, the Al_2O_3 interlayer stabilizes the devices and enables efficient operation in an oxygen-free atmosphere. This can clearly be observed from the open-circuit recombination lifetimes plotted in Figure 9.5a as a function of open-circuit voltage. The encapsulated device without the insulating over-layer has undergone a significant drop in voltage, as compared to when measured in air, and at comparable potentials has an apparent order of magnitude reduction in the effective electron lifetime. Initial stability results for the sealed SnO_2 based cells show no degradation over the first 20 minutes of full sun operation at 50 degrees. The evolutions of the photovoltaic parameters are shown in Figure 9.5c.

9.3 Conclusions

In summary, a peculiar phenomenon of the solid-state dye-sensitized solar cell was presented, where efficient operation can only occur in an atmosphere containing oxygen. Through a device based investigation this behavior was identified to predominantly arise from a light and oxygen sensitive Schottky barrier present at the contact between the top of the mesoporous semiconducting metal oxide photo-anode and the hole-collecting silver cathode. This contact is successfully blocked by the addition of a mesoporous Al_2O_3 interlayer, which enables efficient and stable operation in an oxygen-free atmosphere. This development now enables long term stability to be effectively targeted, and represent a key milestone towards commercial realization of mesoporous hybrid solar cells.

References

[1] Frederik C. and Krebs. Fabrication and processing of polymer solar cells: A review of printing and coating techniques. *Solar Energy Materials and Solar*

Cells, 93(4):394 – 412, 2009. Processing and Preparation of Polymer and Organic Solar Cells. 134

[2] H. Sirringhaus, T. Kawase, R. H. Friend, T. Shimoda, M. Inbasekaran, W. Wu, and E. P. Woo. High-resolution inkjet printing of all-polymer transistor circuits. *Science*, 290(5499):2123–2126, 2000. 134

[3] Lars Blankenburg, Karin Schultheis, Hannes Schache, Steffi Sensfuss, and Mario Schrodner. Reel-to-reel wet coating as an efficient up-scaling technique for the production of bulk-heterojunction polymer solar cells. *Solar Energy Materials and Solar Cells*, 93(4):476 – 483, 2009. Processing and Preparation of Polymer and Organic Solar Cells. 134

[4] Gang Li, Vishal Shrotriya, Jinsong Huang, Yan Yao, Tom Moriarty, Keith Emery, and Yang Yang. High-efficiency solution processable polymer photovoltaic cells by self-organization of polymer blends. *Nat Mater*, 4(11):864–868, 2005. 10.1038/nmat1500. 134

[5] W. Ma, C. Yang, X. Gong, K. Lee, and A.J. Heeger. Thermally stable, efficient polymer solar cells with nanoscale control of the interpenetrating network morphology. *Advanced Functional Materials*, 15(10):1617–1622, 2005. 134

[6] Colin Powell, Timothy Bender, and Yuri Lawryshyn. A model to determine financial indicators for organic solar cells. *Solar Energy*, 83(11):1977 – 1984, 2009. 134

[7] Mikkel Jorgensen, Kion Norrman, and Frederik C. Krebs. Stability/degradation of polymer solar cells. *Solar Energy Materials and Solar Cells*, 92(7):686 – 714, 2008. Degradation and Stability of Polymer and Organic Solar Cells. 134

[8] Frederik C. Krebs, Suren A. Gevorgyan, and Jan Alstrup. A roll-to-roll process to flexible polymer solar cells: model studies, manufacture and operational stability studies. *J. Mater. Chem.*, 19:–, 2009. 134

[9] John N. Clifford, Emilio Palomares, Md K. Nazeeruddin, M. Gratzel, and James R. Durrant. Dye dependent regeneration dynamics in dye sensitized nanocrystalline solar cells: evidence for the formation of a ruthenium bipyridyl cation/iodide intermediate. *The Journal of Physical Chemistry C*, 111(17):6561–6567, 2007. 135

[10] Farahnaz Nour-Mohhamadi, Sau Doan Nguyen, Gerrit Boschloo, Anders Hagfeldt, and Torben Lund. Determination of the light-induced degradation rate of the solar cell sensitizer n719 on TiO_2 nanocrystalline particles. *The Journal of Physical Chemistry B*, 109(47):22413–22419, 2005. 135

[11] Mingkui Wang, Soo-Jin Moon, Mingfei Xu, Kethineni Chittibabu, Peng Wang, Ngoc-Le Cevey-Ha, Robin Humphry-Baker, Shaik M. Zakeeruddin, and Michael Gratzel. Efficient and stable solid-state dye-sensitized solar cells based on a high-molar-extinction-coefficient sensitizer. *Small*, 6(2):319–324, 2010. 135

[12] H. Al-Dmour and D. Taylor. Revisiting the origin of open circuit voltage in nanocrystalline-TiO_2/polymer heterojunction solar cells. *Applied Physics Letters*, 94(22), 2009. 135, 137

[13] Monica Lira-Cantu, Kion Norrman, Jens W. Andreasen, Nieves Casan-Pastor, and Frederik C. Krebs. Detrimental effect of inert atmospheres on hybrid solar cells based on semiconductor oxides. *Journal of The Electrochemical Society*, 154(6):B508–B513, 2007. 135

[14] Christoph Korber, Steven P. Harvey, Thomas O. Mason, and Andreas Klein. Barrier heights at the SnO_2/pt interface: In situ photoemission and electrical properties. *Surface Science*, 602(21):3246–3252, 2008. 135, 140, 142

[15] A. Kay and M. Gratzel. Dye-sensitized core-shell nanocrystals: Improved efficiency of mesoporous tin oxide electrodes coated with a thin layer of an insulating oxide. *Chemistry of Materials*, 14(7):2930–2935, 2002. 135

[16] B. C. O'Regan, S. Scully, A. C. Mayer, E. Palomares, and J. Durrant. The effect of al2o3 barrier layers in TiO_2/dye/cuscn photovoltaic cells explored

by recombination and dos characterization using transient photovoltage measurements. *The Journal of Physical Chemistry B*, 109(10):4616–4623, 2005. 135

[17] Xin tong Zhang, Irwan Sutanto, Taketo Taguchi, Kenichi Tokuhiro, Qing bo Meng, Tata N. Rao, Akira Fujishima, Hiroko Watanabe, Toshie Nakamori, and Masayuki Uragami. Al2o3-coated nanoporous TiO_2 electrode for solid-state dye-sensitized solar cell. *Solar Energy Materials and Solar Cells*, 80(3):315 – 326, 2003. 135

[18] H. J. Snaith and C. Ducati. SnO_2-based dye-sensitized hybrid solar cells exhibiting near unity absorbed photon-to-electron conversion efficiency. *Nano Letters*, 10(4):1259–1265, 2010. 136, 139, 142

[19] Yukyeong Kim, Yung-Eun Sung, Jiang-Bin Xia, Monica Lira-Cantu, Naruhiko Masaki, and Shozo Yanagida. Solid-state dye-sensitized TiO_2 solar cells using poly(3,4-ethylenedioxythiophene) as substitutes of iodine/iodide electrolytes and noble metal catalysts on fto counter electrodes. *Journal of Photochemistry and Photobiology A: Chemistry*, 193(2-3):77–80, 2008. 137

[20] Yasuteru Saito, Norihiro Fukuri, Rohan Senadeera, Takayuki Kitamura, Yuji Wada, and Shozo Yanagida. Solid state dye sensitized solar cells using in situ polymerized pedots as hole conductor. *Electrochemistry Communications*, 6(1):71–74, 2004. 137

[21] J. Weidmann, T. Dittrich, E. Konstantinova, I. Lauermann, I. Uhlendorf, and F. Koch. Influence of oxygen and water related surface defects on the dye sensitized TiO_2 solar cell. *Solar Energy Materials and Solar Cells*, 56(2):153–165, 1999. 137

[22] Y. Muraoka, N. Takubo, and Z. Hiroi. Photoinduced conductivity in tin dioxide thin films. *Journal of Applied Physics*, 105(10), 2009. 137

[23] S. Ruhle and D. Cahen. Electron tunneling at the TiO_2/substrate interface can determine dye-sensitized solar cell performance. *Journal of Physical Chemistry B*, 108(46):17946–17951, 2004. 137

[24] H. J. Snaith and M. Gratzel. The role of a schottky barrier, at an electron-collection electrode in solid-state dye-sensitized solar cells. *Advanced Materials*, 18(14):1910–+, 2006. 137

[25] Henry J. Snaith, Robin Humphry-Baker, Peter Chen, Ilkay Cesar, Shaik M. Zakeeruddin, and Michael Gratzel. Charge collection and pore filling in solid-state dye-sensitized solar cells. *Nanotechnology*, 19(42), 2008. 139

[26] I. K. Ding, N. Tetreault, J. Brillet, B. E. Hardin, E. H. Smith, S. J. Rosenthal, F. Sauvage, M. Gratzel, and M. D. McGehee. Pore-filling of spiro-ometad in solid-state dye sensitized solar cells: Quantification, mechanism, and consequences for device performance. *Adv. Func. Matter.*, 19(15):2431–2436, 2009. 139

[27] H. L. Mosbacker, Y. M. Strzhemechny, B. D. White, P. E. Smith, D. C. Look, D. C. Reynolds, C. W. Litton, and L. J. Brillson. Role of near-surface states in ohmic-schottky conversion of au contactsto ZnO. *Applied Physics Letters*, 87(1), 2005. 140

[28] R. Schafranek, S. Payan, M. Maglione, and A. Klein. Barrier height at (ba,sr) tio3 /pt interfaces studied by photoemission. *Physical Review B*, 77(19):195310, 2008. 140

[29] S. N. Sze. Physics of semiconductor devices. *Wiley-Interscience. Second edition*, pages 256, 258, 1981. 140

[30] K. J. Button, C. G. Fonstad, and Dreybrod.W. Determination of electron masses in stannic oxide by submillimeter cyclotron resonance. *Physical Review B*, 4(12):4539–, 1971. 140

[31] M. Nagasawa, S. Shionoya, and Makishim.S. Electron effective mass of SnO_2. *Journal of the Physical Society of Japan*, 20(6):1093–, 1965. 140

[32] O. Bierwagen, M. E. White, M. Y. Tsai, T. Nagata, and J. S. Speck. Non-alloyed schottky and ohmic contacts to as-grown and oxygen-plasma treated n-type SnO_2 (110) and (101) thin films. *Applied Physics Express*, 2(10), 2009. 142

[33] T. Nagata, O. Bierwagen, M. E. White, M. Y. Tsai, and J. S. Speck. Study of the au schottky contact formation on oxygen plasma treated n-type SnO_2 (101) thin films. *Journal of Applied Physics*, 107(3), 2010. 142

[34] E. R. Leite, A. M. Nascimento, P. R. Bueno, E. Longo, and J. A. Varela. The influence of sintering process and atmosphere on the non-ohmic properties of SnO_2 based varistor. *Journal of Materials Science-Materials in Electronics*, 10(4):321–327, 1999. 142

[35] C. Malagu, V. Guidi, M. Stefancich, M. C. Carotta, and G. Martinelli. Model for schottky barrier and surface states in nanostructured n-type semiconductors. *Journal of Applied Physics*, 91(2):808–814, 2002. 142

[36] T. S. Rantala and V. Lantto. Some effects of mobile donors on electron trapping at semiconductor surfaces. *Surface Science*, 352:765–770, 1996. 142

Chapter 10

Conclusions and Outlook

A power conversion efficiency of over 20% can theoretically be achieved for solid-state dye-sensitized solar cells, even allowing for losses involving overpotentials to drive the required processes.[1] Currently, however, the maximum efficiency achieved is around 7%,[2] due to thickness limitations, i.e. short diffusion lengths. While problems with long-term stability have been dealt with in chapter 9, there appear to be severe losses in the system and it is important to identify them in order to make improvements.

One of the most puzzling aspects of solid-state dye-sensitized solar cells is their low photon to electron conversion efficiencies, which lead to lower short circuit currents than expected. Factors affecting this parameter can be summarized by equation 10.1. Here the light harvesting efficiency (η_{abs}) is simply the fraction of absorbed light, the charge transfer efficiency (η_{trans}) is the fraction of successfully generated electron-hole pairs from each incident photon which are than transferred into TiO_2 and spiro respectively, and η_{col} is the fraction of collected charges at the electrodes:

$$IPCE = \eta_{abs} \cdot \eta_{trans} \cdot \eta_{col} \tag{10.1}$$

In general, the dyes used for ssDSCs have very high extinction coefficients (in particular, for the dye most used in this work, termed D102, it's 55800 $Lmol^{-1}cm^{-1}$ at its peak), and hence high η_{abs}. Through the Beer-Lambert law the extinction coefficient (ϵ), the transmitted light fraction (T), the path length (l) and the concentration of the absorber (c) can be related:[3]

$$T = 10^{\epsilon lc} \tag{10.2}$$

From dye desorption measurements (see section 3.2), for the typical commercial TiO_2 paste from Dyesol after $TiCl_4$ treatment (see section 3.1.4.1), ∼128mmoles of dye per cm^3 of film can be calculated. With this concentration and equation 10.2, ∼1.5μm as the path length necessary to absorb around 90% of the light can be extracted. Most optimised cells can easily achieve between 2 and 2.5 μm without significant losses to charge collection,[4] and since these devices usually incorporate a silver contact on the back to collect the holes, the path length is in fact doubled since silver reflects around 98% of the incident light in the visible range.[5] Most of the devices fabricated from organic dyes generally fall short of generating around 8 $mAcm^{-2}$ short circuit currents. Since it is theoretically possible to generate at least 13 $mAcm^{-2}$ by integrating the absorption spectrum of the dye-sensitized films with the incident solar spectrum shown in figure 2.1, it can be concluded that light absorption for the common dyes used in ssDSCs is not the main loss mechanism.

Parameters influencing η_{trans} include the quantum yield from the dyes, usually dependent on the LUMO and CB level positions, and the availability of charge transfer states. Electron transfer rates from dyes in sensitized metal oxides are usually heterogeneous.[6] This implies that in order to maximize charge transfer efficiency, an overpotential between the excited state energy level of the dye and the accepting states in the TiO_2 must be established. In particular, the slowest injecting states can be sped up considerably by lowering the conduction band edge, i.e. away from vacuum.[7] This problem has been studied in great detail in chapters 4 and 5, where it was found that crystallizing titania in an organic rich matrix led to a distribution of sub bandgap states more favorable for charge generation. However, the improvements were relatively minor at only around 16% extra short circuit current for the optimized triblock terpolymer route(chapter 5).

The fact that charge generation can still be improved quite a lot further suggests that some of the losses to the short circuit current stem from the hole regeneration dynamics. While the dye regeneration process is very efficient at

low light intensities,[8, 9] it is likely to be dye dependent as well as being greatly influenced by the additives in the hole transporter. Indeed, on an indoline-based dye similar to the one used in this thesis, the solar cells perform extremely well under low light conditions after the addition of lithium ions (over 6% efficient), but as the light intensity is increased, this number can drop to almost half.[10] The crux of the matter is that hole regeneration is extremely fast, usually faster than electron injection, leading to a system where the electron is not injected first into the TiO_2 and detrimental charge build-up at the interface can occur. The lithium ions were found to be essential in order to extend the lifetime of the excited dye and subsequent high charge generation efficiency. It is my opinion that further improvements will arise from optimizing the charge generation dynamics.

To optimize the charge collection efficiency, and hence make thicker films available, the factors limiting the diffusion length of the devices must be identified. While multiple studies suggested that pore filling is the limiting factor to achieving thick cells (in the order of 5 μm),[11, 12, 13] and therefore complete light absorption by the most common sensitizers, I have conclusively shown in chapter 6 that it is possible to sufficiently fill films up to 5 μm in thickness. Since pore filling does not seem to be the issue, other strategies must be pursued to enhance the charge collection length.

In chapter 7, I have studied the effects of a thin MgO layer and it was observed that this treatment extends the electron lifetimes by an order of magnitude. However, this is accompanied by a reduction in the charge generation efficiency. When used in TiO_2 films, a big reduction in current is observed. For this reason, the use of insulating metal oxide coatings, while extending the charge collection length, is unlikely to lead to competitive power conversion efficiencies and therefore a different solution must be sought.

In chapter 8 I have shown that the charge transport through the films can be enhanced by an order of magnitude by simply reducing the number of intergrain boundaries. This rather surprising result opens up the possibility of extending the diffusion lengths in systems with large crystals. Usually this leads to reduced surface area and consequently smaller short circuit currents. However, if strategies can be employed where the TiO_2 is crystallized in a confined morphology, the surface area does not necessarily have to be compromised. It is my opinion then

that to fully optimize the performance of solid-state dye-sensitized solar cells, future research efforts must be directed at enabling the formation of films where the crystal size is decoupled from the surface area of the films. If a favorable DOS distribution for charge transfer can be maintained, large improvements should be possible.

References

[1] H. J. Snaith. Estimating the maximum attainable efficiency in dye-sensitized solar cells. *Advanced Functional Materials*, 20(1):13–19, 2010. 151

[2] Julian Burschka, Amalie Dualeh, Florian Kessler, Etienne Baranoff, Ngoc-Le Cevey-Ha, Chenyi Yi, Mohammad K. Nazeeruddin, and Michael Gratzel. Tris(2-(1h-pyrazol-1-yl)pyridine)cobalt(iii) as p-type dopant for organic semiconductors and its application in highly efficient solid-state dye-sensitized solar cells. *Journal of the American Chemical Society*, 133(45):18042–18045, 2011. 151

[3] James D. Ingle and Stanley R. Crouch. Spectrochemical analysis. *Prentice Hall 1st edition*, 1988. 151

[4] Henry J. Snaith, Robin Humphry-Baker, Peter Chen, Ilkay Cesar, Shaik M. Zakeeruddin, and Michael Gratzel. Charge collection and pore filling in solid-state dye-sensitized solar cells. *Nanotechnology*, 19(42), 2008. 152

[5] Hiram W. Edwards and Robert P. Petersen. Reflectivity of evaporated silver films. *Phys. Rev.*, 50:871–871, Nov 1936. 152

[6] B. Wenger, M. Gratzel, and J. E. Moser. Rationale for kinetic heterogeneity of ultrafast light-induced electron transfer from ru(ii) complex sensitizers to nanocrystalline TiO_2. *J. Am. Chem. Soc*, 127(35):12150–12151, 2005. 0002-7863. 152

[7] S. Koops, B. O'Regan, P. R. F. Barnes, and J. R. Durrant. Parameters influencing the efficiency of electron injection in dye-sensitized solar cells. *J. Am. Chem. Soc*, 131(13):4808–4818, 2009. 152

[8] U. B. Cappel, E. A. Gibson, A. Hagfeldt, and G. Boschloo. Dye regeneration by spiro-meotad in solid state dye-sensitized solar cells studied by photoinduced absorption spectroscopy and spectroelectrochemistry. *Journal of Physical Chemistry C*, 113(15):6275–6281, 2009. 153

[9] Ute B. Cappel, Amanda L. Smeigh, Stefan Plogmaker, Erik M. J. Johansson, Hakan Rensmo, Leif Hammarstrom, Anders Hagfeldt, and Gerrit Boschloo. Characterization of the interface properties and processes in solid state dye-sensitized solar cells employing a perylene sensitizer. *The Journal of Physical Chemistry C*, 115(10):4345–4358, 2011. doi: 10.1021/jp111466h. 153

[10] Henry J. Snaith, Annamaria Petrozza, Seigo Ito, Hidetoshi Miura, and Michael Gratzel. Charge generation and photovoltaic operation of solid-state dye-sensitized solar cells incorporating a high extinction coefficient indolene-based sensitizer. *Advanced Functional Materials*, 19(11):1810–1818, 2009. 153

[11] H.J. Snaith and L. Schmidt-Mende. Advances in liquid-electrolyte and solid-state dye-sensitized solar cells. *Adv. Mater.*, 19(20):3187–3200, 2007. 153

[12] I. K. Ding, N. Tetreault, J. Brillet, B. E. Hardin, E. H. Smith, S. J. Rosenthal, F. Sauvage, M. Gratzel, and M. D. McGehee. Pore-filling of spiro-ometad in solid-state dye sensitized solar cells: Quantification, mechanism, and consequences for device performance. *Adv. Func. Matter.*, 19(15):2431–2436, 2009. 153

[13] Lukas Schmidt-Mende and Michael Gratzel. Tio2 pore-filling and its effect on the efficiency of solid-state dye-sensitized solar cells. *Thin Solid Films*, 500(12):296–301, 2006. 153

Appendix: Publications and International Conferences

Publications

- 1. **Docampo,P;** Ivaturi, A; Gunning, R; Diefenbach, S; Kirkpatrick, J; Palumbiny, C.M; Sivaram, V.; Geaney, H; Schmidt-Mende, L; Welland, M.E; Snaith, H.J; "The influence of 1D structures on charge transport in solid-state dye-sensitized solar cells." [In preparation]

- 2. **Docampo,P;** Guldin, S; Steiner, U.; Snaith, H.J; "Limits to the electron transport in mesoporous TiO_2 photoanodes" [In preparation]

- 3. Tiwana, P; **Docampo,P;** Johnston, M.B; Herz, L.M; Snaith, H.J; "The Origin of an efficiency improving "light soaking" effect in SnO_2 based solid-state Dye Sensitized Solar Cells." [Submitted]

- 4. **Docampo,P;** Hey, A.;Guldin, S; Gunning, R; Steiner, U; Snaith, H.J; "Pore-filling of spiro-OMeTAD in solid-state DSCs determined via optical reflectometry." [Submitted]

- 5. **Docampo,P;** Tiwana, P; Sakai, N; Miura, H; Herz L.M; Takurou, M; Snaith, H.J; "Unraveling the function of an MgO interlayer in both electrolyte and solid-state SnO_2 based dye-sensitized solar cells." [Submitted]

- 6. **Docampo, P.;**Guldin, S; Stefik,M; Yufa, N; Wiesner, U; Steiner, U.; Snaith, H.J.; "Triblock terpolymer directed self-assembly of mesoporous TiO_2 - high performance photoanodes for solid state dye-sensitized solar cells." [Accepted], Advanced Energy Materials, 2012, DOI: aenm.201100699.

- 7. Guldin, S.; **Docampo, P.;** Stefik, M.; Kamita, G; Wiesner, U.; Snaith, H.J.; Steiner, U.; "Layer-by-Layer Formation of Block-Copolymer-Derived TiO_2 for Solid-State Dye-Sensitized Solar Cells." Small 2012, 8 (3), 432-440.

- 8. S. Guldin, **P. Docampo,** S. Httner, P. Kohn, M. Stefik, H. J. Snaith, U. Wiesner and U. Steiner, "Self-assembly as a design tool for the integration of photonic structures into excitonic solar cells." Proc. SPIE 8111, 811108 (2011); doi:10.1117/12.893798

- 9. Tiwana, P.; **Docampo, P.;** Johnston, M. B.; Snaith, H. J.; Herz, L. M., "Electron Mobility and Injection Dynamics in Mesoporous ZnO, SnO_2, and TiO_2 Films Used in Dye-Sensitized Solar Cells." ACS Nano 2011, 5 (6), 5158-5166.

- 10. Snaith, H. J.; Stavrinadis, A.; **Docampo, P.;** Watt, A. A. R., "Lead-sulphide quantum-dot sensitization of tin oxide based hybrid solar cells." Solar Energy 2011, 85 (6), 1283-1290.

- 11. **Docampo, P.;** Snaith, H. J., "Obviating the requirement for oxygen in SnO_2-based solid-state dye-sensitized solar cells." Nanotechnology 2011, 22 (22).

- 12. Guldin, S.; Huttner, S.; Tiwana, P.; Orilall, M. C.; Ulgut, B.; Stefik, M.; **Docampo, P.;** Kolle, M.; Divitini, G.; Ducati, C.; Redfern, S. A. T.; Snaith, H. J.; Wiesner, U.; Eder, D.; Steiner, U., "Improved conductivity in dye-sensitised solar cells through block-copolymer confined TiO_2 crystallisation." Energy & Environmental Science. 2011, 4 (1), 225-233.

- 13. **Docampo, P.;** Guldin, S.; Stefik, M.; Tiwana, P.; Orilall, M. C.; Huttner, S.; Sai, H.; Wiesner, U.; Steiner, U.; Snaith, H. J., "Control of Solid-State Dye-Sensitized Solar Cell Performance by Block-Copolymer-Directed TiO_2 Synthesis." Advanced Functional Materials. 2010, 20 (11), 1787-1796.

International Conference Talks

- April 2011 MRS Spring Meeting in San Francisco - "Control of Solid-State Dye-Sensitized Solar Cell Performance by Block-Copolymer-Directed TiO_2 Synthesis" **P. Docampo**, S. Guldin, M. Stefik, P. Tiwana, C. M. Orilall, S. Huttner, H. Sai, U. Wiesner, U. Steiner, H. J. Snaith.

International Conference Posters

- June 2011 JUDO-PV Meeting in Oxford - "The role of a thin MgO shell on the surface of SnO2 based dye-sensitized solar cells" **P. Docampo**, Priti Tiwana, Nobuya Sakai, Takurou N. Murakami, Henry J. Snaith.

- May 2011 HOPV Meeting in Valencia - "Controlling the Electronic States and the Interplay Between Transport and Charge Generation in Self-Assembled Oxides for Solid-State Dye-Sensitized Solar Cells" **P. Docampo**, S. Guldin, M. Stefik, P. Tiwana, C. M. Orilall, S. Huttner, H. Sai, U. Wiesner, U. Steiner, H. J. Snaith.

- December 2009 MRS Fall Meeting in Boston - "Block-copolymer Self-assembly in Mesoporous Metal Oxide Films: Application in Efficient Hybrid Solar Cells" **P. Docampo,** S. Guldin, M. Stefik, P. Tiwana, C. Orilall, S. Httner, U. Wiesner, U. Steiner, and H. J. Snaith.

Appendix: Posters

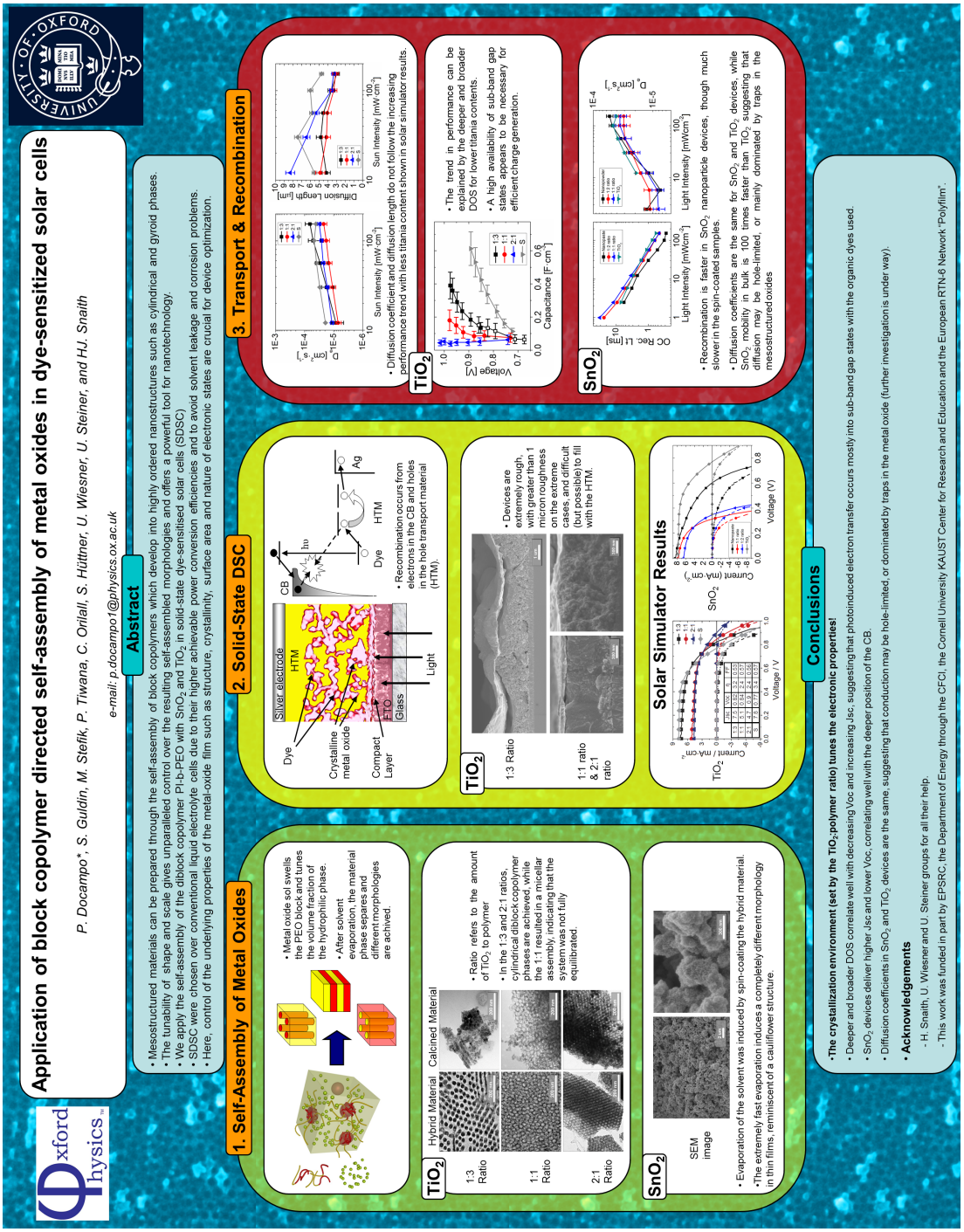

Figure 1: MRS Fall Meeting 2009 Poster

The role of a thin MgO shell on the surface of SnO_2 based dye-sensitized solar cells

Pablo Docampo, Priti Tiwana, Nobuya Sakai, Takurou N. Murakami, Henry J. Snaith*
e-mail: p.docampo1@physics.ox.ac.uk

Abstract

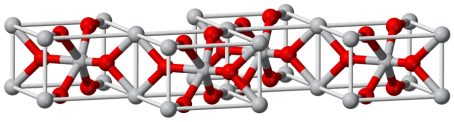

SnO_2 based dye-sensitized solar cells (DSC) are a very promising device concept. The conduction band (CB) in this material is situated 0.5 eV further from vacuum as compared to TiO_2. This has a profound influence in the device applications, since this allows us to target narrower bandgap dyes, which may lead to overall improvements in efficiency.[1] This material also benefits from improved stability, as SnO_2 is less photoreactive than TiO_2 due to its wider bandgap.
However, fabricating efficient devices based on SnO_2 requires careful tuning of the surface via a shell of MgO when used with the current available dyes. In this study, **we explore the precise function of the thin MgO shell** by fabricating and characterizing both electrolyte and solid-state DSCs utilizing indolene based dyes. In contrast to most reports in literature,[2] **we observe no change to recombination dynamics with or without the MgO shell, for both electrolyte and solid-state DSCs**, when measured under comparative operating conditions.

Most previous studies were performed under open circuit conditions for which the charge density varies considerably between the cells with and without the MgO shell. **We observe that the predominant function of this coating is a shift of the CB of the SnO_2 mesostructure**, which is the overriding factor governing the enhancement to open circuit voltage.

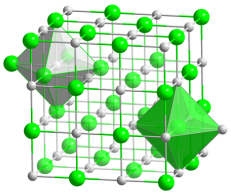

Crystal structure of MgO

Photovoltaic performance

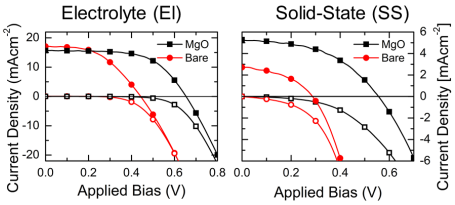

	El-Bare	El-MgO	SS-Bare	SS-MgO
Jsc (mAcm2)	17.1	15.7	2.72	5.28
Voc (V)	0.45	0.67	0.28	0.56
FF	0.47	0.61	0.32	0.47
Eff(%)	3.65	6.4	0.32	1.39

Ultrafast charge dynamics, optical-pump THz-probe wavelengths.

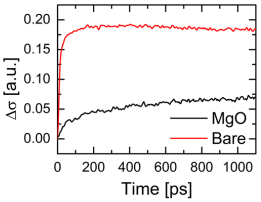

Complete charge injection in SnO_2 sensitized with Z907 takes place within the first few hundred picoseconds. However, in case of MgO treated SnO_2, charge injection keeps taking place even beyond the first nanosecond.

Electronic characteristics, transient photovoltage and photocurrent decays

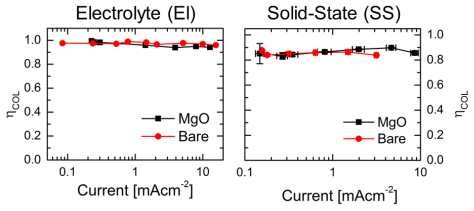

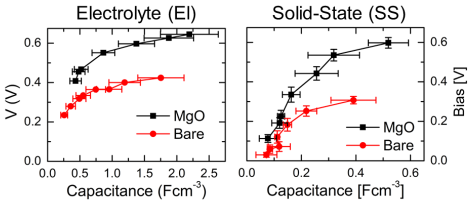

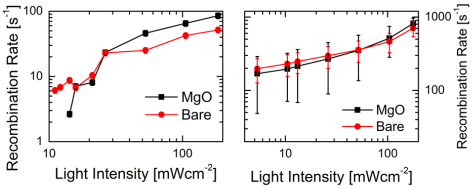

•For El and SS devices the recombination dynamics are the same under comparative operating conditions, whether there is an MgO shell or not. There is no difference in charge collection efficiency, which is almost unity in El-DSC.

•This result is particularly important to the viability of using SnO_2 as the mesoporous metal oxide for narrow band-gap dyes, since the recombination dynamics seem to be relatively unaffected by the MgO coating which was found to be critical in the past.

• In the devices prepared for this study, what is observed after the addition of the MgO shell is mainly a ~250 mV shift in the surface potential, for both liquid and solid-state DSCs, as shown in the Voltage/Capacitance plots (see above).

References

1. Snaith, H. J., Estimating the Maximum Attainable Efficiency in Dye-Sensitized Solar Cells. *Adv. Funct. Mater.* **2010,** *20* (1), 13-19.
2. Green, A. N. M.; Palomares, E.; Haque, S. A.; Kroon, J. M.; Durrant, J. R., Charge transport versus recombination in dye-sensitized solar cells employing nanocrystalline TiO2 and SnO2 films. *J. Phys. Chem. B* **2005,** *109* (25), 12525-12533.

• I would like to thank the Henry J. Snaith group, particularly Andrew Hey, and Nobuya Sakai for all their help.

Figure 2: HOPV Meeting 2011 Poster

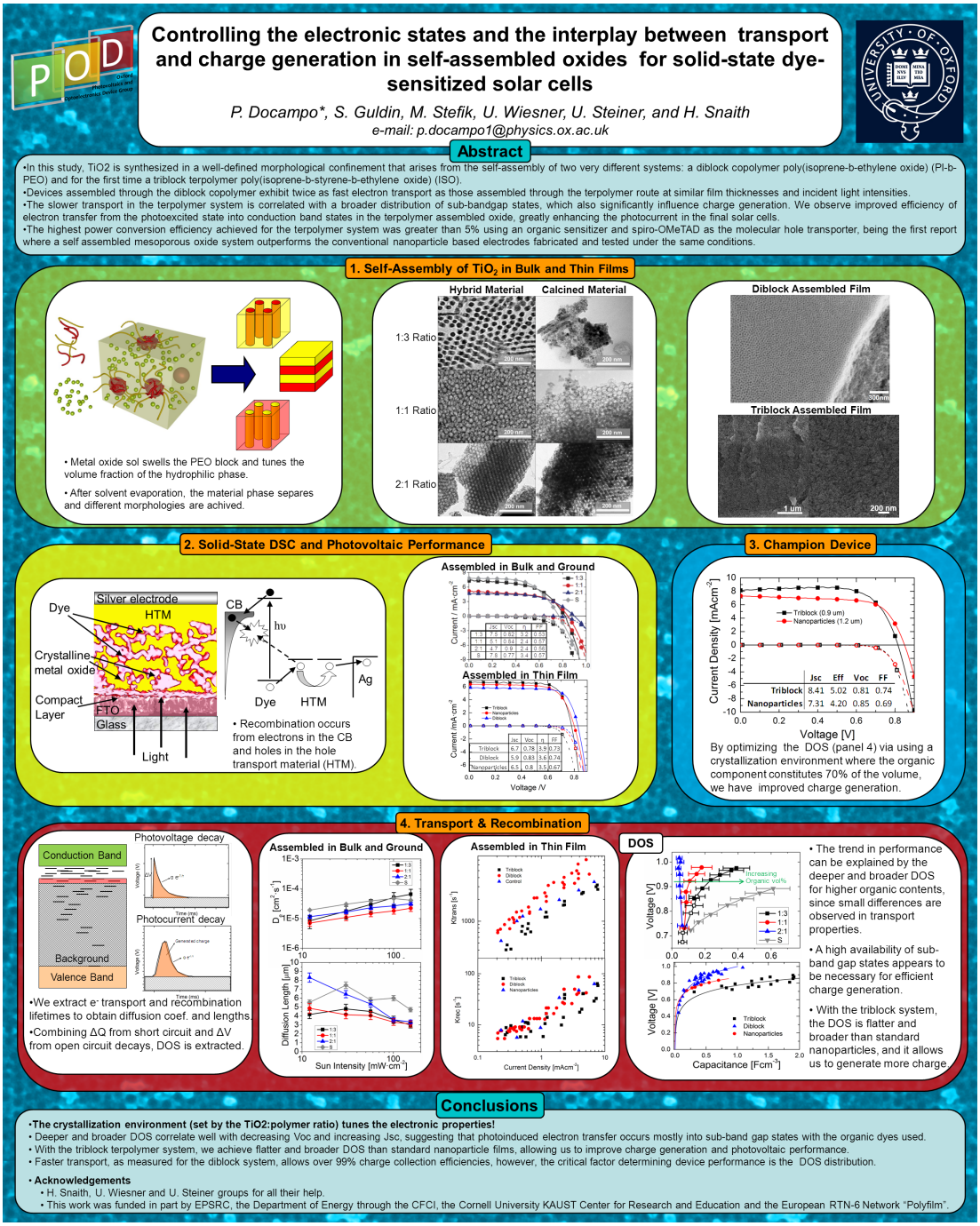

Figure 3: JUDO-PV Meeting 2011 Poster